CHALMERS
UNIVERSITY OF TECHNOLOGY

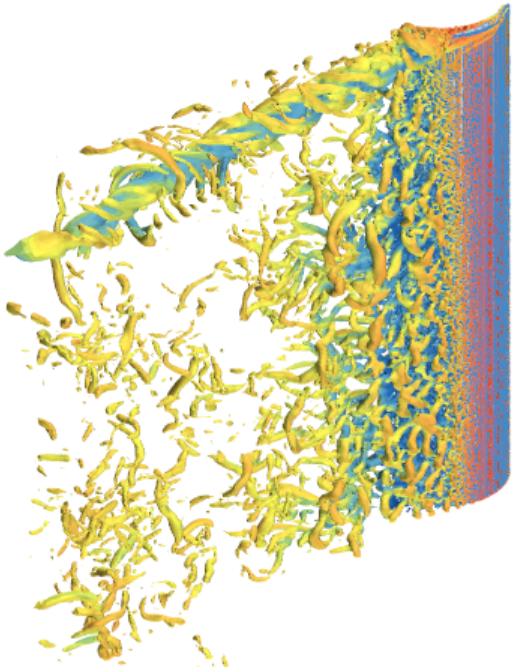

Evaluation of Novel Wingsail Concepts in Terms of Aerodynamic Efficiency

Master's thesis in Engineering mathematics and computational science

ERIK LJUNGBERG

DEPARTMENT OF MECHANICS AND MARITIME SCIENCES

CHALMERS UNIVERSITY OF TECHNOLOGY
Gothenburg, Sweden 2023
www.chalmers.se

Master's thesis 2023

Evaluation of Novel Wingsail Concepts in Terms of Aerodynamic Efficiency

ERIK LJUNGBERG

CHALMERS
UNIVERSITY OF TECHNOLOGY

Department of Mechanics and maritime sciences
Chalmers University of Technology
Gothenburg, Sweden 2023

Erik Ljungberg

Supervisors: Heng Zhu, Mechanics and maritime sciences. Bengt Ramne, ScandiNAOS. Henry Lee, ScandiNAOS
Co-supervisor: Laura Marimon Giovannetti, SSPA
Examiner: Hua-Dong Yao, Mechanics and maritime sciences

Master's Thesis 2023
Department of Mechanics and maritime sciences
Chalmers University of Technology
SE-412 96 Gothenburg
Telephone +46 31 772 1000

Cover: Illustration of vortex shedding and the velocities of vortexes from a crescent-shaped wingsail, simulated in STAR-CCM+ with LES turbulence model.

Typeset in LaTeX
Printed by Chalmers Reproservice
Gothenburg, Sweden 2023

Erik Ljungberg
Department of Mechanics and maritime sciences
Chalmers University of Technology

Abstract

In this project the evaluation and comparison of five different designs for rigid wingsails were made by performing simulations in the CFD software STAR-CCM+ and two parameters, gap distance between foils and camber angle for three of the wingsails were varied to understand its effects. The wingsails in question were the crescent-shaped profile, two-element foil sails and three element foil sails. Three different designs were created for the two element foil sails with the following ratios of the total chord length between the front and aft foils; 70/30, 80/20, 90/10, and only one design for the three element foil sail with ratio 15/70/15. The parameters of gap distance and camber angle were only altered for the two element foil wingsails, while only the camber was altered for the three element foil wingsail. The comparisons that were made between the different designs were between the propulsive performances as well as stall angles. This study has found that, regarding the two element foil designs, the absence of a gap between the front and aft foils yield superior propulsive performance and that the difference in performance between different non-zero gap sizes is not very significant. The crescent-shaped profile performs significantly better than the non-cambered multi-element foil sails, but appeared to be a less favourable design when compared with the no-gap, cambered multi-element foil sails. However 3D simulation results revealed that the performance of the best multi-element foil design, the two element foil sail with ratio 70/30, no gap and 25° camber had been severely overestimated, and performed worse through all apparent wind angles when compared to the crescent-shaped profile. If we were to assume that the relation between the multi-element foil designs remained the same, in terms of performance over all apparent wind angles, when performing 3D simulations, then they would be ranked as follows. The best designs in terms of overall propulsion, in order of greatest to worst, are the crescent-shaped profile followed by the two element foil sails with ratio 70/30 and 80/20 with no gap and 25° camber and lastly ratio 90/10 (also no gap and 25° camber) and the three element foil profile with ratio 15/70/15 and 15° camber. It was discovered that the crescent-shaped profile began to experience stall, often much later than the multi-element foil designs, and reached its critical angle of attack earlier as well.

Keywords: Rigid wingsail, Stall, Camber, Crescent-shaped profile.

Acknowledgements

I wish to extend my gratitude to the people that have helped me in these past months to complete my masters thesis and want them to know that their help has been greatly appreciated.

I want to thank my examiner, Hua-Dong Yao as well as my supervisors, Heng Zhu, Bengt Ramne, Yu-Sheng Lee (Henry), Laura Marimon Giovannetti for their support which has been of great help to me and without which I could not have completed this thesis.

To Hua-Dong Yao I want to extend my gratitude for his invaluable insight and knowledge of aerodynamics, the cluster, STAR-CCM+ and ability to answer any question that I would bring to him. I also want to show my appreciation for his encouragements and steady availability and patience as well as his part in helping to set boundaries for and organize the thesis. His help and guidance have truly helped me on this final journey of my engineering degree and I have become better for it.

To Heng Zhu I am very appreciative of his continuous support and advice throughout all stages of my thesis. His many insights into aerodynamics and STAR-CCM+ have been very helpful and I am grateful for him and his willingness to spend the time to explain and straighten out all the questions I have had for him for these past months. His support has helped me to elevate both my work and myself and for that I am very thankful.

To Bengt Ramne I want to say that I am thankful for being given the opportunity to work on this very interesting thesis and for being able to visit and work at his office. His feedback and passion for this project has been a motivating factor for me to improve this thesis.

To Yu-Sheng Lee (Henry) I want to extend my thanks for lending me a hand whenever I would ask. His suggestions for camber became a key part of this work and I want to thank him for his feedback throughout the duration of this project which has contributed to this thesis.

To Laura Marimon Giovannetti I want to express my gratitude for her help in the very initial stages of this thesis, which established key parameters for this thesis. Parameters such as the geometry and chord length for the multi-element foil sails, wind speed and intervals between AoA.

I also want to thank my family and my friends at Chalmers who have supported me. This journey would not have been the same without you.

Lastly I want to dedicate this thesis to my grandmother, Tanja, who passed away while I was working on this project. Even though you and my other grandparents never got to see me graduate I know that you would all be proud of me. I love you and I miss you, your grandson, Erik.

Erik Ljungberg, Gothenburg, November 2023

List of Acronyms

Below is the list of acronyms that have been used throughout this thesis listed in alphabetical order:

AoA	Angle of Attack
CFD	Computational Fluid Dynamics
LES	Large Eddy Simulation
RANS	Reynolds-Averaged Navier-Stokes
SST	Shear Stress Transport
uRANS	unsteady Reynolds-Averaged Navier-Stokes
WASP	Wind-assisted ship propulsion

Nomenclature

Below is the nomenclature of indices, sets, parameters, and variables that have been used throughout this thesis.

Parameters

A_S	Sail area [m^2]
C_L	Lift force coefficient [-]
C_D	Drag force coefficient [-]
C_T	Thrust force coefficient [-]
F_D	Drag force [N]
F_L	Lift force [N]
F_T	Thrust force [N]
g	Gravitational acceleration [m/s^2]
p	Pressure [Pa]
V_{AW}	Apparent wind speed (inlet velocity) [m/s]
v	Flow velocity [m/s]
ρ_m	Material density [kg/m^3]
ρ_{air}	Air density [kg/m^3]
z	Height over given horizontal reference plane [m]

Variables

θ_{AW}	Apparent wind angle [°]
α	Angle of attack [°]

Contents

List of Figures

List of Tables

1
Introduction

A growing issue of the modern world is that of greenhouse gas emissions, and how to reduce them. One area in particular where there is potential to reduce the greenhouse gas emissions is the maritime transport sector, which currently is responsible for about 2.9% of total global greenhouse gas emissions [1]. Furthermore global shipping is responsible for the transportation of 90% of world trade by volume[2]. One of many possible solutions to facilitate the reduction of greenhouse gas emissions in the maritime transport sector is wind-assisted ship propulsion (WASP). However in order for WASP to be beneficial enough that it becomes relevant to implement it must be able to contribute to the ships propulsion under several conditions. In this report the conditions in question that will be studied are a range of angles of attack (AoA) as well as apparent wind angles. When talking about WASP there are several implementations, such as kites, rotor sails and rigid wingsails.

1.1 Report overview

The report is structured in the following way; first theory will be presented, in which the principles of sailing, airfoil theory and turbulence models are discussed. Thereafter the method, where the general approach is introduced, followed by how the simulations were made and the software in which they were simulated, as well as how the results were post-processed. Next the results are presented in the following order of sail design; Crescent-shaped profile, Two-element foil profile and the Three-element foil profile. For each type of sail there will first be a summary of the results for each AoA studied followed by a deep-dive for the best one. All 2D simulation results will be presented before the 3D results.

1.2 Background

As previously stated there are several implementations of WASP. For this project different setups of vertical airfoils, henceforth referred to as rigid wingsails, will be studied and compared to a crescent-shaped wingsail concept which has been developed by ScandiNAOS. In figure 1.1 a cross sectional view of the crescent-shaped wingsail concept is displayed next to two different types of rigid wingsails. A previous study comparing the crescent-shaped wingsail with a NACA 0015 profile showed promise for the crescent-shaped wingsail, as it generated substantially more thrust than the symmetrical NACA 0015 profile [3]. Therefore it is of interest to

compare the crescent-shaped wingsail with different setups of the sails shown in figure 1.1, given the clear geometrical differences between the sails.

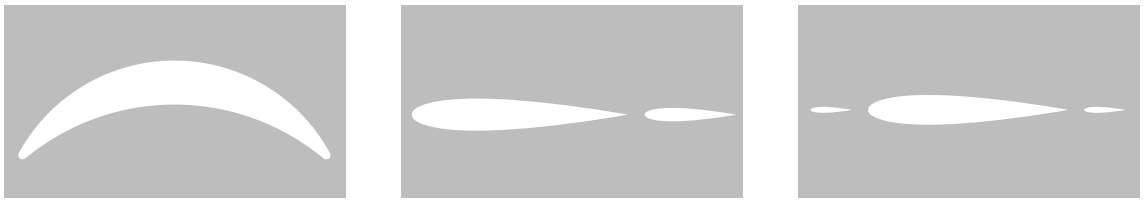

Figure 1.1: From left to right: A modified version of the crescent-shaped wingsail developed by ScandiNAOS, a two element foil sail replicating a concept used by Oceanbird, and a three element foil sail replicating a concept developed by BAR Technologies. Figures taken at angle of attack $\alpha = 0$.

1.3 Literature review

Several previous studies on WASP systems exists where the method of evaluation has been that of numerical simulations, which provide the ability to, with high accuracy, simulate and model complex CFD problems in real scale and also provide details about the characteristics of the flow through visualizations. One study [12] performed CFD simulations in STAR-CCM+ on a collapsible double-flap wingsail using the SST turbulence model, and utilizing the control variable method in order to find the best configuration of the wingsail. The gaps and the wing angles were varied and in the study it was found that the smallest gap distance of those studied yielded the best result.
Another study [13] utilized numerical simulations in ANSYS Fluent with the uRANS and $k - \omega$ SST models in order to study a two-element wingsail design. The paper aimed to understand the influence that geometric parameters had on the aerodynamic performance, and thus compared different rotating axis positions of the flap, flap deflection angles and flap thickness. The study found that at high camber with $\alpha = 6°$the lift would increase as the gap between the main wing and the flap decreased.
Lastly [14] developed an aerodynamic optimisation procedure for a double element wing configuration, a AC72 wingsail. Utilizing an iterative procedure that employs the RANS model and a velocity prediction program. The results of the analysis showed that out of the two gap distances between the trailing edge of the main and the leading edge of the flap, it was the smaller gap that yielded higher performance. It was also stated that, with the gap being set as a percentage of the chord, "...a difference of a few percent can lead to either attached flow on both the wing elements or to significant trailing edge separation on the main element and stall of the flap".

1.4 Aim

This project aims to study the three aforementioned concepts shown in figure 1.1 and in doing so, evaluate the overall aerodynamic performance. To, by studying an extensive range of angles of attack, reach a greater understanding in regards to the process of aerodynamic force generation and the flows. Another aim for this project as well is to uncover under which conditions and angles of attack that are critical, in the sense that stall will appear and also where maximum thrust is achieved. Lastly it is of course of interest to compare the three different concepts with each other to compare their performance.
The reason for the implementation of the two and three element airfoil rigid wingsails, constructed from NACA 0015 wing profiles in this report, is to see if the crescent geometry still performs better now that more factors that may influence the aerodynamic performance of the airfoil sails have been introduced, such as gap distances and camber angles. Furthermore from a practical point of view, operating sails that have the ability to alter their camber can be very beneficial, but also might be harder to implement since it means more moving parts.

1.5 Limitations

Due to limitations in both time and computational resources the selected range of AoA to be studied will be limited between 12 and 25 degrees. The reason behind selecting this particular range of AoA is because that is the range that sails are commonly operated in. Furthermore only one setup of the three element foil sail will be studied, that is the case with no gaps between the foils. The range of camber angles to be studied will be limited between 5 and 25 degrees, and will only be applied to the most promising cases of each sail setup. Additionally the simulation file and geometry for the crescent-shaped wingsail will be provided for both 2D and 3D simulations, and for all 3D simulations it is assumed that the apparent wind is a uniform flow. Also note that the influence of Reynolds number, wall roughness, flow compressibility and fluid-structure interaction will not be considered in this study. Lastly all simulations will be carried out for a singular constant chord length and wind speed for all sails.

2

Theory

This chapter will begin by discussing some of the principles of sailing, airfoil aerodynamics and important terms as well as different turbulence models that were used in this project.

2.1 The principles of sailing

For ships using rigid wingsails the propulsion of the ship, called the thrust, originates from loads on the sail due to wind. The thrust force acting on the sail is composed of a lift force and a drag force, both of which depend on the apparent wind speed, V_{AW}. The apparent wind speed is the speed experienced by an observer on the ship, in contrast to the true wind speed V_{TW} which would be experienced by a stationary observer. The figure below illustrates both apparent and true wind as well as the forces acting on a sailing ship.

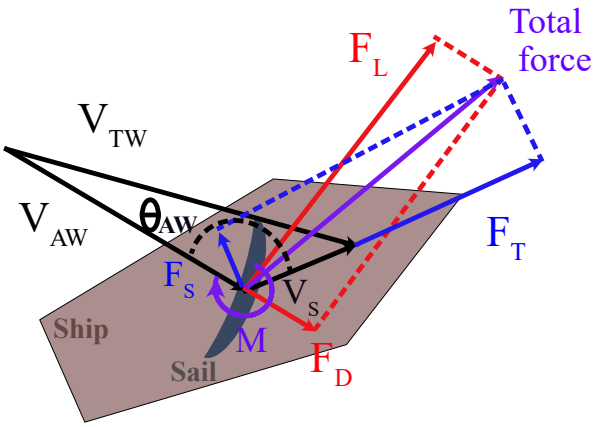

Figure 2.1: Illustration of different wind speeds and also forces acting on the sail. Remake of illustration borrowed from [3].

The forces outlined in red, F_D and F_L, are the drag force and lift force respectively. Both of which can be used together with the apparent wind angle θ_{AW} to calculate the thrust force F_T as shown in equation (2.1).

$$F_T = F_L \cdot sin(\theta_{AW}) - F_D \cdot cos(\theta_{AW}) \tag{2.1}$$

The force F_S perpendicular to the ship speed is the side force and does not contribute to the propulsion of the ship and "...causes heeling and rolling, as well as drift and additional induced resistance" according to [3].
In the CFD software that will be utilized the lift and drag force coefficients are exported, rather than the forces themselves. The lift, drag and thrust force coefficients are expressed in equations (2.2), (2.3) and 2.4 respectively.

$$C_L = \frac{F_L}{0.5\rho_m V_{AW}^2 A_S} \tag{2.2}$$

$$C_D = \frac{F_D}{0.5\rho_m V_{AW}^2 A_S} \tag{2.3}$$

$$C_T = \frac{F_T}{0.5\rho_m V_{AW}^2 A_S} \tag{2.4}$$

In this project the thrust coefficient is of particular interest but it will not be calculated as shown in equation (2.4). Instead the maximum potential thrust coefficient will be used and it is calculated as shown in equation (2.5). The reason that the maximum potential thrust was chosen was because no apparent wind angle was ever specified in any of the simulations. Since the apparent wind angle can come from many different directions it was of interest to calculate the maximum potential thrust from those possible directions.

$$C_T = \sqrt{C_L^2 + C_D^2} \tag{2.5}$$

The amount of forward propulsion that a ship can generate depends on the direction of the ship in relation to the wind direction, also called a point of sail. The points of sail can be divided into segments of 45°each. There are points of sail for which a ship cannot sail as it will eventually slow down to a stop, or be "in irons" as its called [5]. This is referred to as the "no-go zone" [4] which extends about 45°on either side of the direction of the wind, as illustrated in figure 2.2. When sailing as close to this 45°border as possible, it is said that the ship is "close-hauled". If the ship is sailed perpendicular to the wind, the ship is on a "beam reach" and if it is sailed at a 135°off the direction of the wind the ship is on a "broad reach". Finally if the ship is sailed at a 180°off the wind the ship is said to be "running downwind". Depending on the point of sail the ships sail will behave either as a wing, with lift being the dominant contributor to the ships propulsion, or as a parachute with drag as the dominant contribution. When the point of sail of the ship is between close-hauled and broad reach the sail will act as a wing, while it will act as a parachute if the point of sail is between broad reach and running downwind.

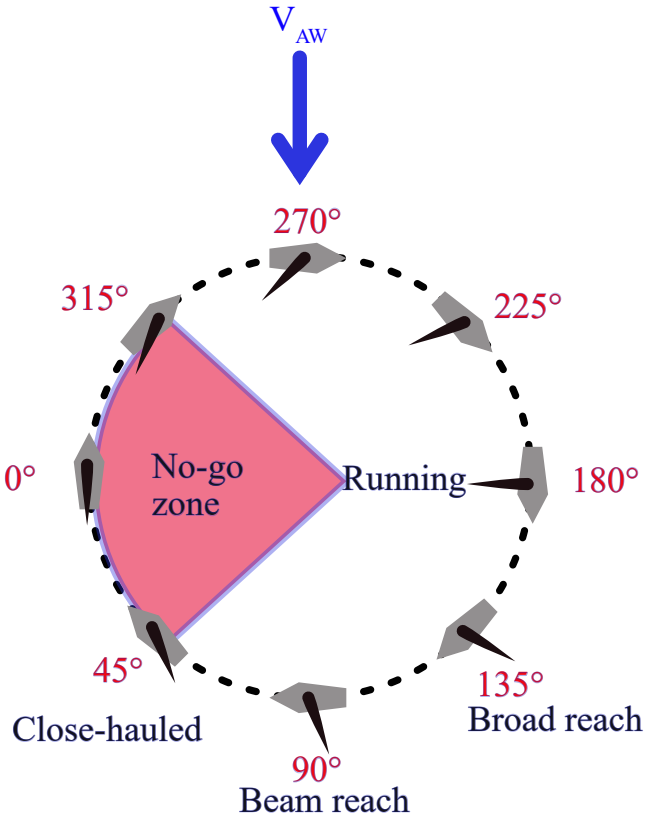

Figure 2.2: Illustration of the different points of sail and the no-go zone. Remake of illustration from [3].

2.2 Airfoil aerodynamics

This section will discuss briefly the aerodynamics of a airfoil and terms that will be used in this report. A airfoil is a shape that generates considerable amounts of lift while moving through a gas, in contrast to a hydrofoil which moves through water. An airfoil can be a propeller, turbine blade, a wing or a sail. The airfoil generates lift in part by pushing the incoming air downwards, and due to conservation of momentum the wing is lifted upwards. The loads that act on the airfoil are called lift and drag and act perpendicular and parallel to the relative free stream velocity respectively, as seen in figure 2.3. Note that in the case of the NACA 0015 profile which is symmetrical, it must be inclined, that is, have an AoA greater than 0, in order to be able to deflect the air downwards and generate lift. Also note that cambered airfoils are able to generate lift even at an AoA of 0°. The AoA is measured as the angle between the chord line and the direction of the relative wind, as seen in figure 2.4. The length measured along the chord line from the leading edge to the

trailing edge is called the chord length. In the case of the two and three element airfoils the chord length is measured as the sum of the individual chord lengths. In the case of a inclined NACA 0015 or a airfoil with camber, the airfoil is curved in such a way that the air on the lower surface of the wing decreases in velocity and thus an increase in pressure occurs. Meanwhile the air flowing on the upper surface of the wing increases in speed, thus decreasing the pressure. For a friction-less flow Bernoullis equation (2.6) states that a increase in velocity of the fluid happens in conjunction with a decrease in the pressure. Likewise a decrease in velocity happens in conjunction with a increase in pressure. This principle explains the pressure differences that can be observed over airfoils on whats called the pressure side, which is the underside of the airfoil, and the suction side which is the top of the airfoil.

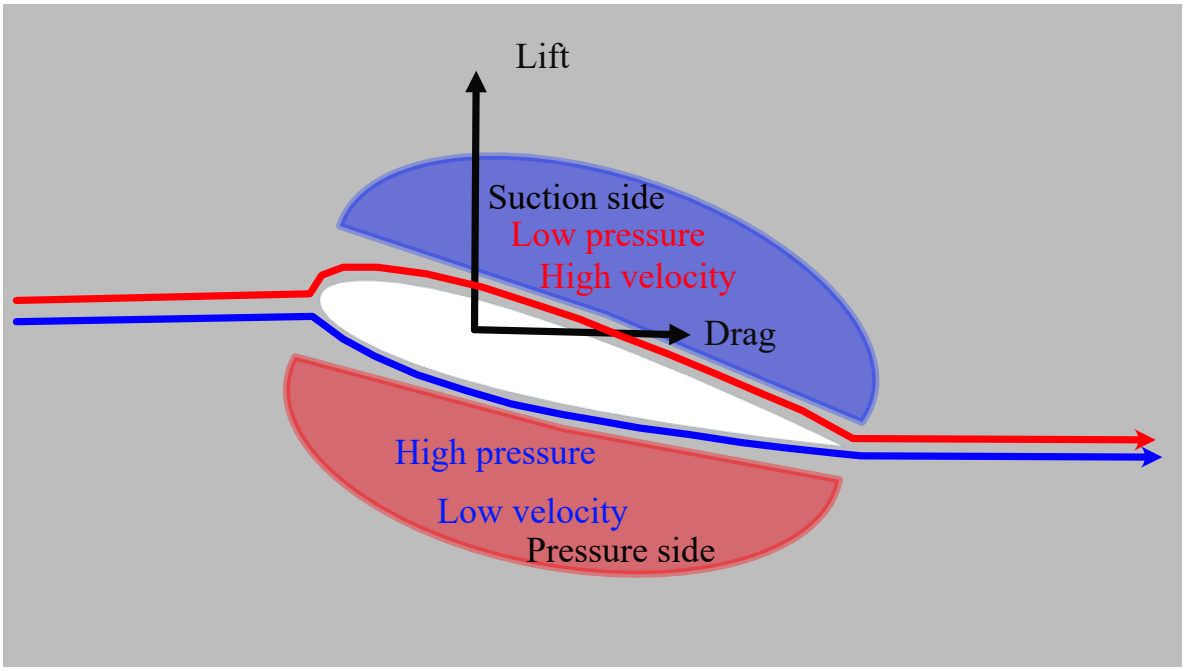

Figure 2.3: A NACA 0015 profile at an AoA of 16°.

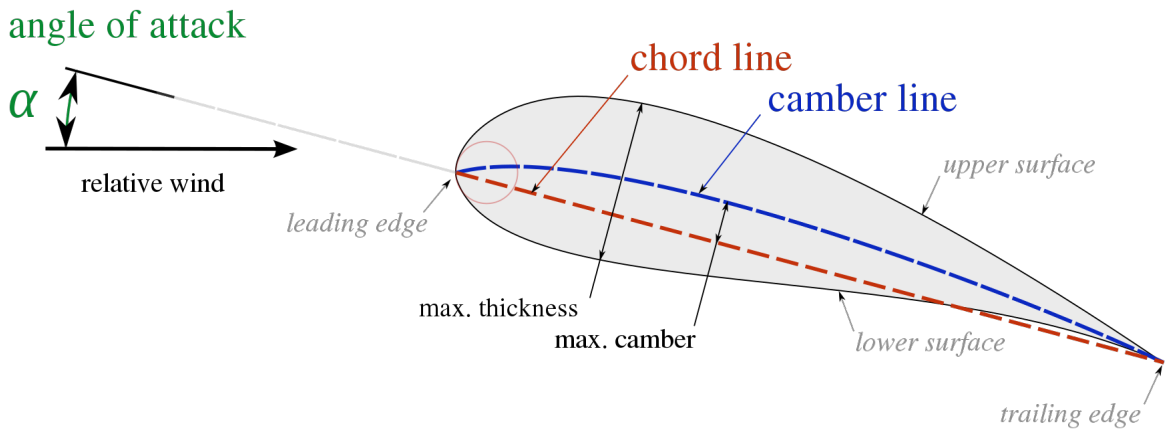

Figure 2.4: Airfoil nomenclature

$$\frac{v^2}{2} + gz + \frac{p}{\rho_{air}} = constant \tag{2.6}$$

Another important concept to discuss is that of stall. As previously mentioned airfoils are proficient at generating lift, and with increasing AoA follows increasing lift generated by the airfoil. However each airfoil has an angle called the critical angle of attack, where if the airfoil exceeds this critical angle then the lift generated by the airfoil will begin to decrease. This is referred to as stall and happens because the airfoil has generated its maximum lift coefficient value at the critical angle of attack, and increasing it further will thus lead to a decrease of the lift coefficient. The reason behind this decrease in lift is flow separation from the wing, which in turn is caused by an increase in pressure on the upper surface of the wing. This increase in pressure is referred to as something called the adverse pressure gradient, which is a positive gradient, $dp/dx > 0$, of the pressure distribution on the upper surface of the wing, and is created if the following holds true. If you have a geometry like an airfoil that is designed in such a way that it will increase the free stream velocity when the air flows on its upper surface, decreasing the pressure, until it reaches a maximum velocity and a pressure peak (through), and then decrease in velocity and increase in pressure as it moves along the upper surface of the airfoil and eventually rejoins the free stream flow at the end of the trailing edge, returning to ambient pressure. Then the positive increase in pressure as the air flows along the upper surface of the airfoil (the adverse pressure gradient) will try to slow the flow down again. If the adverse pressure gradient is great enough it will have enough force to push the boundary layer backwards, causing a re-circulation region and thus flow separation and stall [15]. For the NACA 0015 profile stall occurs somewhere between 12 and 15°AoA[6].

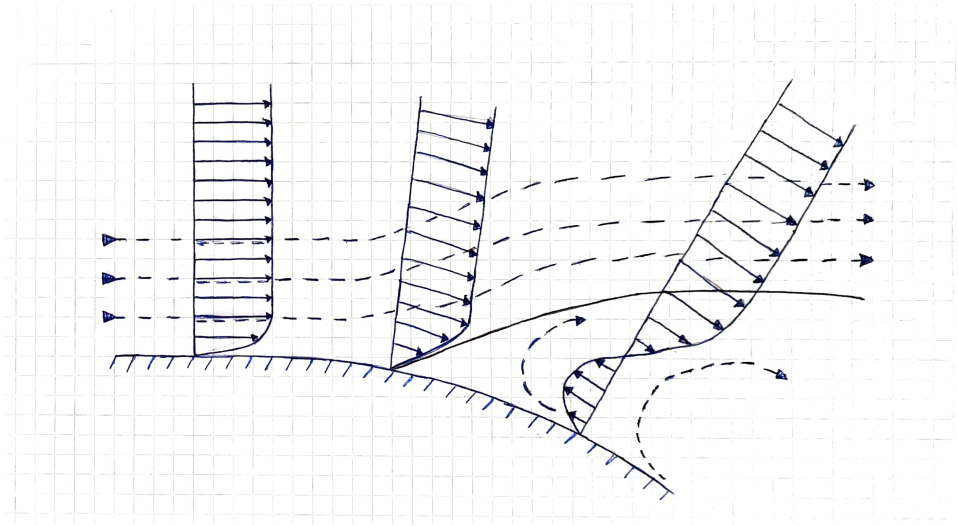

Figure 2.5: Sketch depicting the effect of the adverse pressure gradient if it is big enough

2.3 Turbulence models

This section will briefly discuss the turbulence models that are utilized in a subsection for each model. The models that will be discussed are the unsteady Reynolds-Averaged Navier-Stokes (uRANS), Large Eddy Simulation (LES) and $k-\omega$. Since one of the aims of this project is to try and identify the AoA at which the different sails experience stall, it is necessary to apply turbulence methods as stall is caused by flow separation on the suction side of the sail, which in turn is caused by the adverse pressure gradient which creates turbulent vortexes on the sails upper surface. Since it is unclear at which AoA that stall will appear, all simulations are run with turbulence models. Furthermore, due to the chaotic nature of vortex generation and propagation in space, it is also necessary to run the simulations as unsteady in order to obtain realistic results. Lastly a previous study[3] has found that the crescent-shaped wingsail experiences significant flow separation which in turn causes significant unsteady characteristics of the flow field.

2.3.1 uRANS and LES

Before talking about uRANS and LES it is helpful to first talk about Reynolds-Averaged Navier-Stokes (RANS). In turbulent flow the instantaneous variables such as velocity and pressure are decomposed into a mean and fluctuating value, as seen in equation (2.7).

$$v = \overline{v} + v' \tag{2.7}$$

Here $\overline{v}$ denotes the time averaged value and v' denotes the fluctuating value, and this decomposition is called a Reynolds-decomposition. Using the fact that $\overline{\overline{v}} = \overline{v}$ and $\overline{v'} = 0$[7] the Reynolds-decomposition will be applied to the Navier-Stokes equation for incompressible flow with constant viscosity, equation (2.8), and then all terms of

equation (2.8) will be time averaged. Note that the gravitation term $-\rho g_i$ has been omitted from equation (2.8).

$$\rho\frac{\partial v_i}{\partial t} + \rho\frac{\partial v_i v_j}{\partial x_j} = -\frac{\partial p}{\partial x_i} + \mu\frac{\partial^2 v_i}{\partial x_j \partial x_j} \tag{2.8}$$

The complete derivation will not be shown here, but what is important is the assumption that the mean flow $\overline{v_i}$ is steady, and thus the term $\frac{\partial(\overline{v_i + v_i'})}{\partial t}$ is zero. After derivations the equation can be written as:

$$\rho\frac{\partial \overline{v_i v_j}}{\partial x_j} = -\frac{\partial \overline{p}}{\partial x_i} + \frac{\partial}{\partial x_j}\left(\mu\frac{\partial \overline{v_i}}{\partial x_j} - \rho\overline{v_i' v_j'}\right) \tag{2.9}$$

Equation (2.9) is the time-averaged Navier-Stokes equation, or as it is often called, the Reynolds-Averaged Navier-Stokes equation. As a result of the Reynolds-decomposition the term $\rho\overline{v_i' v_j'}$ appears on the right hand side of equation (2.9) and is called the Reynolds stress tensor. This term is unknown and requires a model in order to solve for it, which in turn will allow the equation system (2.9) to be solved as there currently are more unknowns than equations. This problem of modelling the Reynolds stress tensor is referred to as the closure problem. The eddy viscosity model(s), which is a group or class of models used to calculate the Reynolds stress tensor, that has been used in this project is the later discussed $k-\omega$ SST (Menter, 1993) model.

As previously stated, in RANS the equations are time-averaged, but in LES the same equations are filtered (volume-averaged) instead, which means that the variables are a function of both space and time. The difference between the uRANS equations and the RANS equations is that in uRANS the unsteady term $\frac{\partial(\overline{v_i + v_i'})}{\partial t}$ from the Reynolds averaged equation (2.9) is retained, meaning that these variables as well are a function of both space and time. A big difference between uRANS and LES is where the models are efficient. "The basic idea in LES is to resolve (large) grid scales (GS), and to model (small) subgrid-scales" [7]. Therefore LES is good at resolving large eddies which can be found in wake flow where "...the flow is governed by large, turbulent structures, which can be captured by a fairly coarse mesh" [7]. However it is likely to get poor predictions in the boundary layer regions from the LES model unless a very fine mesh is used, which in turn can cause problems in said regions [7]. Conversely if the attached boundary layer is of importance, then the LES model can be substituted for the uRANS model. In uRANS, compared to LES, much more of the turbulence is modelled, while LES as previously stated only models small isotropic turbulent scales [7]. This means that the results from uRANS are generally less accurate. However it should be noted that LES is much more costly to simulate compared to uRANS.

2.3.2 $k-\omega$

The $k-\omega$ model is slightly different but quite similar to another model, called the $k-\epsilon$ model, as the purpose of both models is to calculate the turbulent viscosity μ_t. Both ω and ϵ describe the same physical event, that is the dissipation of turbulent

energy into thermal energy, which happens at very small scales (eddy sizes). However the reason that the $k-\omega$ model is favored here instead of the $k-\epsilon$ model is because the $k-\epsilon$ model over-predicts the shear stress in the presence of adverse pressure gradients[7], which often occur on airfoils. Furthermore the $k-\omega$ model not only predicts adverse pressure gradient flow better than the $k-\epsilon$ model, but the $k-\epsilon$ model has to make use of empirical damping functions while the $k-\omega$ model does not require any near-wall modifications[7]. It is worthwhile to note that there exists several versions of the $k-\omega$ model, but the one that will be utilized in this project is the $k-\omega$ SST (Menter, 1993).

2.3.3 $k-\omega$ SST

So far it seems like the $k-\omega$ model is superior to the $k-\epsilon$ model, but the drawback of the $k-\omega$ model is that it is dependent on the free stream value of ω [9]. The $k-\epsilon$ model on the other hand does not suffer from this drawback, so in an attempt to improve on both of the models it was suggested to combine them both[10]. The $k-\omega$ Shear Stress Transport (SST) model makes use of blending functions to smoothly switch between the models. If the cells are close to the wall then the $k-\omega$ model will be applied, and if the cells are far away in the free stream then the $k-\epsilon$ model will be applied. Likewise a blend of the two functions is utilized at intermediate distances from the wall.

3

Methodology

This chapter will explained the different methods employed in this project. From the general method or plan of action, to how computations were set up and carried out, and how the results were post processed.

3.1 General method

As was previously stated in the background and limitations chapters, a comparison between three different types of sails will be made, and studied in a small range of both AoA and camber angles. For the two and three element foils sails there are gaps between the aft, (middle) and front foils as can be seen in figure 1.1. Three different setups of gap distances listed below will be studied for the two element foil, whereas for only the first of these, the three element foil will be studied.

- No gap
- 5% gap
- 10% gap

Note that the gap distances refer to percentages of the total chord length.

Furthermore different ratios between the foils will be studied as well. Three different kinds of ratios will be studied for the two element foil sail, while only the ratio 15:70:15 will be studied for the three element foil sail. The ratios refer to the chord length of each foil in terms of percentage of the total chord length. That is, the front and aft foil will be 15% of the total chord length and the middle foil will be 70% of the total chord length. The ratios studied for the two element foil sail are listed below:

- 70:30
- 80:20
- 90:10

To help visualize the ratios of the gap distances and chord lengths of the foils, please see figure 3.1 below.

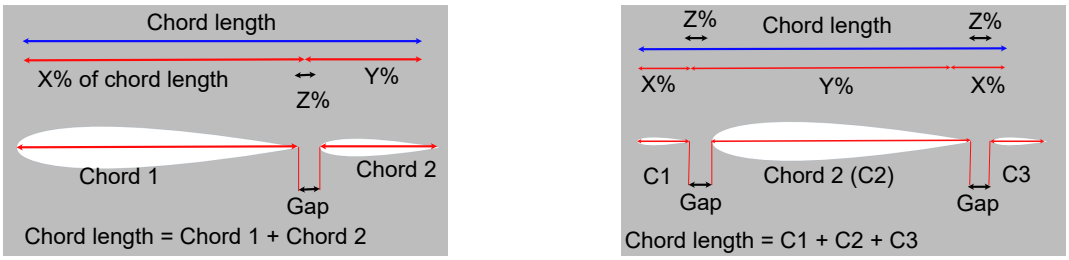

(a) Two element foil sail **(b)** Three element foil sail

Figure 3.1: Gap and chord length ratios visualized

The total chord length shown in the figures 3.1 (a) and (b) above as well as the chord length in figure 3.2 below was set to 14 meters for all rigid wingsails studied in this paper. However the specifics of the crescent-shaped profile have yet to be mentioned. The crescent profile that was studied in this thesis was the D2R8 profile, meaning that the sail has a mast diameter of 2m and a suction-side arc radius of 8m, as can be seen in figure 3.2.

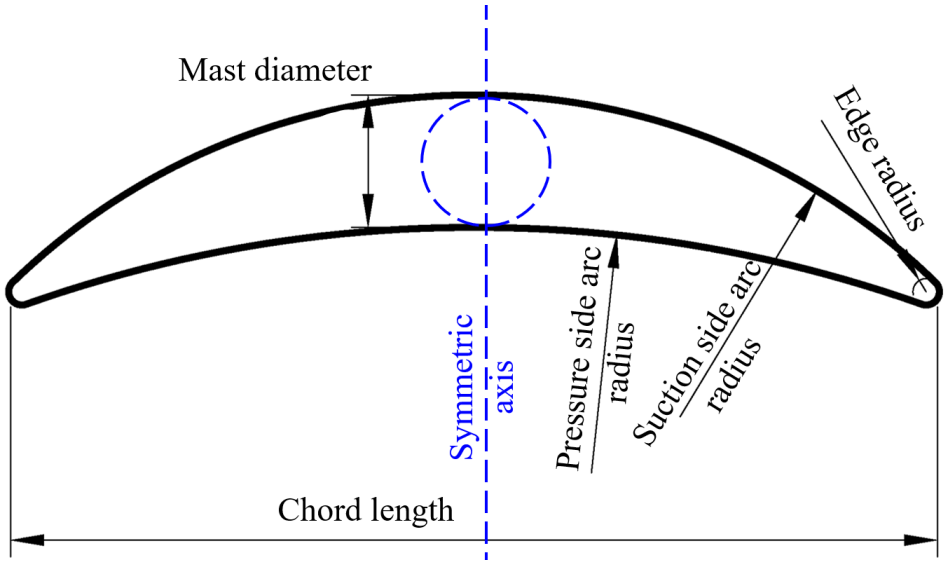

Figure 3.2: Dimensions of the crescent D2R8 profile, image taken from [3].

It is also helpful to know that camber will not be defined as in figure 2.4, but rather as in figures 3.3 (a) and (b). Note that if the camber angle is set to, say 15 degrees, then both the angles in figure 3.3 (b) are set to 15 degrees.

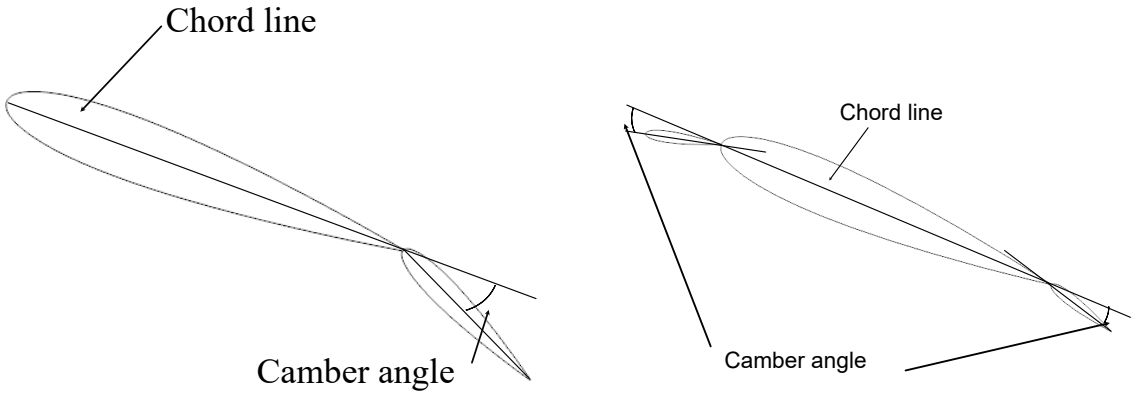

(a) Two element foil sail **(b)** Three element foil sail

Figure 3.3: Definition of camber for the multi-element foil designs visualized

Initially all simulations will be computed without any camber angle between the foils in order to get a baseline value. The second step is to identify the effects that gap distance has on the performance of the sails, and choose the most promising gap distance for further study. When the gap distance has been chosen, the AoA that yields the greatest maximum potential thrust will be chosen to study the effects of camber angles. Finally, for each ratio configuration of the sails, with the best gap distance and camber angle combination, will be compared with each other, including the crescent-shaped sail at the AoA that yields the greatest maximum potential thrust. Since the crescent-shaped sail is of special interest a 3D simulation will be carried out for it, as well as for the two or three element foil configuration that yielded the best results from the comparison.

3.2 Computation

Due to the vast quantity of simulations that are to be made, coupled with the hardware requirements to run these simulations in a reasonable length of time, a cluster was utilized for all simulations. The cluster used was the Tetralith cluster, provided by the Swedish National Infrastructure for Computing (SNIC). 2D simulations for the different wingsail concepts between 12 and 18 AoA were computed using 32 cores with a stopping criteria of a maximum of 10 inner iterations. Simulations for a AoA of 18.5 and greater were also simulated with 32 cores and a maximum of 10 inner iterations, but were given twice as much time to simulate. The reason for the latter cases of simulations being simulated for a longer duration is to give the flow time to fully develop, as these AoA are closer to the believed area where stall appears. All 3D simulations utilized 128 cores, which was the maximum amount possible.

3.3 STAR-CCM+

In this project the commercial software STAR-CCM+ (Version 2210) [11] will be utilized to perform all CFD simulations, both 2D and 3D. This section will thus be split into two parts, one for the 2D simulations and one for the 3D simulations, each part detailing how the simulation was set up.

3.3.1 2D simulation set up

All cases were simulated as turbulent and transient with an inlet flow speed of 8 m/s and the models used in the 2D simulation were as follows:

- Reynolds-Averaged Navier-Stokes
- $k - \omega$ SST [8]
- Implicit Unsteady[1]

3.3.1.1 Fluid domain, 2D

Before introducing the domain in more detail the coordinate system and location of origo for the crescent-shaped profile will be introduced, which will facilitate the understanding and interpretation of some of the results later in the report.

(a) Representation of global coordinate system in 3D

(b) Representation of global coordinate system in 2D

Figure 3.4: Location of origo, and global coordinate system for the crescent-shaped wingsail

The fluid domain consists of two regions referred to as the inner and outer region and encompass the sail and the entire domain excluding the sail respectively. These regions are discussed later as they are linked to different sets of boundaries. The

[1]For more information on this model, please see the STAR-CCM+ user guide

length of the 2D rectangular domain is 700m with a width of 400m, and the flow direction and coordinate system is illustrated in figure 3.5, with the sail at a distance of 200m from the left edge of the domain, at origo.

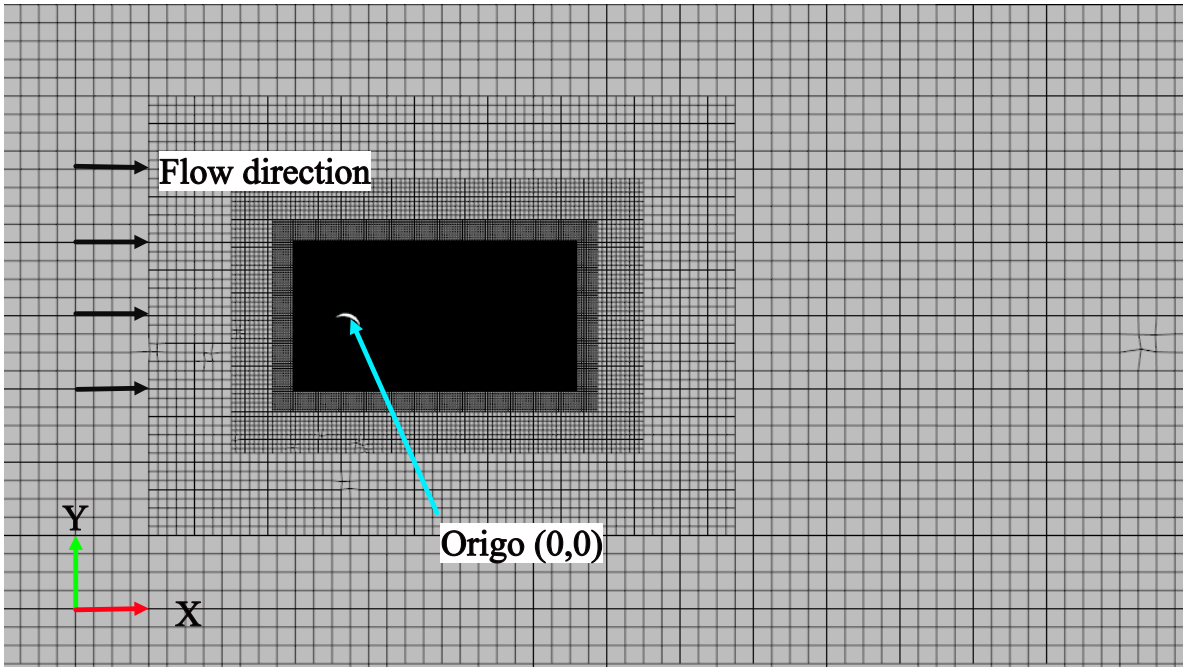

Figure 3.5: Fluid domain for the 2D simulation cases

3.3.1.2 2D Boundaries

The boundaries at the sides and back of the domain are set as pressure outlets, while the front boundary is set as a velocity inlet, and the bottom boundary is set as a symmetric boundary. These boundaries are part of the region called outer, and the no-slip wall boundary that is imposed on all parts of the sail are part of the inner region. The inner region is encircled in figure 3.7 with the label Near-foil refinement.

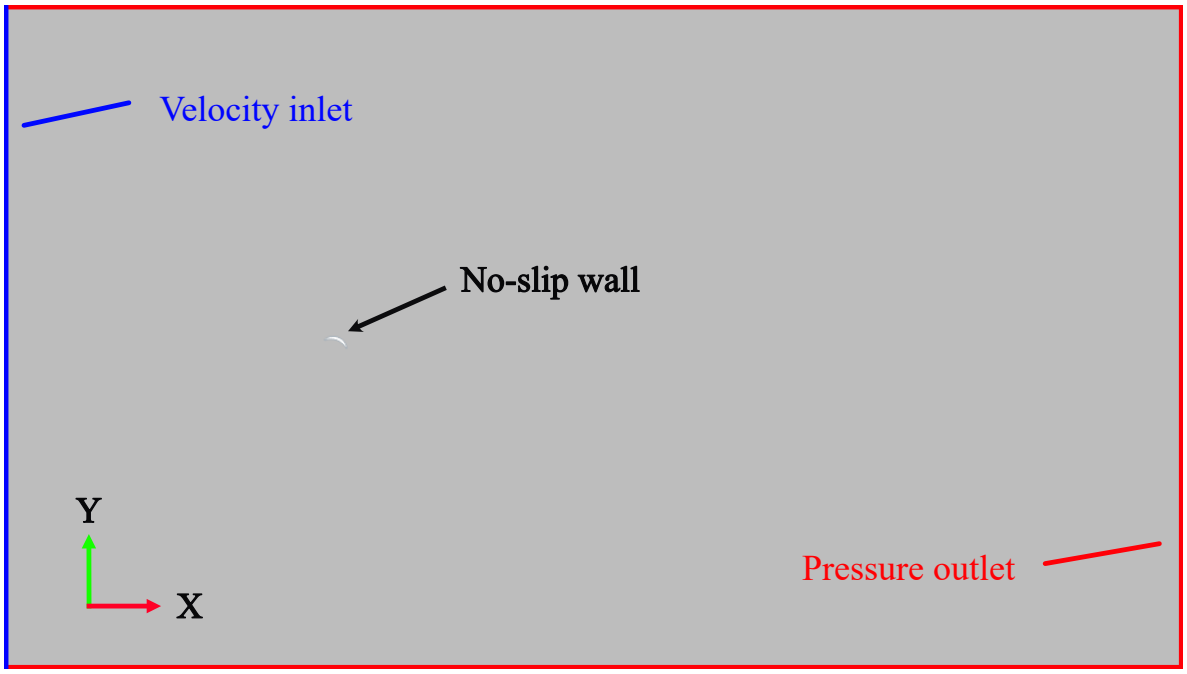

Figure 3.6: Locations and types of boundaries for the 2D simulation cases

3.3.1.3 2D Mesh

When generating the mesh for the geometry, a near-foil refinement was added as well as a wake refinement and a downstream refinement, and of course a mesh covering the entire domain. In the case of the near-foil refinement, the following meshers were utilized:

- Surface Remesher
- Trimmed Cell Mesher
- Prism Layer Mesher

In STAR-CCM+ there is something called the base size and target surface size which are both utilized here when setting up the mesh. The base size is set by the user and is a characteristic dimension of the model that is then used to set other values relative to the base size. The value set by the target surface size is that which it aims for in the absence of a mesh refinement and its value is in this case relative to the base size. The prism layer mesher used a geometric progression stretching function with a wall thickness distribution mode. The target surface size was set to 20 % of the base, which was set to 0.5m, yielding a target surface size of 0.1m. The number of prism layers were set to 55 and the prism layer near wall thickness was set to $1 \cdot 10^{-5}m$ with a prism layer total thickness of 0.5m. The prism layer near wall thickness and the thickness of the prism layer can be observed in figure 3.8.
For the mesh that covers the entire domain a trimmed cell mesher is utilized with a target surface size of 2000 % of the base size, yielding a 10m target surface size. In regards to the wake refinement the surface size is set to be 20% of the base, and for the downstream refinement the surface size is set to be 60% of the base. See figure 3.7 below that outline the wake and downstream refinement as well as the near-foil refinement.

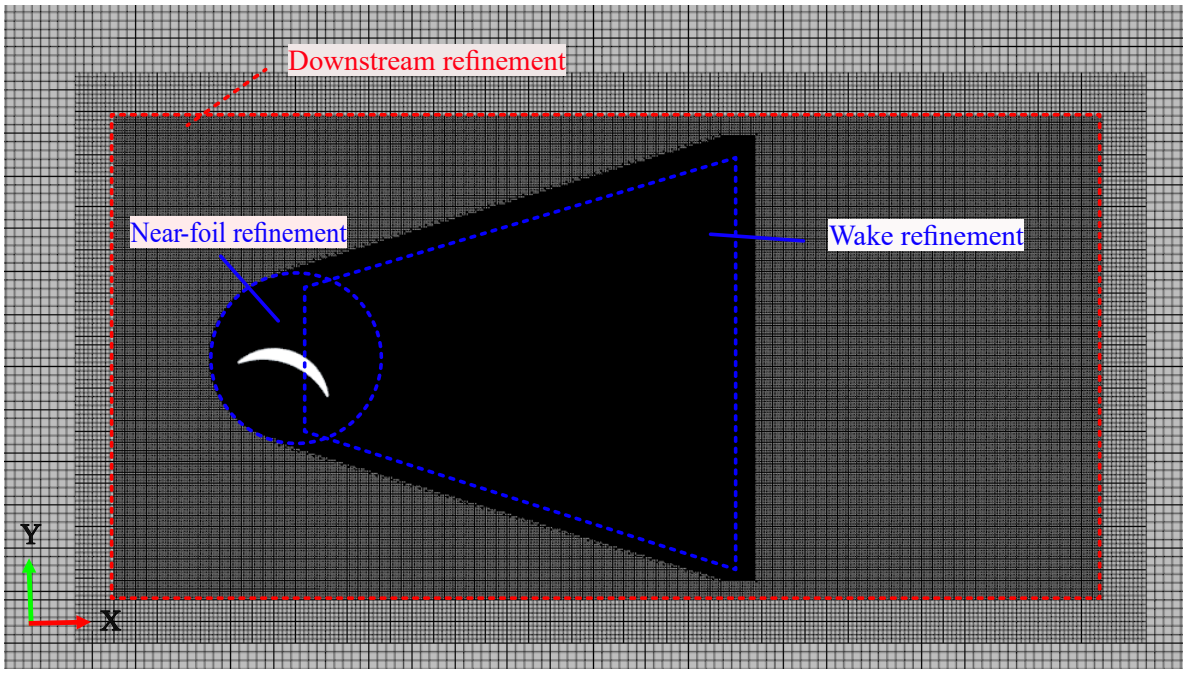

Figure 3.7: Downstream, wake and near-foil mesh refinement used in 2D simulations

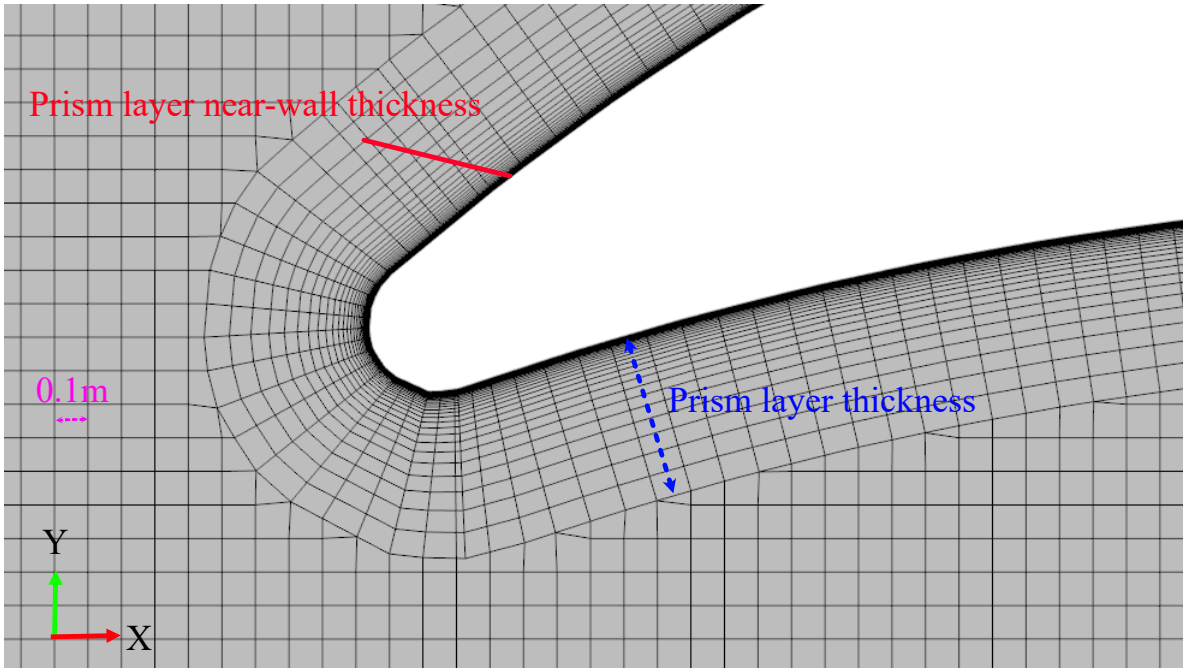

Figure 3.8: Close up of near-foil refinement and prism layers used in 2D simulations

The number of cells used in the 2D simulation were 619108.

3.3.2 3D simulation setup

In the case of 3D simulations the same models and inlet flow speed of 8 m/s were used once again. However this time, the Reynolds-Averaged Navier-Stokes model was only used in the beginning of the simulation. After roughly five periods could be observed in the lift coefficient plot data the model was swapped for the LES model for the remainder of the simulation.

3.3.2.1 Fluid domain, 3D

Unlike the 2D case there is only one region covering the entire domain. The domain is also slightly smaller in the x-y plane with a width of 300m, a length of 600m and the depth is 300m. Furthermore the sail, which is extruded to a length of 72m, is now 150m from the inlet.

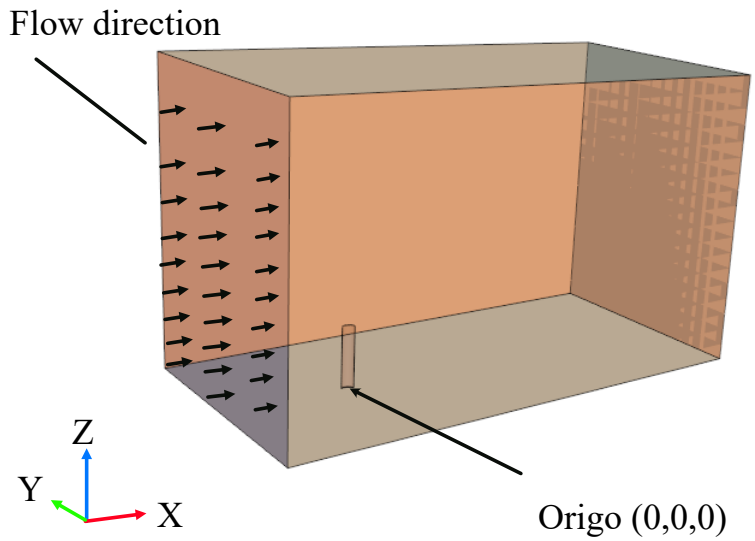

Figure 3.9: Fluid domain for the 3D simulation cases

3.3.2.2 3D Boundaries

In contrast to the 2D simulations which used a rectangular domain, a cubic domain was used for the 3D simulations, as seen in figure 3.14. Once again the boundaries at the sides and back of the domain are set as pressure outlets, as illustrated in figure 3.10, and the front boundary is set as a velocity inlet and the top and bottom as symmetric boundaries, as illustrated in figure 3.11.

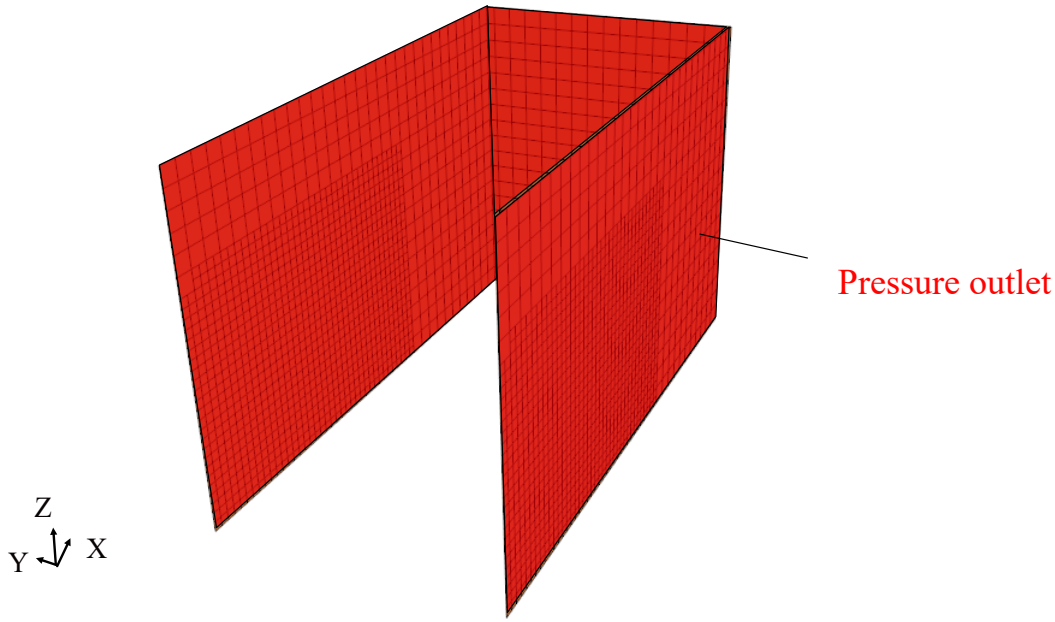

Figure 3.10: Pressure outlets of the cubic domain

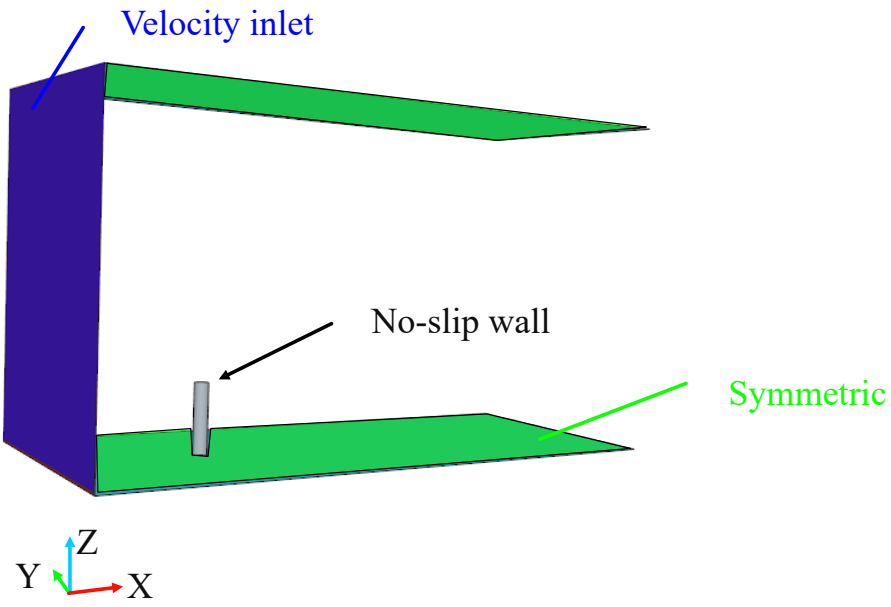

Figure 3.11: Velocity inlet, wall boundary and symmetry planes of the cubic domain

3.3.2.3 3D Mesh

Similar to the 2D simulation setup there is a near-foil refinement, a wake refinement and a downstream refinement, which can be observed in figure 3.12. Additionally there is also a near-edge refinement for the leading and trailing edges of the wing,

which can be observed in figure 3.13. In the case of the two element foil setup there will also be a refinement enclosing the trailing edge of the front wing and the leading edge of the aft wing. In contrast to the 2D simulation case there is only one mesh for the entire domain of the 3D geometry, as can be seen in figure 3.14, and the meshers that are used are:

- Surface remesher
- Trimmed Cell Mesher
- Prism Layer Mesher

Like before the prism layer mesher uses a geometric progression stretching function with a wall thickness distribution mode. The target surface size is set to be 2000% of the base size, which this time is set to be 1m. The number of prism layers have been increased to 65 and the prism layer near-wall thickness have been decreased to $6 \cdot 10^{-6}m$, while the prism layer total thickness have remained the same at 0.5m.

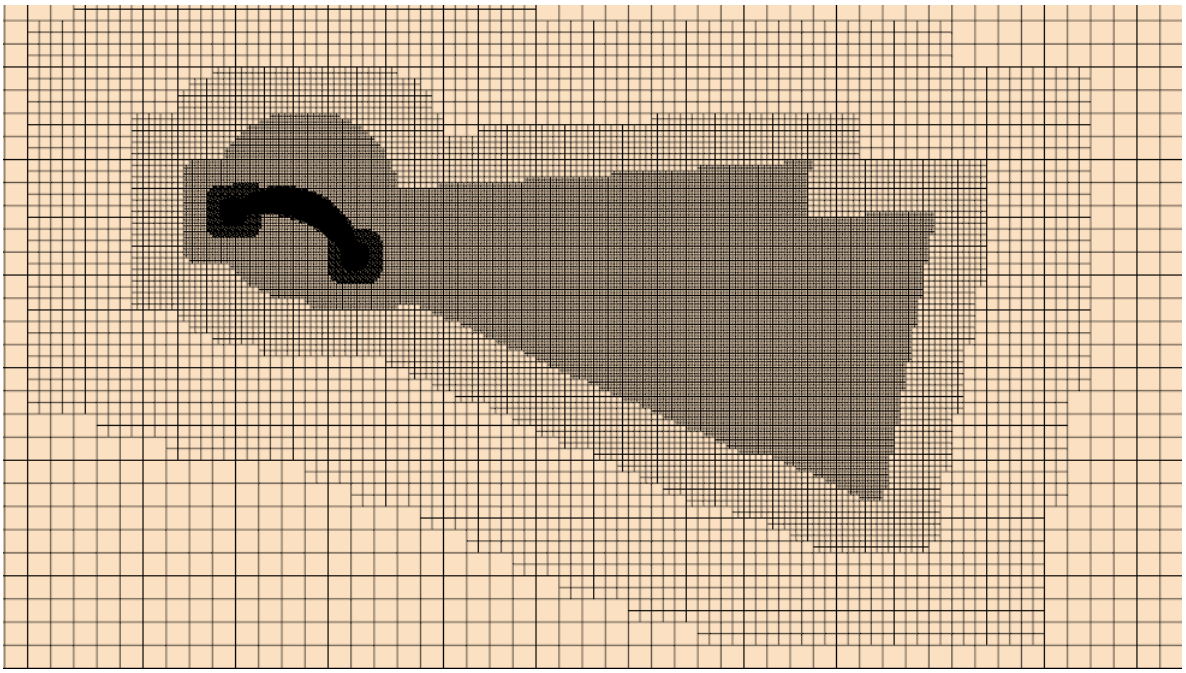

Figure 3.12: Wake and near foil mesh refinements for the 3D case, taken at a sectional plane at the half span of the sail.

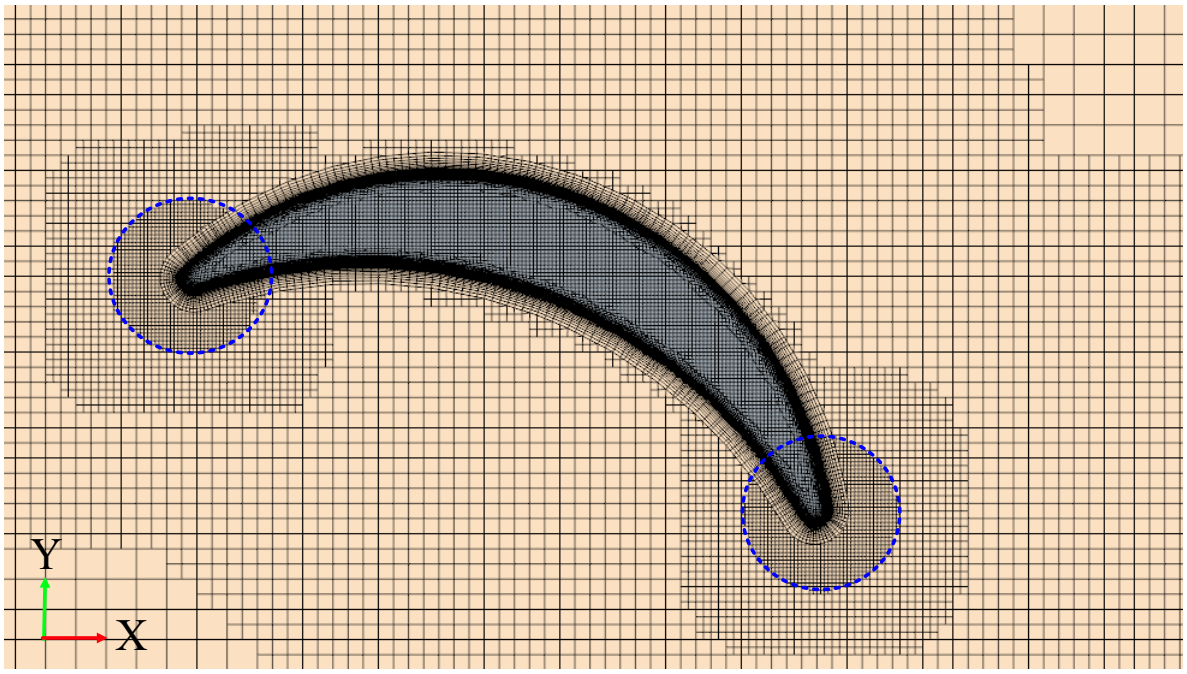

Figure 3.13: Highlight of the added refinements to the leading and trailing edges, , taken at a sectional plane at the half span of the sail.

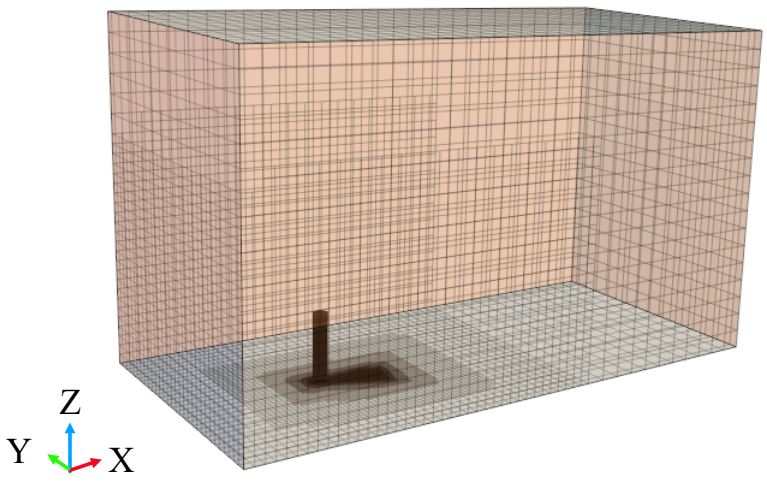

Figure 3.14: Entire meshed domain of the crescent 3D simulation case

The number of cells used in the 3D simulation were 21,252,242.

3.4 Post processing

This section will discuss the process of the post processing. Note that no post processing of the results was made in STAR-CCM+, only exporting of the results.

3.4.1 Matlab

The programming language Matlab, version 2022b, was used for processing all of the results from STAR-CCM+. This program was chosen mainly due to my familiarity with the language.
Initially the post processing script that was written would load in the csv files of the force coefficient data, and then do the following steps:

- Begin at the very end of the file, that is, at the last physical time simulated
- Identify whether or not the data has converged
- In case of convergence, set the time-averaged force coefficient value to the last observed value.
- In case of no convergence, calculate the time-averaged force coefficient values from three seconds until the last physical second simulated.

The script is automated to load in both drag and lift coefficient data for all simulated AoA and plot and save the appropriate graphs afterwards. The polar plots were created by using the previously mentioned equation 2.1 to calculate the thrust coefficient at different apparent wind angles. To clarify, the thrust coefficient that is shown in the polar plots, for any wingsail, is calculated by inserting the time-averaged force coefficients of the lift and drag force, from the csv file that represents the AoA that yielded the greatest maximum potential thrust according to equation 2.5, into equation 2.1 and varying the apparent wind angle.

4

Results

In this chapter the results for the full range of AoA for all sails are condensed into mostly graphs and the most promising AoA for each sail is further examined. First all the results for sail with no camber, with the exception of the crescent-shaped wingsail, will be presented followed by some comparative plots of those results, followed by the cambered results and again some comparative plots. Note that for all line plots containing the thrust coefficient, it has been calculated according to equation (2.5), excluding the polar plots. In the case of the polar plots the thrust is calculated as in equation (2.1), with the force variables exchanged for the respective coefficients.

4.1 Crescent

Presented below are results from the 2D simulations of the crescent-shaped sail as well as post processing results, regarding the full range of angles of attack.

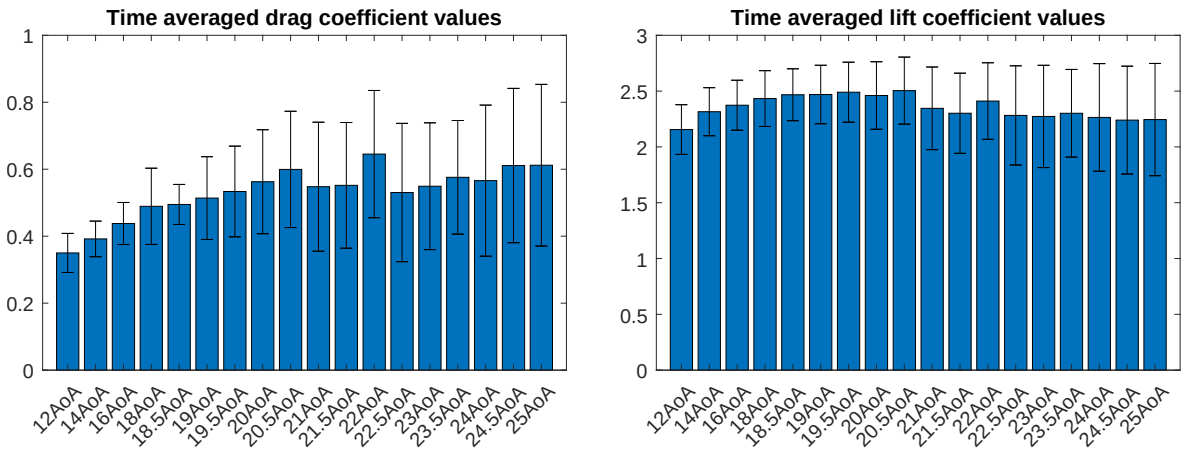

(a) Drag force coefficients

(b) Lift force coefficients

Figure 4.1: Time averaged force coefficient values

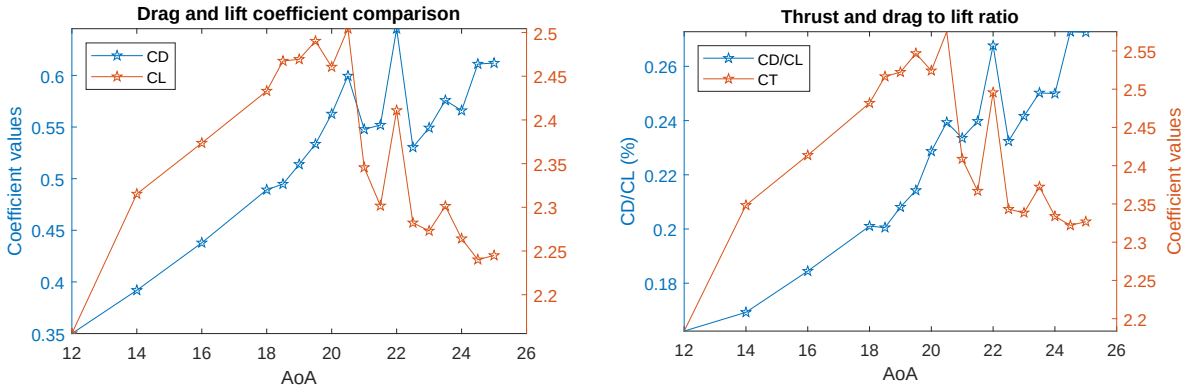

(a) Comparison of coefficients

(b) Thrust and size relation between coefficients

Figure 4.2: Time averaged force coefficient values, with the thrust calculated as in equation (2.5).

From figure 4.1 it can be seen that the drag coefficients seem to oscillate more overall compared to the lift coefficients. The time-averaged lift coefficient values in figure 4.1 (b) are quite similar to those found in a previous study[3] for a crescent-shaped wingsail with different camber, although those coefficient values are slightly larger, peaking around 2.6 for 19°AoA. Furthermore in figure 4.2 (a) there is no obvious AoA for which the wingsail stalls, unlike for a single NACA profile where stall is easy to identify. Instead there is rather than one critical angle of attack, a range of stall from 19.5°to 24°AoA where loss of lift can be observed. However, in this range of stall a peak in lift can be observed at 20.5°AoA, followed by a significant drop, which if one were to try and identify a singular stall angle, then 20.5 AoA would be the most likely.

The following table presents the AoA where the greatest thrust coefficient values were achieved

AoA	20.5AoA	19.5AoA	20AoA
C_T	2.5751	2.5468	2.5241

Table 4.1: The three greatest thrust coefficient values in descending order and the respective AoA

4.1.1 20.5AoA

Here is a more in-depth look at the AoA which yielded the greatest maximum potential thrust. For clarification, the Q-criterion (shown in figure 4.3) is used to indicate whether the flow is vorticity dominated (positive values) or strain dominated (negative values).

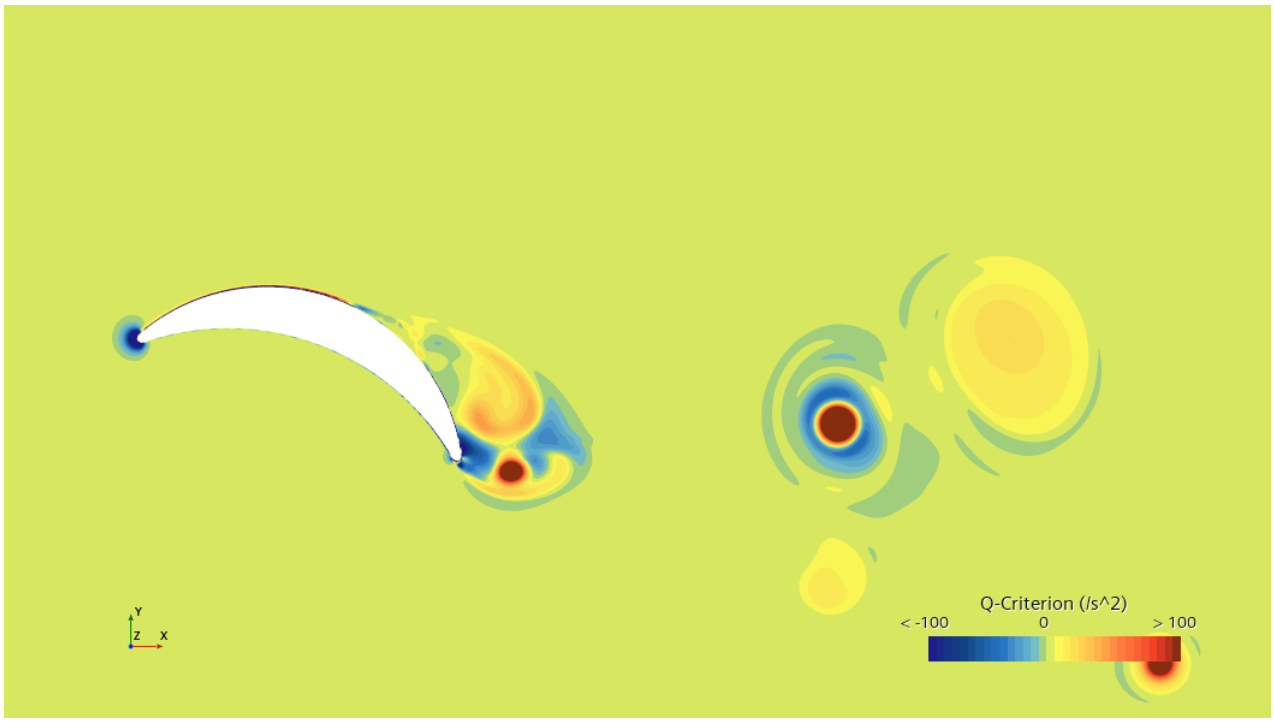

Figure 4.3: Q-Criterion at 47 000 iterations

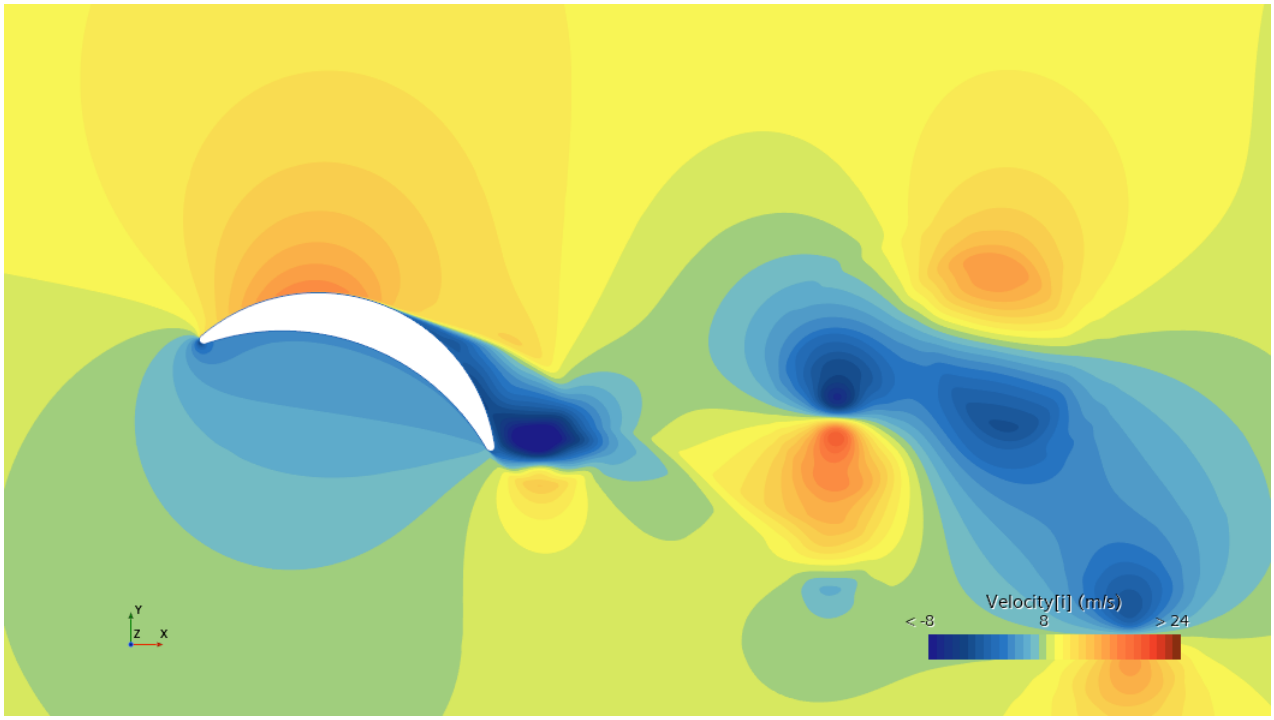

Figure 4.4: Velocity at 47 000 iterations

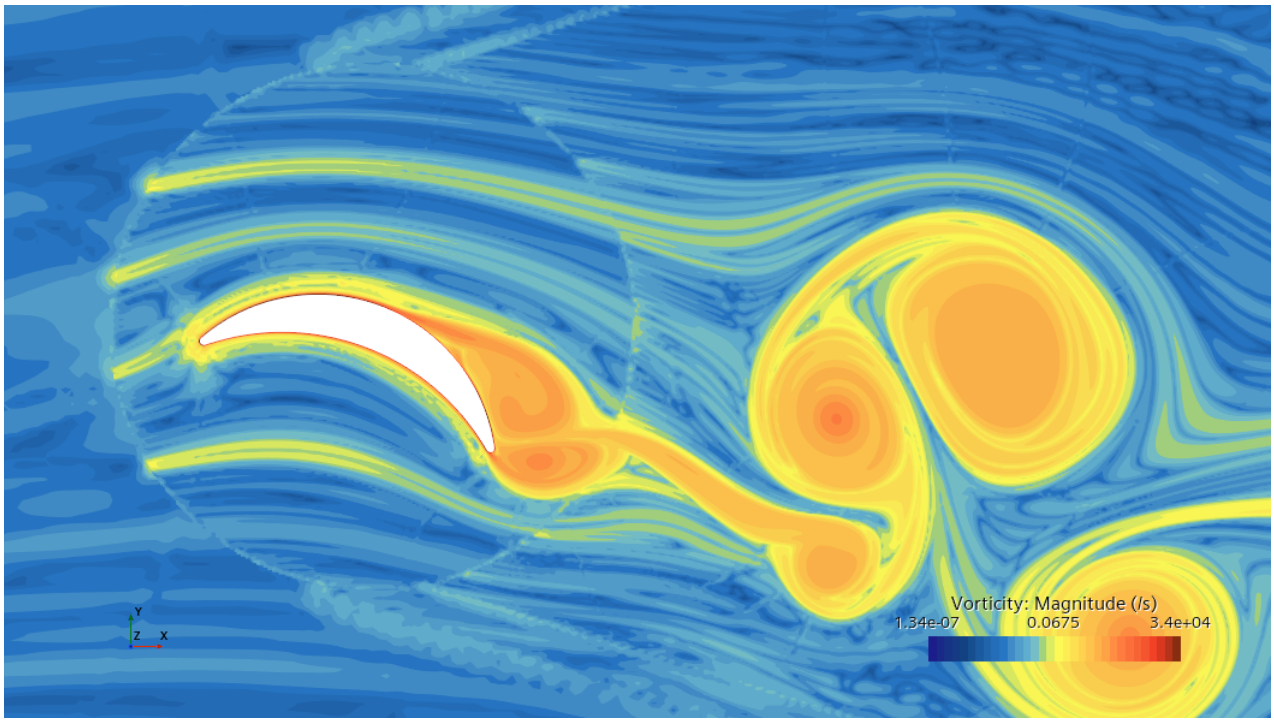

Figure 4.5: Vorticity at 47 000 iterations

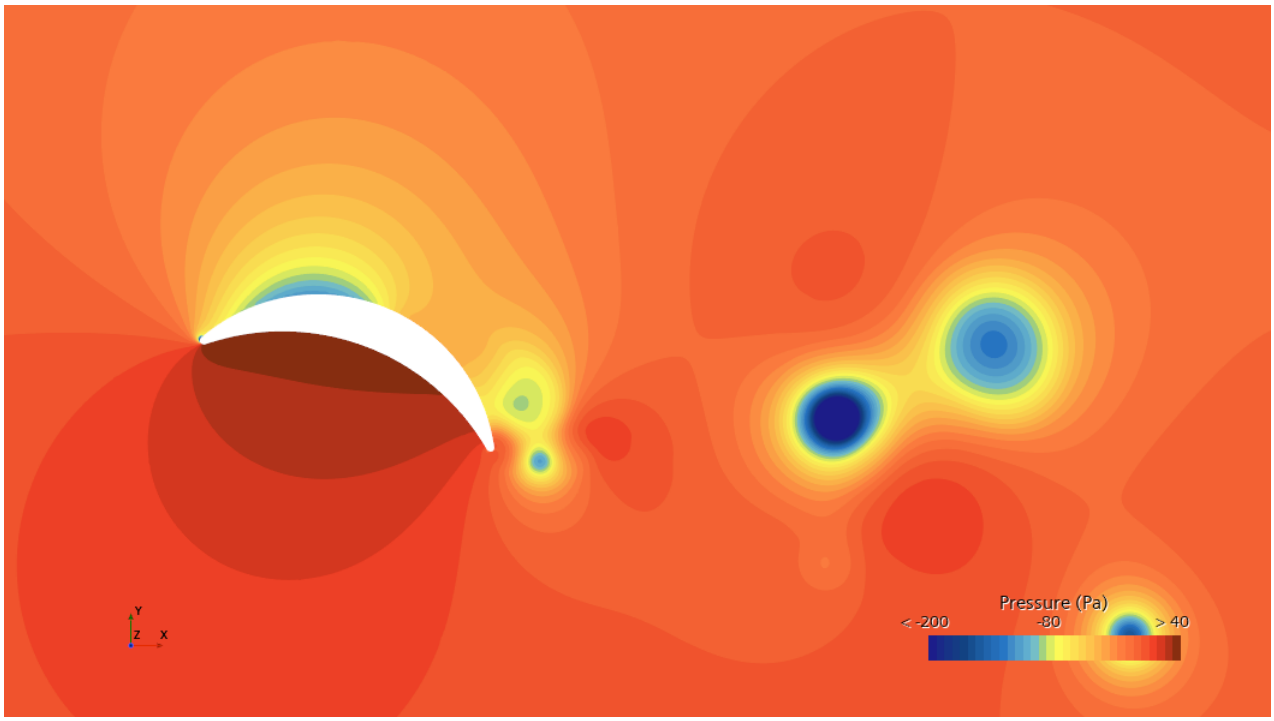

Figure 4.6: Pressure at 47 000 iterations

As can be seen in figure 4.4 the flow at the upper surface of the sail speeds up and then slows down significantly, suggesting a high adverse pressure gradient is present. Figure 4.5 confirms this as flow separation is visible and consequently some

large vortexes can be observed in the wake of the sail. Furthermore in figure 4.3 it can be seen from the positive Q-values that the flow is mostly vorticity dominated, especially a bit of the trailing edge, with strain dominating the flow right at the trailing and leading edges.

4.2 Two Foil

This section presents the results from the two foil element sail design for the different chord length configurations, in combination with different camber angles, AoA and gap distances as well.

4.2.1 Baseline values

In this section all baseline values for the two element foil wingsails will be presented, that is, simulation results for the designs without any camber angle.

4.2.1.1 Ratio 70/30 with no gap and no camber

Below the results for different AoA are presented for the setup of the two element foil sail with a chord length ratio of 70 and 30 for the front and aft foil respectively. In the setup of the simulations the distance between the aft of the bigger foil and the front of the smaller foil was set to be zero.

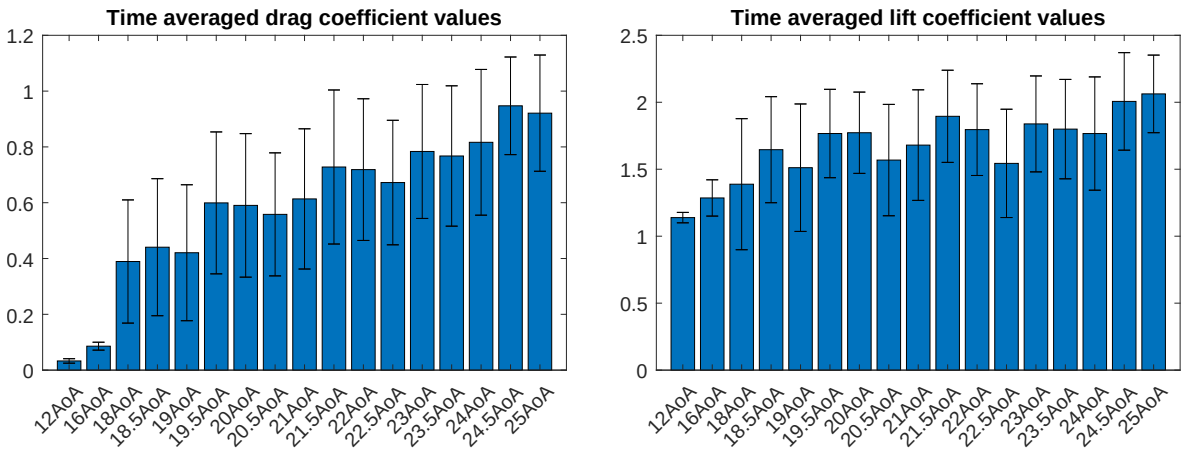

(a) Drag force coefficients **(b)** Lift force coefficients

Figure 4.7: Time averaged force coefficient values

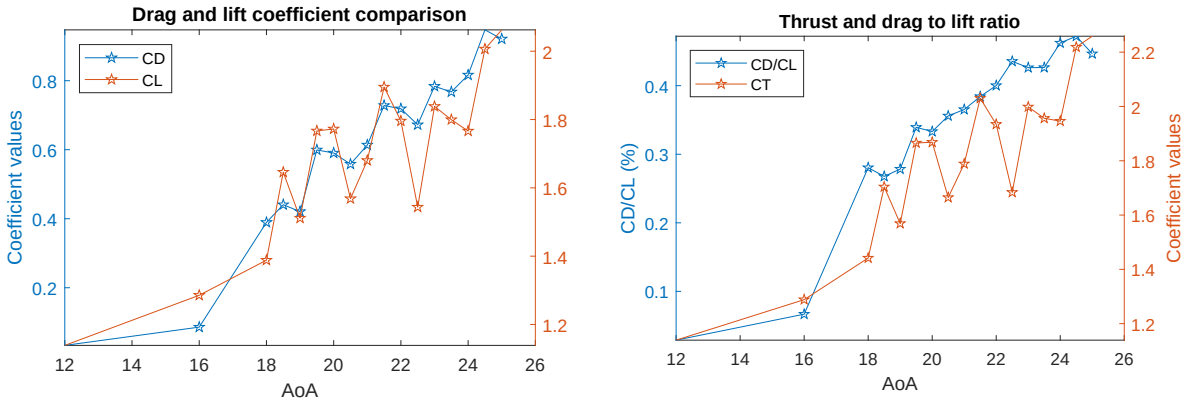

(a) Comparison of coefficients

(b) Thrust and size relation between coefficients

Figure 4.8: Time averaged force coefficient values

Just as for the crescent-shaped wingsail, from figure 4.7 it looks like the drag coefficients oscillate more than those of the lift. The keen observer might have noticed that the data point for 14 AoA is missing from both figures 4.7 and 4.8. This is due to a mistake in the simulation file which was discovered to late to be able to correct it, rendering the results from this simulation invalid. In figure 4.8 (a) an increase in lift can be observed up until 18.5 AoA after which several points where a loss of lift occurs can be observed. Once again, just like in the case of the crescent-shaped wingsail there is a range of stall between 18.5°and 23.5°AoA where several points with loss of lift can be observed, with the largest consecutive loss of lift occurring after 21.5 AoA. However, unlike the crescent-shaped profile the largest lift is not achieved at the AoA where, when exceeded, the largest loss of lift or consecutive loss of lift can be observed. Instead, outside this range a peak in lift appears at 25°AoA which makes this the more likely stall angle as its the maximum lift observed. Stating that the most likely stall angle is outside of the observed range of stall might seem contradictory, but since there is no data from this study from greater AoA it can't be known if the lift will increase or decrease after 25°AoA, hence why it's the most likely given the data available.
The following table presents the AoA where the greatest thrust coefficient values were achieved

AoA	25AoA	24.5AoA	21.5AoA
C_T	2.2588	2.2188	2.0302

Table 4.2: The three greatest thrust coefficient values in descending order and the respective AoA

4.2.1.1.1 25AoA Here is a more in-depth look at the AoA which yielded the greatest maximum potential thrust.

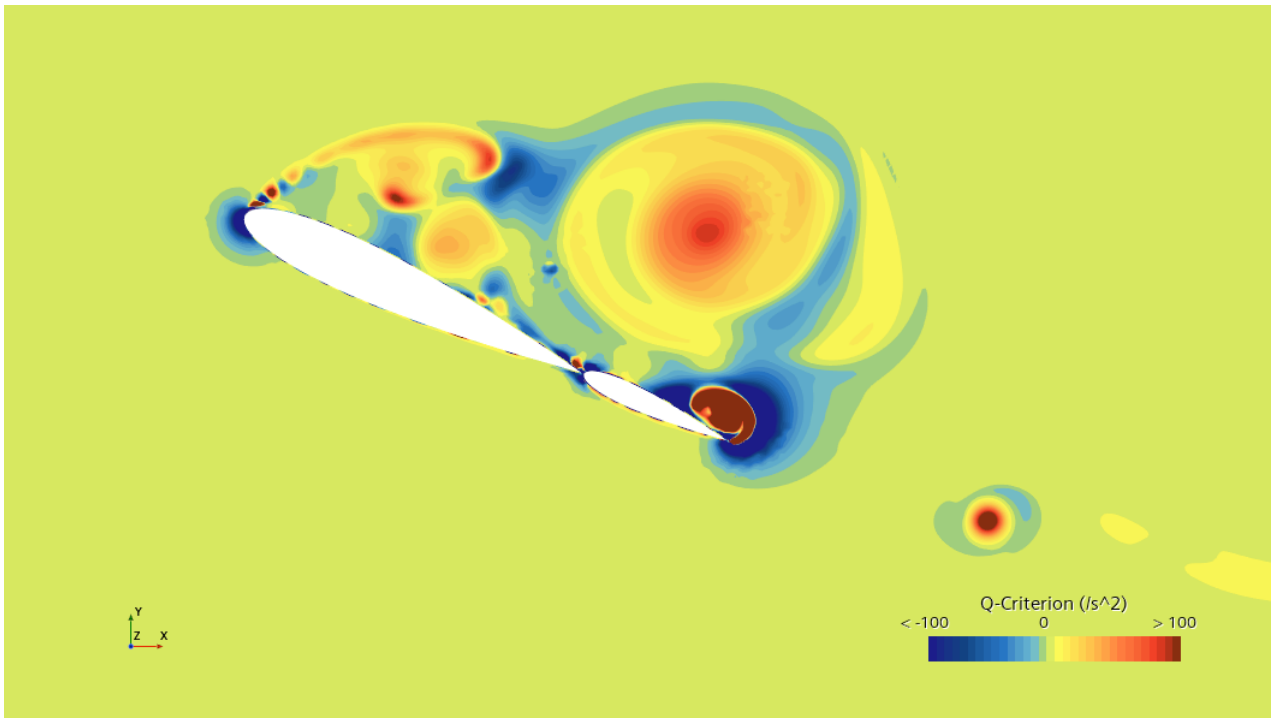

Figure 4.9: Q-Criterion at 60 000 iterations

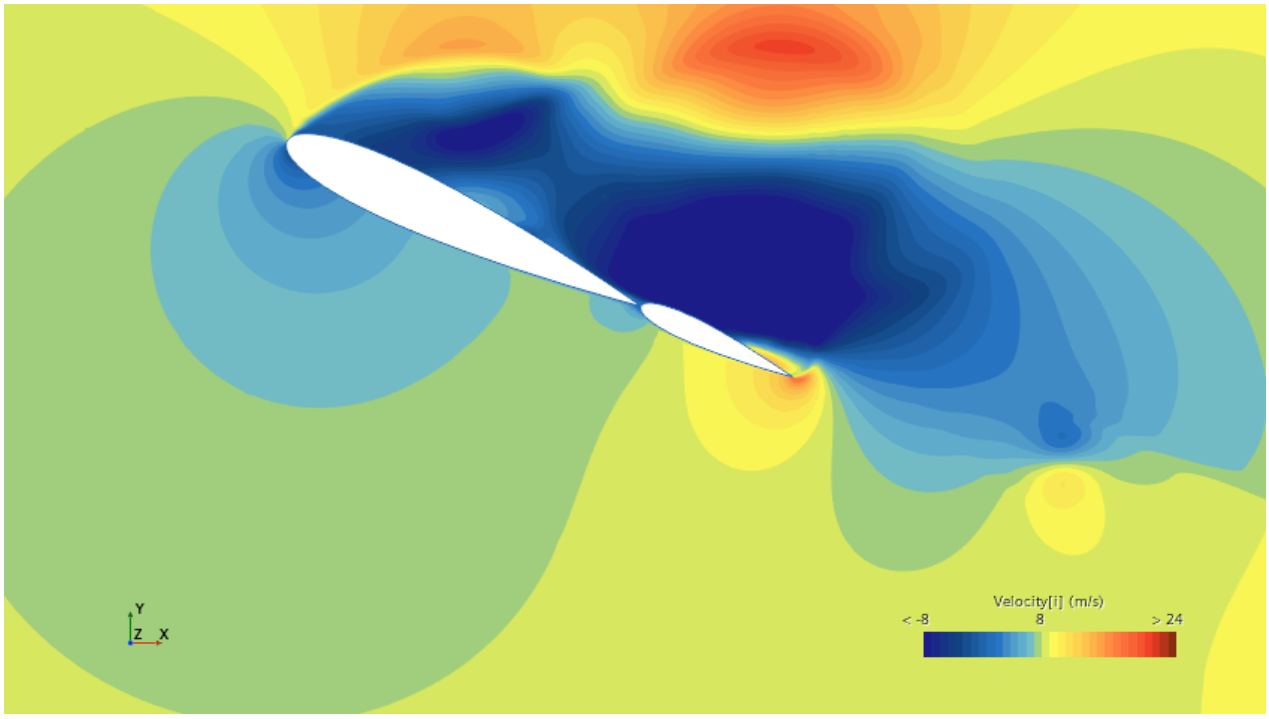

Figure 4.10: Velocity at 60 000 iterations

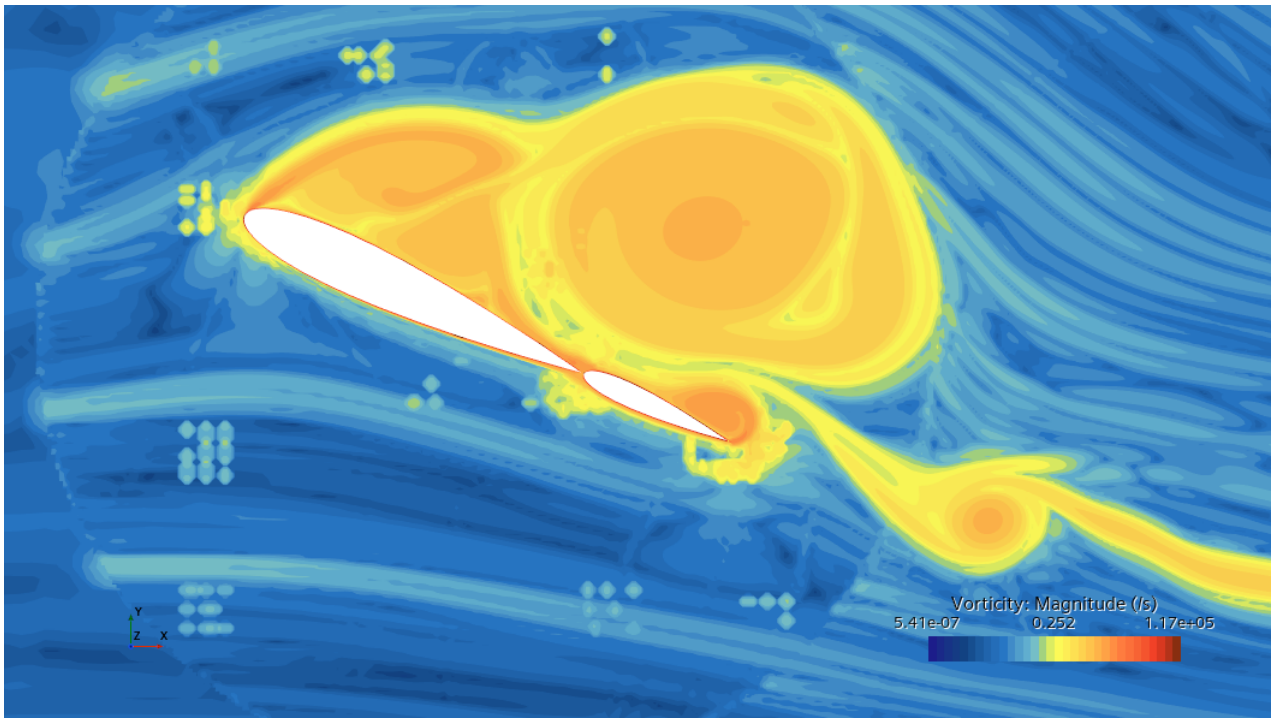

Figure 4.11: Vorticity at 60 000 iterations

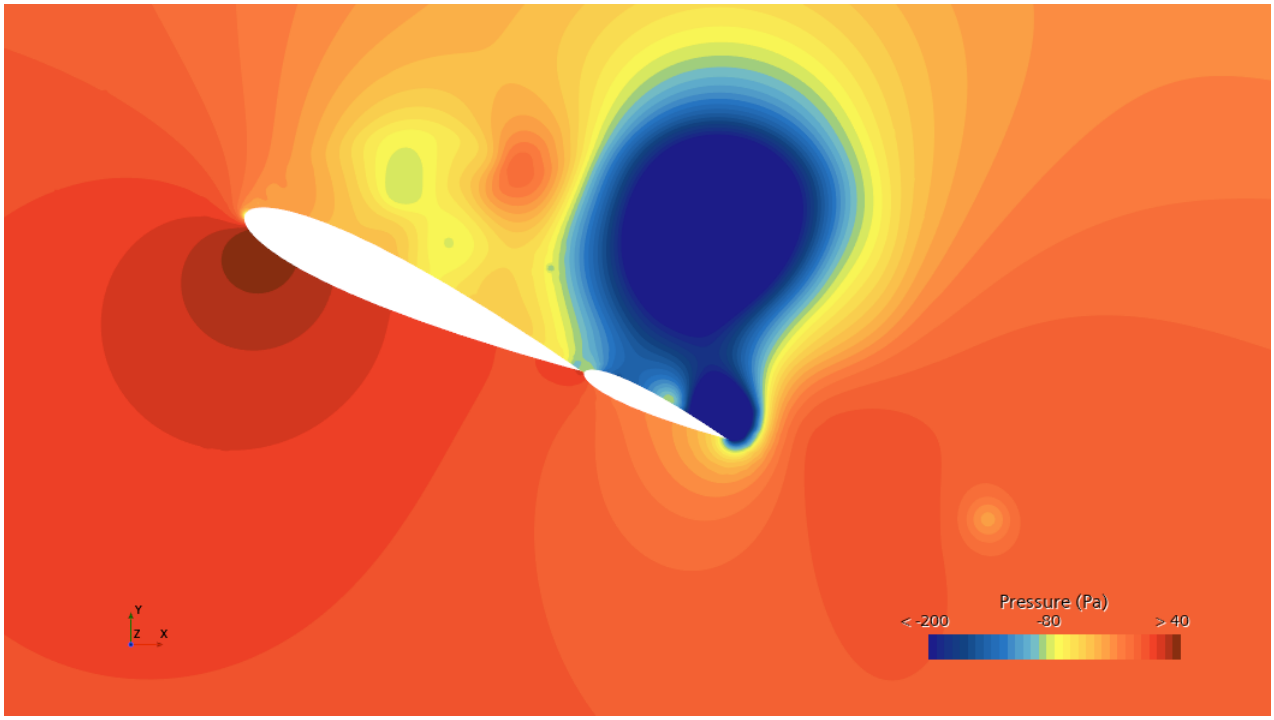

Figure 4.12: Pressure at 60 000 iterations

In figure 4.10 a decrease in velocity on the bigger foil can be observed at the leading edge, which then increases further along the lower surface of the sail until it reaches about the leading edge of the smaller foil, where the velocity decreases again with

an increase at the tip of its trailing edge. On the upper surface of the bigger foil the velocity does increase, however not with as steep of a gradient as for the lower surface. This can be hard to discern from the velocity figure alone but can be inferred from the pressure plot in figure 4.12. The high velocity a bit above the smaller foil does explain the large suction created at that position when looking at the pressure plot. Furthermore, looking at the pressure plot there are two spots with significantly low pressure surrounded by regions of higher pressure, which might cause some re-circulation. Looking at figure 4.11 it can be seen that the flow separates at the leading edge of the bigger foil with a large vortex above the smaller foil. Figure 4.9 also shows vortexes (positive Q) at the leading edge of the bigger foil and in the large low pressure region above the smaller foil, as well as at the trailing edge of the smaller foil.

4.2.1.2 Ratio 70/30 with 5% gap and no camber

Below the results for different AoA are presented for the setup of the two element foil sail with a chord length ratio of 70 and 30 for the front and aft foil respectively. In the setup of the simulations the distance between the aft of the bigger foil and the front of the smaller foil was set to be 0.7m, or 5% of the total length of the airfoils.

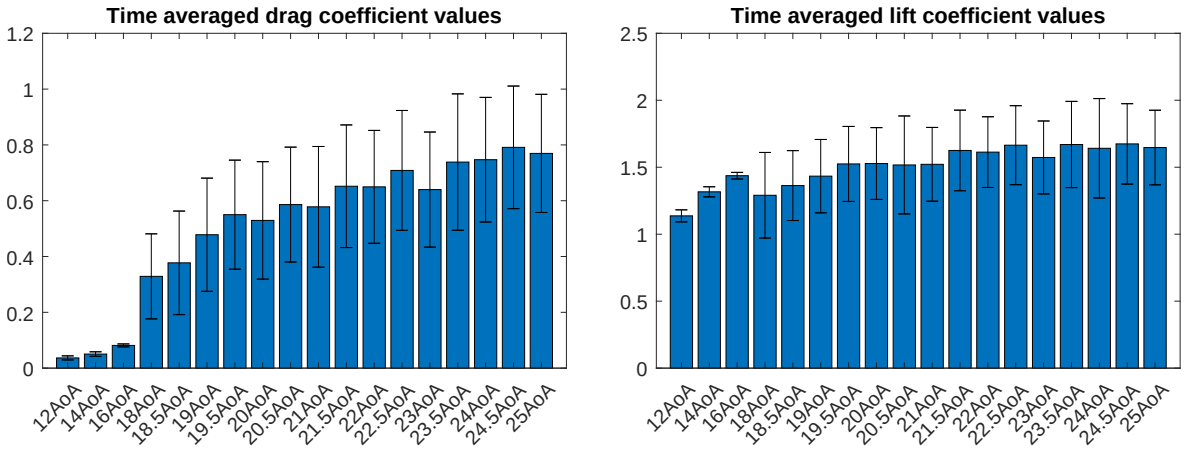

(a) Drag force coefficients

(b) Lift force coefficients

Figure 4.13: Time averaged force coefficient values

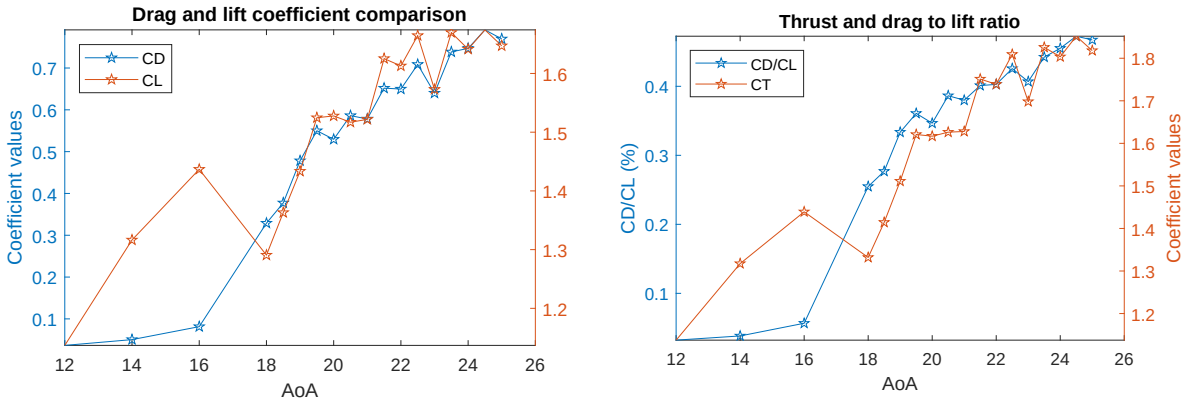

(a) Comparison of coefficients

(b) Thrust and size relation between coefficients

Figure 4.14: Time averaged force coefficient values

As before, by studying figure 4.13 it seems like the drag oscillates more than the lift. Furthermore from figure 4.13 (b) and 4.14 (a) the greatest loss of lift is observed when the AoA is increased beyond 16 °, which would suggest that this is the critical angle of attack. However since the maximum lift occurs at 24.5°AoA this is the more likely stall angle. As was also observed previously there is a range of stall with an onset at 16°AoA, which is earlier than for the prior configuration, and ends at 24.5°AoA. Lastly, an interesting plateau in the lift can be observed between 19.5 and 21°AoA.

The following table presents the AoA where the greatest thrust coefficient values were achieved

AoA	24.5AoA	23.5AoA	25AoA
C_T	1.8518	1.8257	1.8180

Table 4.3: The three greatest thrust coefficient values in descending order and the respective AoA

4.2.1.2.1 24.5AoA Here is a more in-depth look at the AoA which yielded the greatest maximum potential thrust.

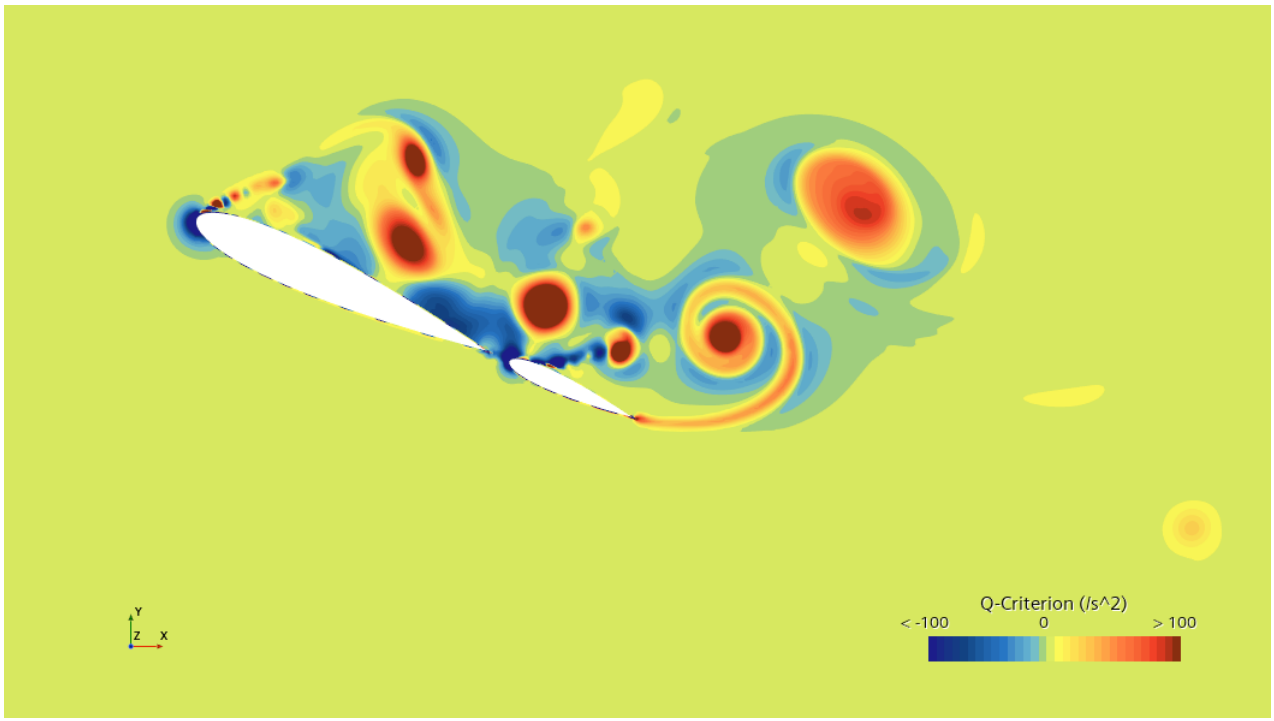

Figure 4.15: Q-Criterion at 114 000 iterations

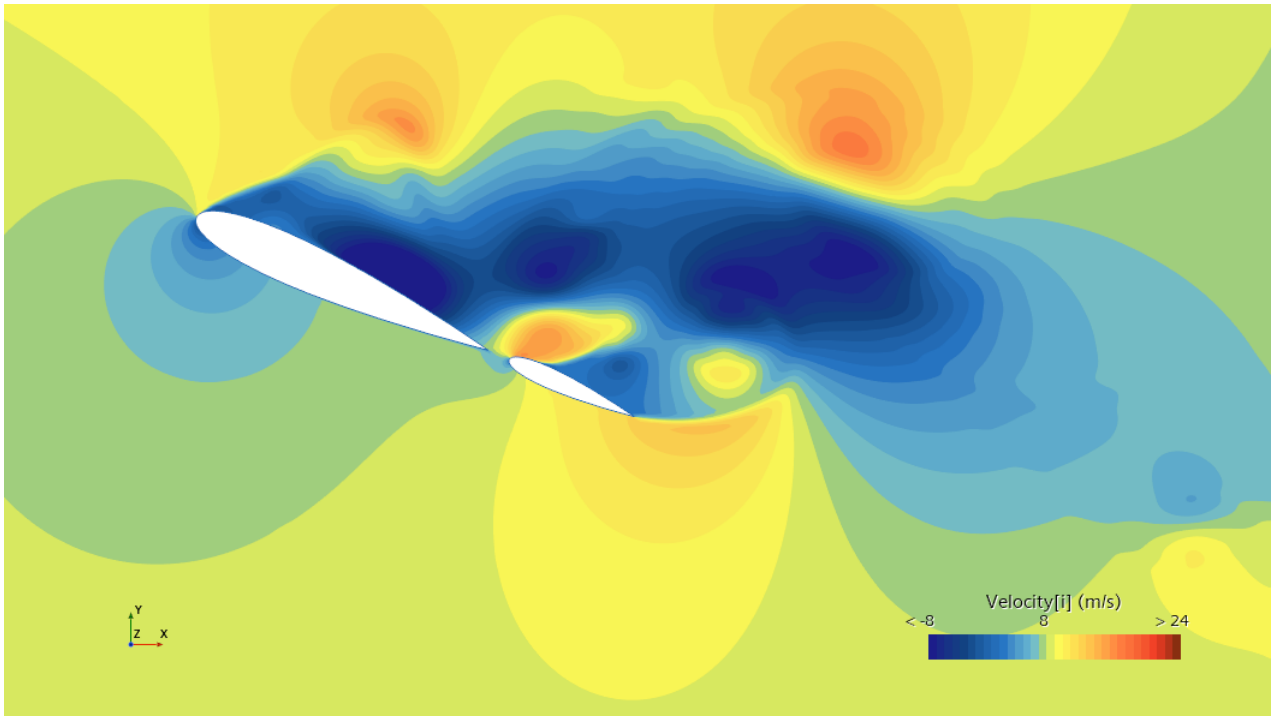

Figure 4.16: Velocity at 114 000 iterations

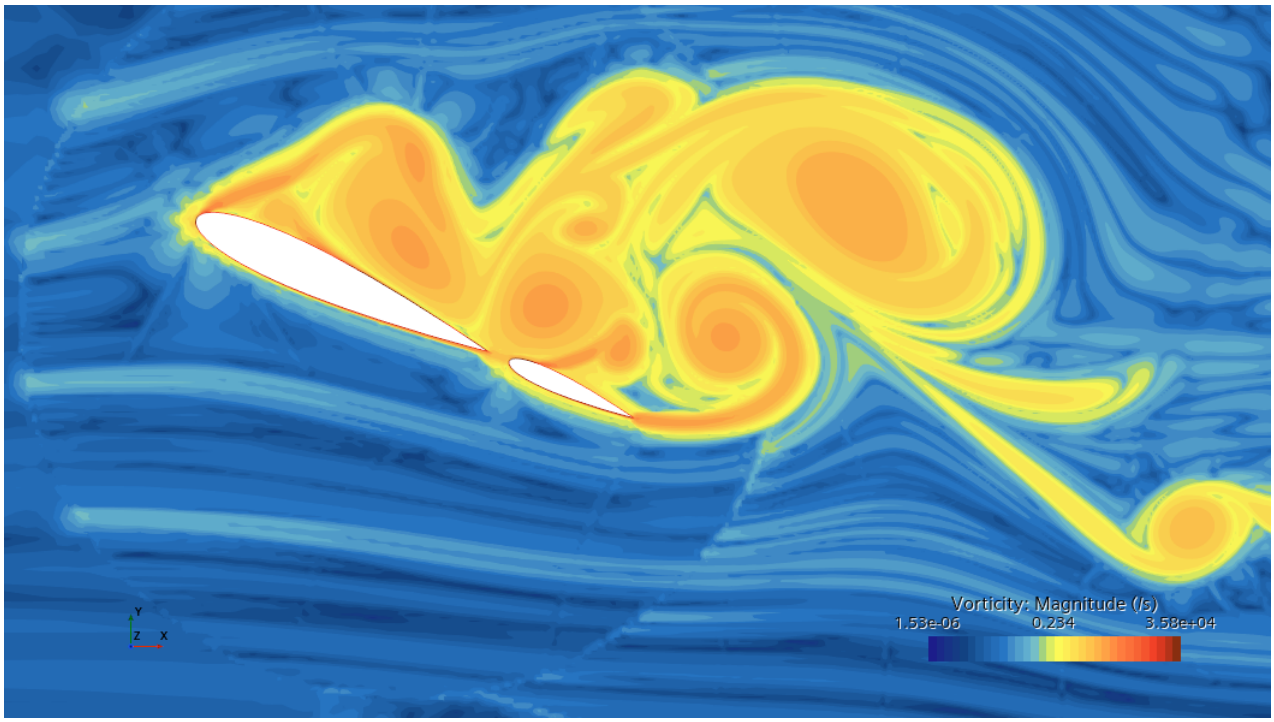

Figure 4.17: Vorticity at 114 000 iterations

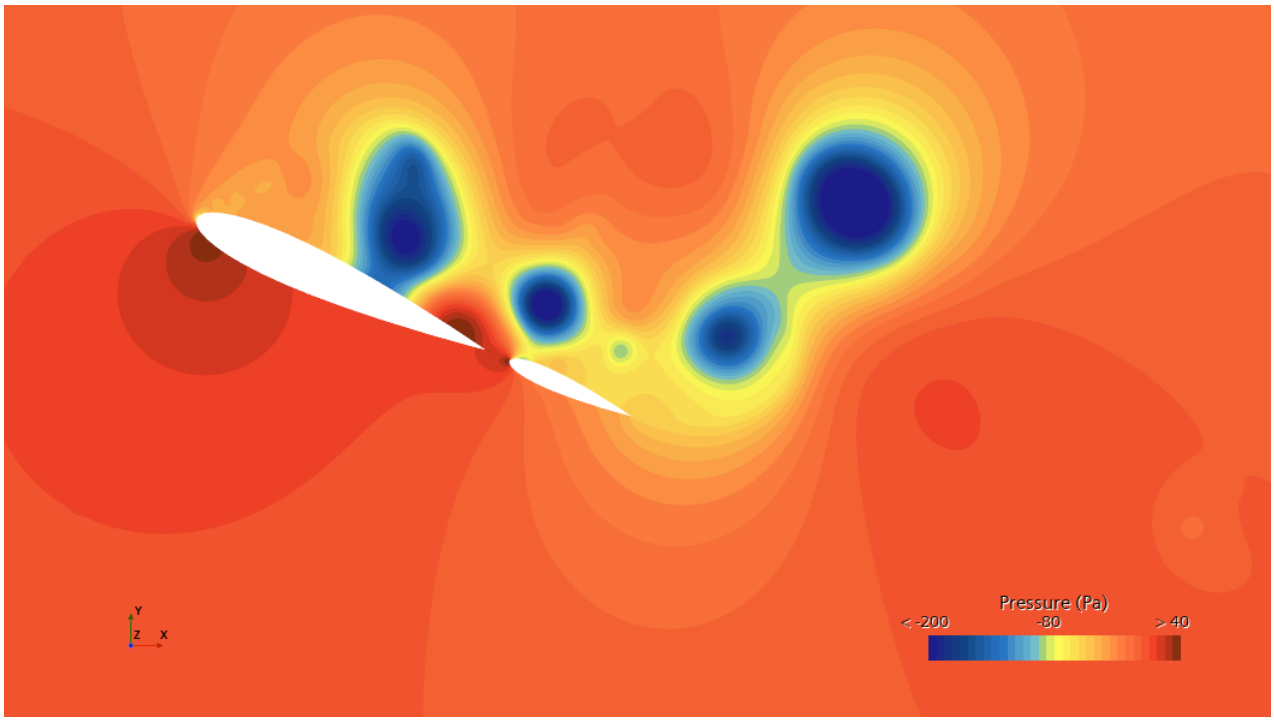

Figure 4.18: Pressure at 114 000 iterations

Similar to the previous case, when looking at the velocity plot in figure 4.16 the velocity decreases at the leading edge of the lower surface of the bigger foil, and then slowly increases as its moving downstream. At the tip of the trailing edge of

the front foil and the leading edge of the aft foil the velocity decreases again and is followed by another slow increase in velocity. When looking at the upper surface on the leading edge of the front foil there is a decrease in velocity almost immediately which consequently means an increase in pressure, which might cause the adverse pressure gradient to become great enough to create flow separation at the leading edge. This also seems to be the case when looking at the leading edge in figure 4.17. Furthermore, from the velocity plot a increase in velocity can be observed between the front and aft foils which suggest a low pressure region followed by presumably another great adverse pressure gradient region close to the leading edge of the aft foil, causing more flow separation. Going back to the vorticity plot this does seem to be the case as well. Looking at the pressure plot in figure 4.18 there is a low pressure region present at the leading edge of the aft foil, coinciding with the pocket of high velocity observed in the same spot. In the figure a region of high pressure can be observed at the upper surface of the trailing edge of the front foil, with lower pressure further up, suggesting that there might be flow separation in this region. Looking at the plot of the Q-values in figure 4.15 this is indeed the case as the flow is vorticity dominated in the low pressure region above the trailing edge. Additionally if the pressure and Q-Criterion plots are studied side by side it can be seen that the low pressure regions coincide with vorticity dominated flow.

4.2.1.3 Ratio 70/30 with 10% gap and no camber

Below the results for different AoA are presented for the setup of the two element foil sail with a chord length ratio of 70 and 30 for the front and aft foil respectively. In the setup of the simulations the distance between the aft of the bigger foil and the front of the smaller foil was set to be 1.4m, or 10% of the total length of the wings.

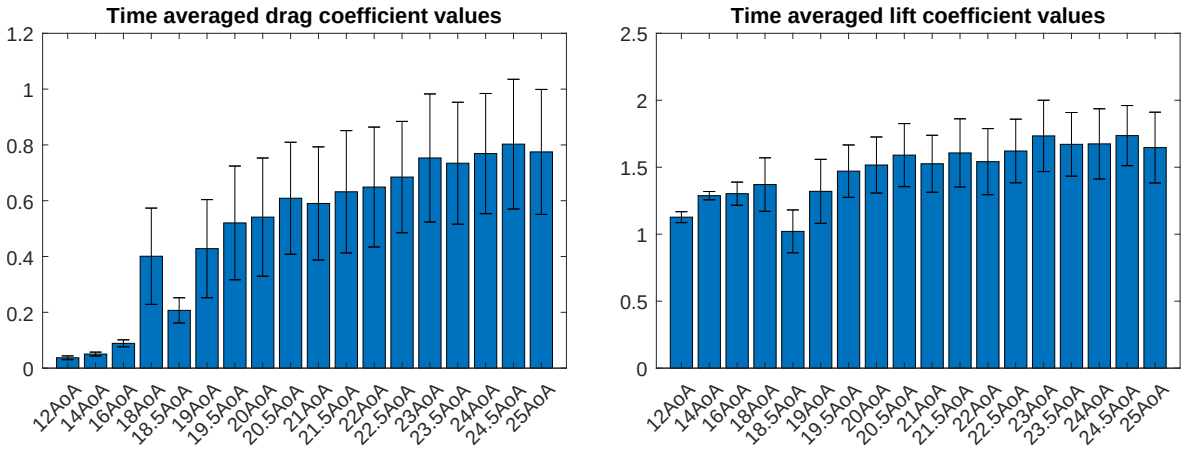

(a) Drag force coefficients

(b) Lift force coefficients

Figure 4.19: Time averaged force coefficient values

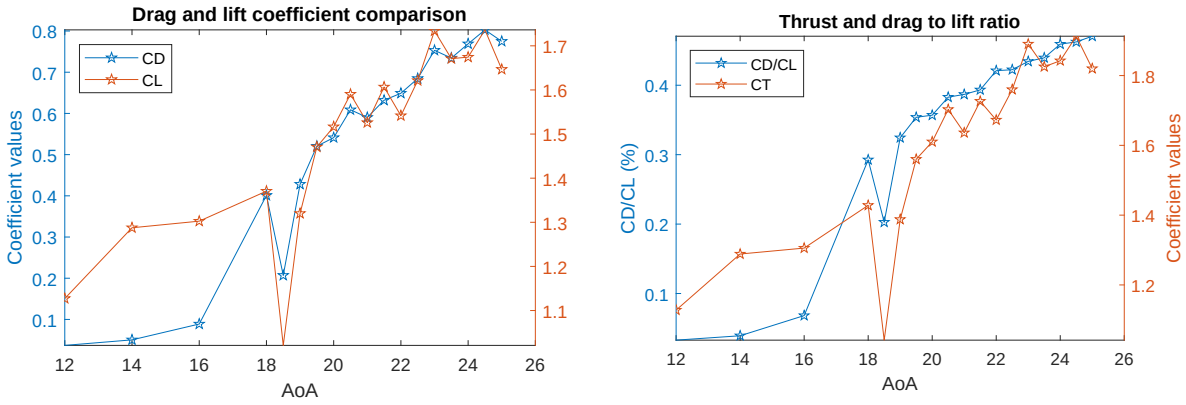

(a) Comparison of coefficients

(b) Thrust and size relation between coefficients

Figure 4.20: Time averaged force coefficient values

Just as for the other two setups with different gap distances it seems like, looking at figure 4.19, the drag coefficients oscillate more than the lift. Also by looking at figures 4.19 (b) and 4.20 (a) a significant drop in lift can be observed when exceeding 18°AoA, but the maximum lift is achieved at 24.5°AoA suggesting that stall occurs at this angle. Interestingly the onset of the range of stall is further delayed in this instance, beginning at 18°AoA and ending at 24.5°AoA. From the results of the three different designs for this two element foil rigid wingsail it does seem like altering the gap distance between the front and aft foil slightly changes the onset of stall behavior in the sail.

The following table presents the AoA where the greatest thrust coefficient values were achieved

AoA	24.5AoA	23AoA	24AoA
C_T	1.9128	1.8904	1.8425

Table 4.4: The three greatest thrust coefficient values in descending order and the respective AoA

4.2.1.3.1 24.5AoA Here is a more in-depth look at the AoA which yielded the greatest maximum potential thrust.

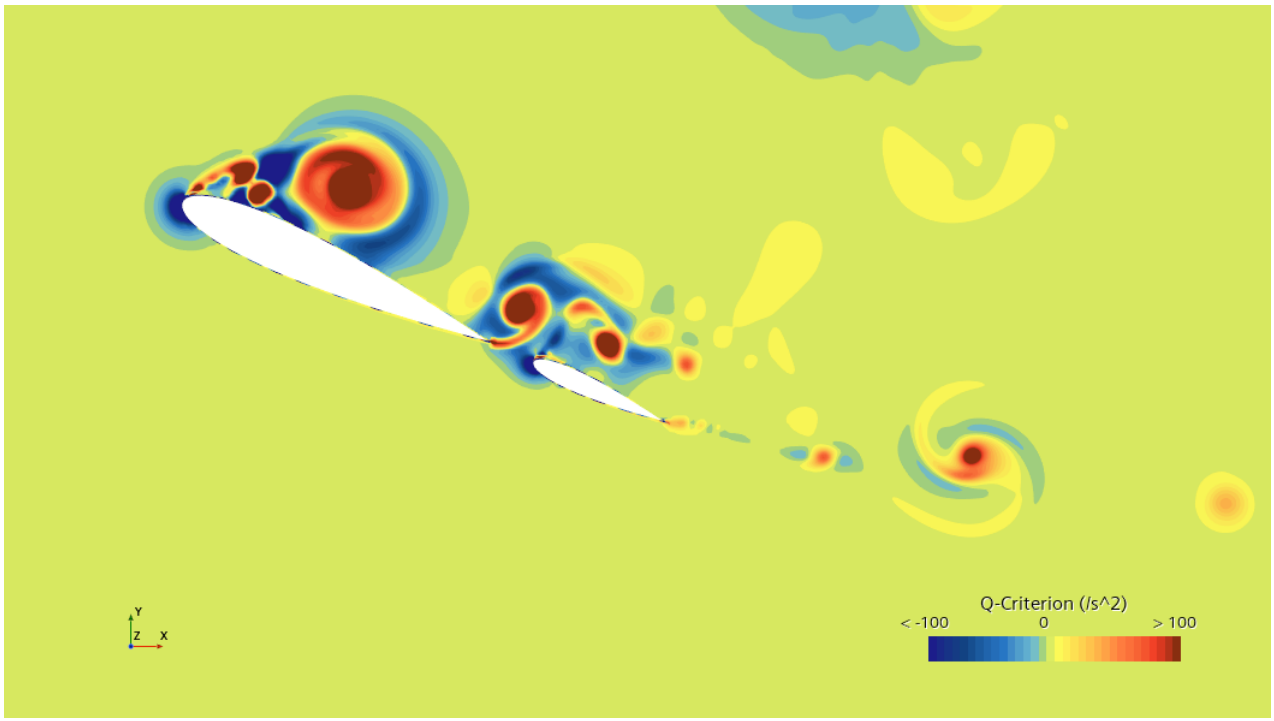

Figure 4.21: Q-Criterion at 72 000 iterations

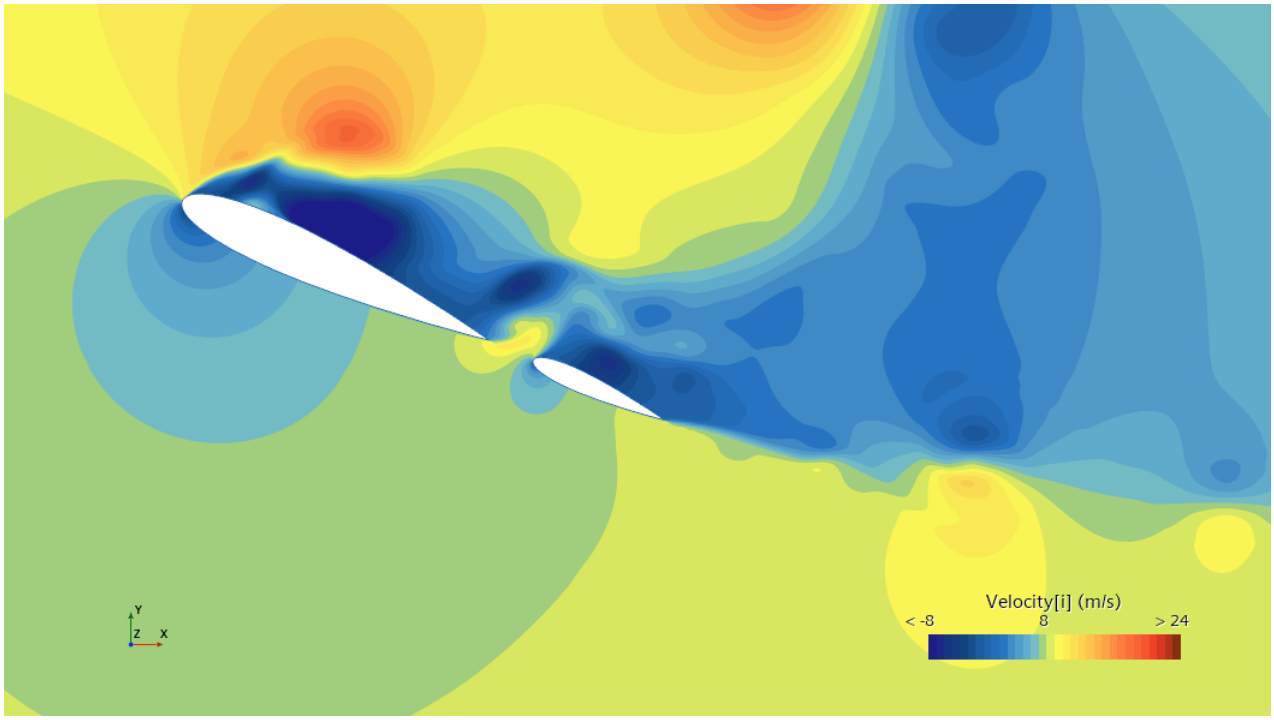

Figure 4.22: Velocity at 72 000 iterations

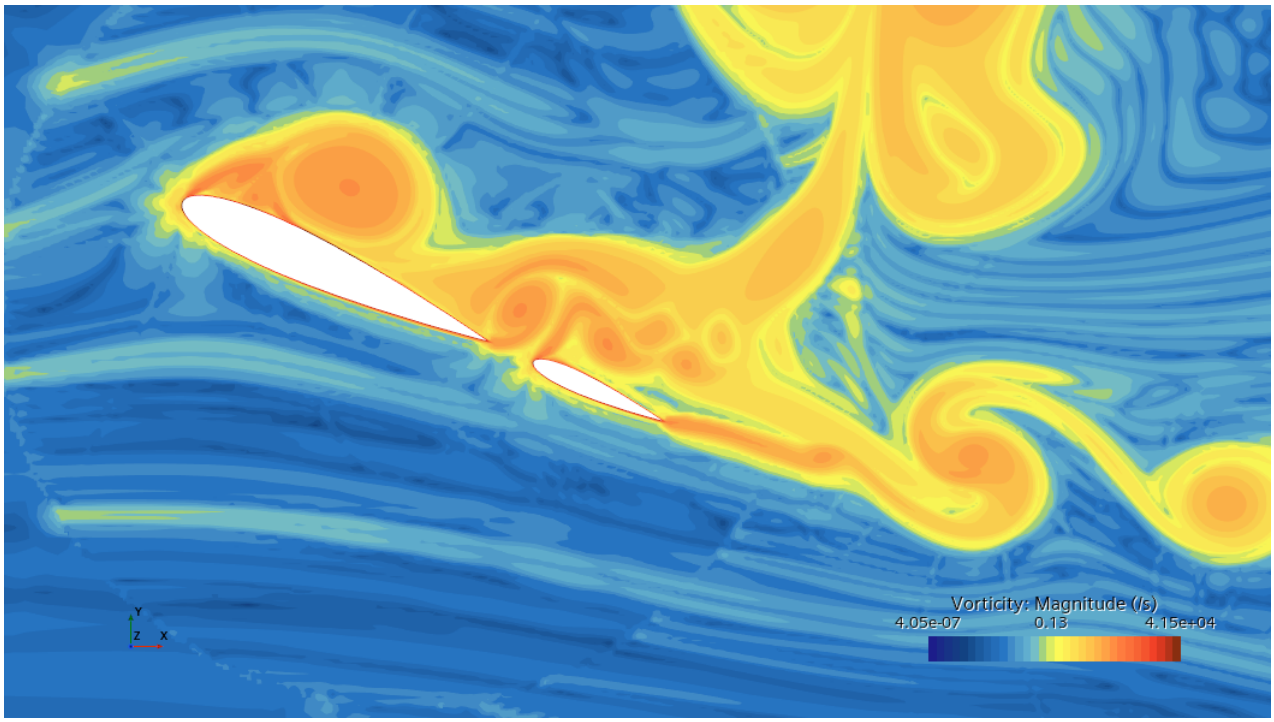

Figure 4.23: Vorticity at 72 000 iterations

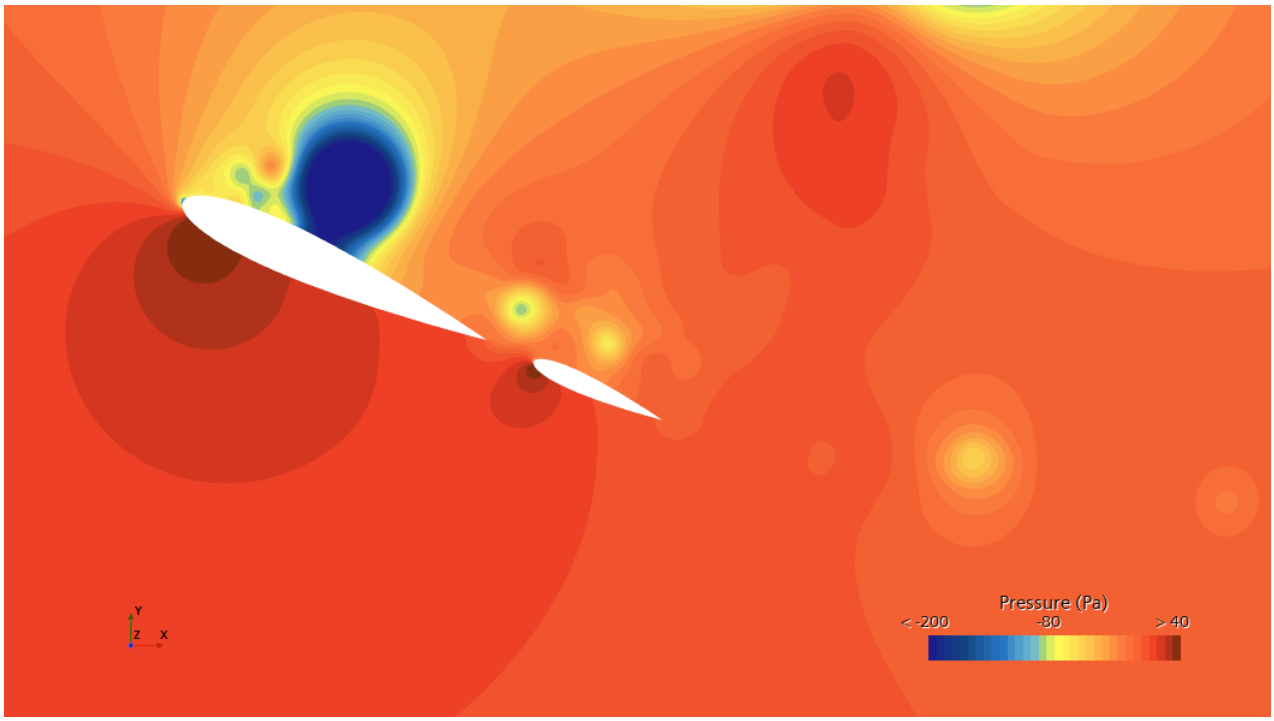

Figure 4.24: Pressure at 72 000 iterations

As has been observed before and is expected, the velocity in figure 4.22 decreases at the leading edge of the front foils lower surface and then slowly increases as it moves downstream, which should create a region of higher pressure at the lower

surface close to the leading edge. Looking at the leading edge of the front foil on the upper surface a more defined decrease in velocity can be detected, which once again suggests there might be flow separation due to large adverse pressure gradients. A slight increase in velocity can be seen close to the leading edge followed by a significant decrease in velocity, which suggests very high adverse pressure gradient on this part of the upper surface, which in turn leads to lots of turbulence and consequently low pressure. If the pressure plot in figure 4.24 is studied there is indeed quite low pressure in this low-velocity region on the foil. The vorticity plot in figure 4.23 confirms that there is some flow separation at the leading edge of the front wing as well as vorticity in the low-velocity region. This is also confirmed by the Q-Criterion plot in figure 4.21 which displayes vorticity dominated flow at the leading edge and the low-velocity region. Going back to the velocity plot the speed increases at the trailing edge of the front foil and, just as for the front foil, appears to decrease more rapidly at the upper surface of the leading edge than the lower. However comparing the vorticity plot with the Q-Criterion plot it seems like the flow at the upper surface of the aft wing is mostly strain-dominated rather than vorticity dominated.

4.2.1.4 Ratio 80/20 with no gap and no camber

Below the results for different AoA are presented for the setup of the two element foil sail with a chord length ratio of 80 and 20 for the front and aft foil respectively. In the setup of the simulations the distance between the aft of the bigger foil and the front of the smaller foil was set to be zero.

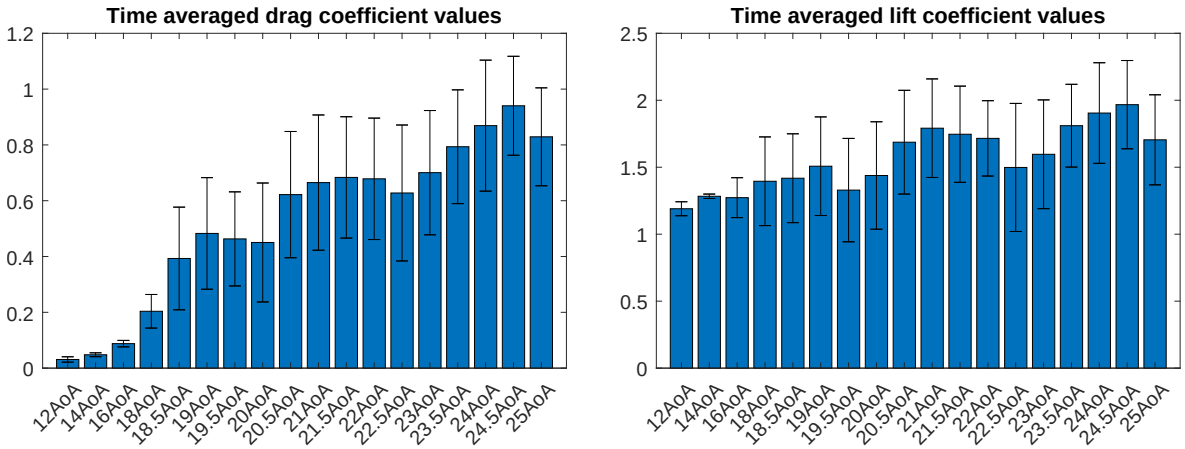

(a) Drag force coefficients **(b)** Lift force coefficients

Figure 4.25: Time averaged force coefficient values

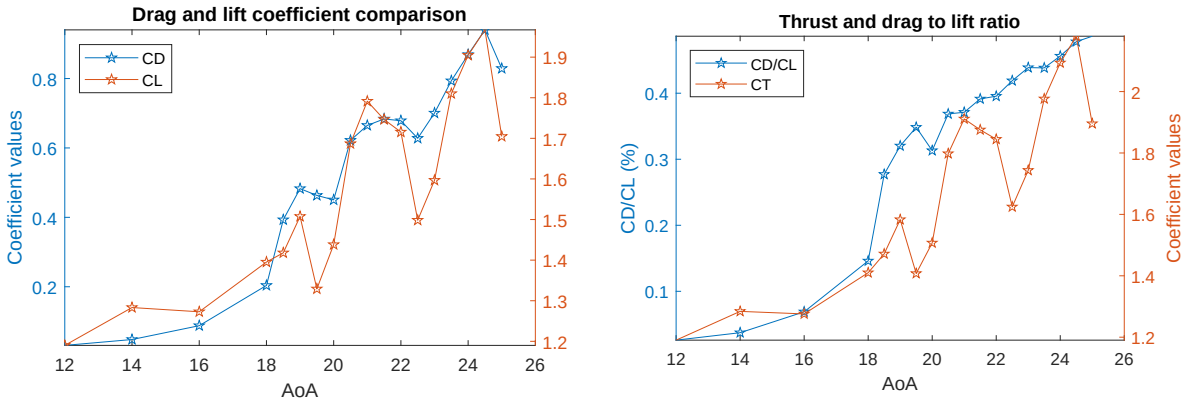

(a) Comparison of coefficients

(b) Thrust and size relation between coefficients

Figure 4.26: Time averaged force coefficient values

Inspecting figures 4.25 (b) and 4.26 (a) it can be seen that the maximum lift is achieved at an AoA of 24.5°followed by a steep decline in lift when the AoA exceeds this value, suggesting that 24.5 is the critical AoA for this sail configuration. The range of stall for this wingsail ranges from 14 to 24.5°AoA, which can be compared to the wingsail with no gap and ratio 70/30 whose range of stall began at 12°AoA.

The following table presents the AoA where the greatest thrust coefficient values were achieved

AoA	24.5AoA	24AoA	23.5AoA
C_T	2.1803	2.0935	1.9764

Table 4.5: The three greatest thrust coefficient values in descending order and the respective AoA

4.2.1.4.1 24.5AoA Here is a more in-depth look at the AoA which yielded the greatest maximum potential thrust.

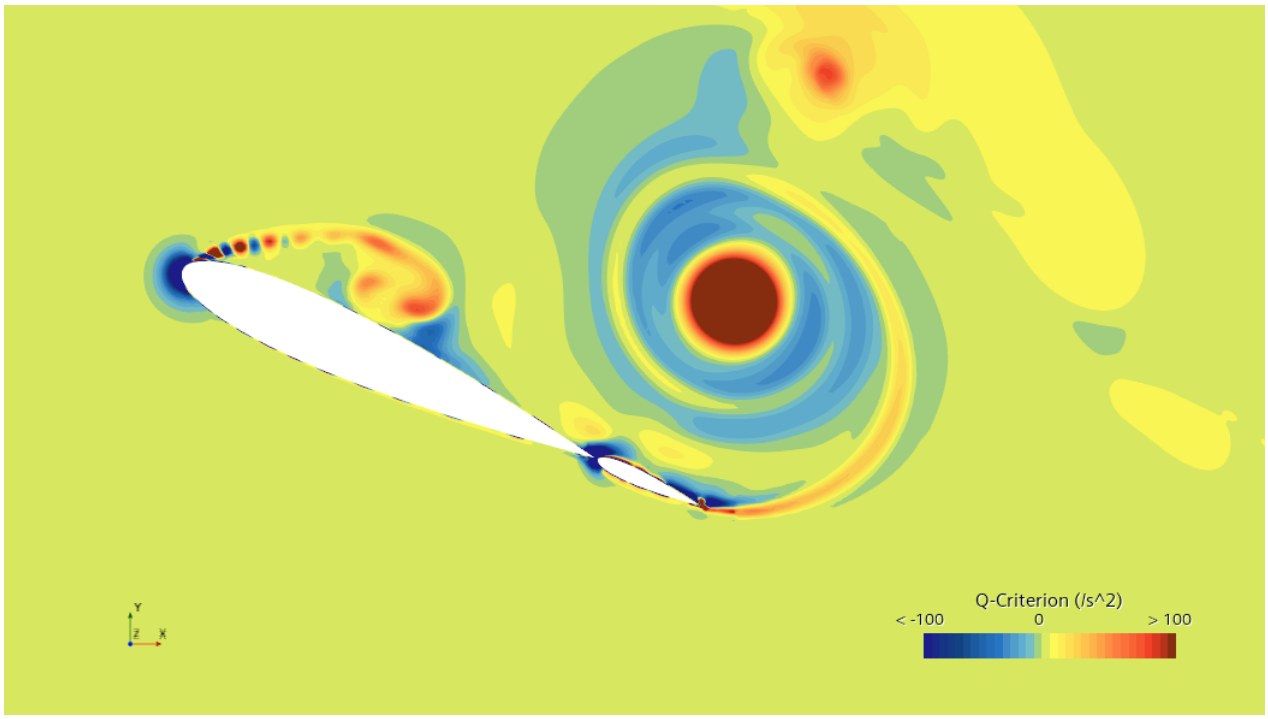

Figure 4.27: Q-Criterion at 120 000 iterations

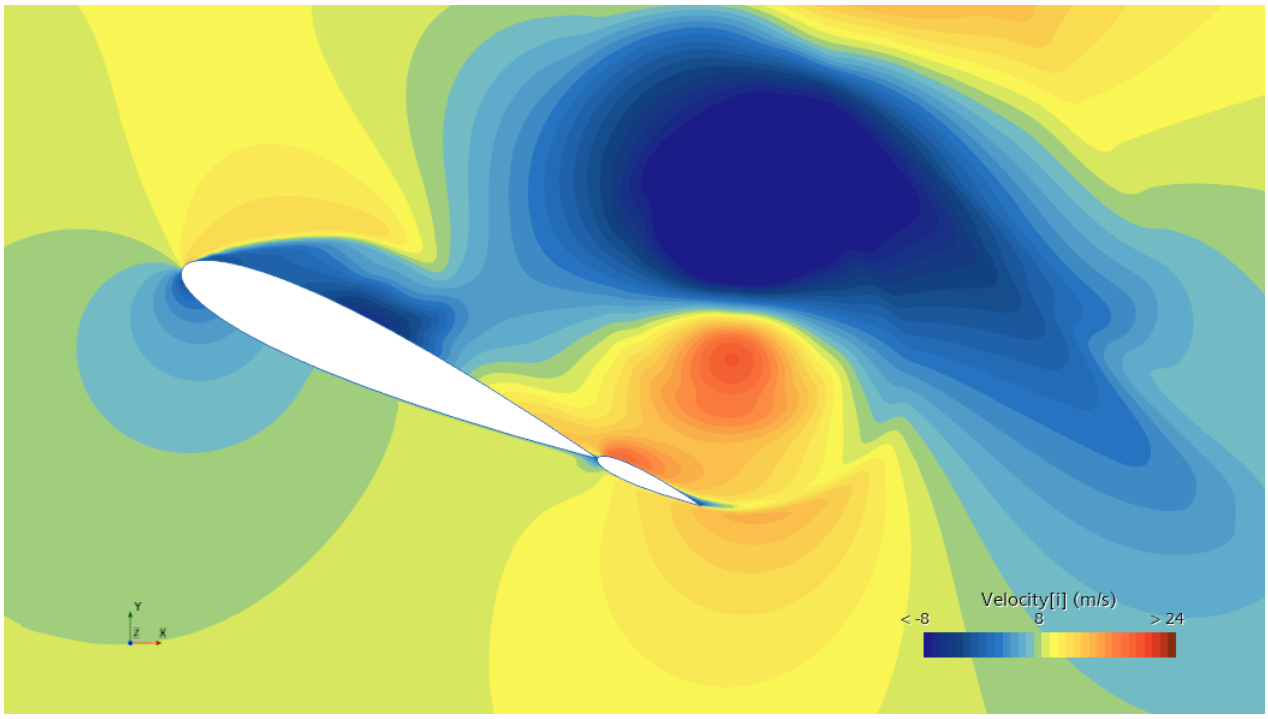

Figure 4.28: Velocity at 120 000 iterations

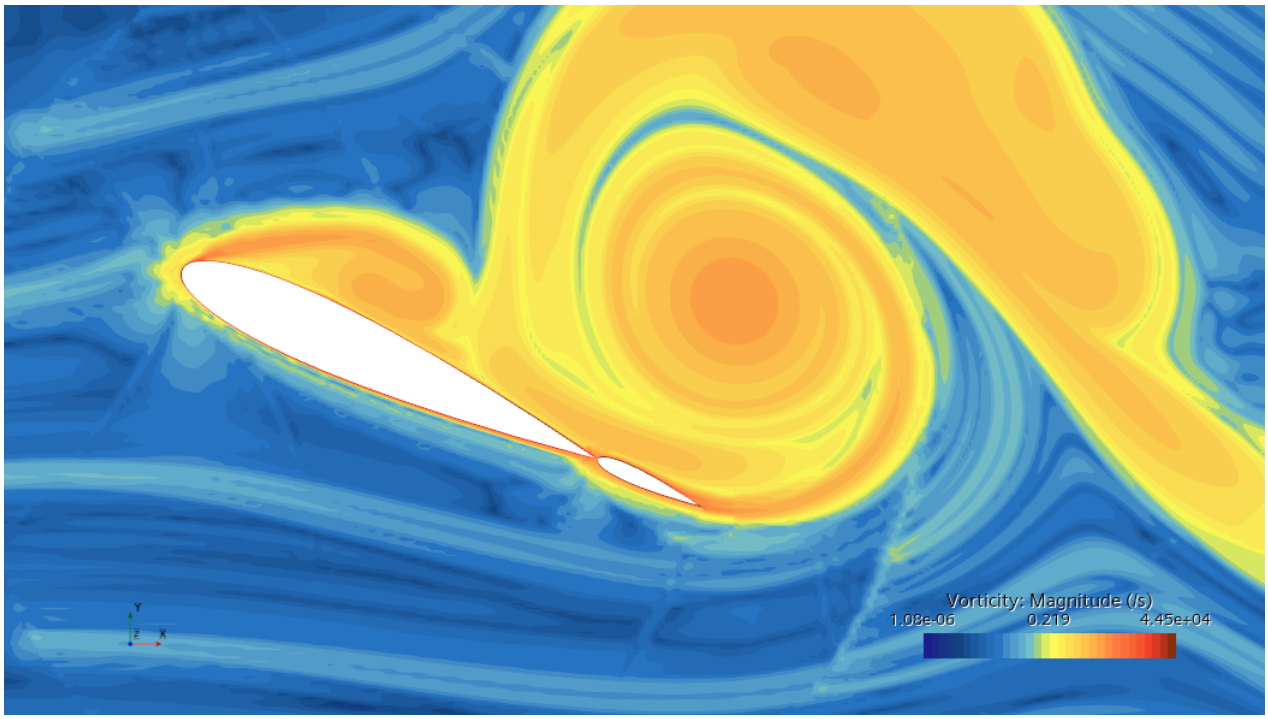

Figure 4.29: Vorticity at 120 000 iterations

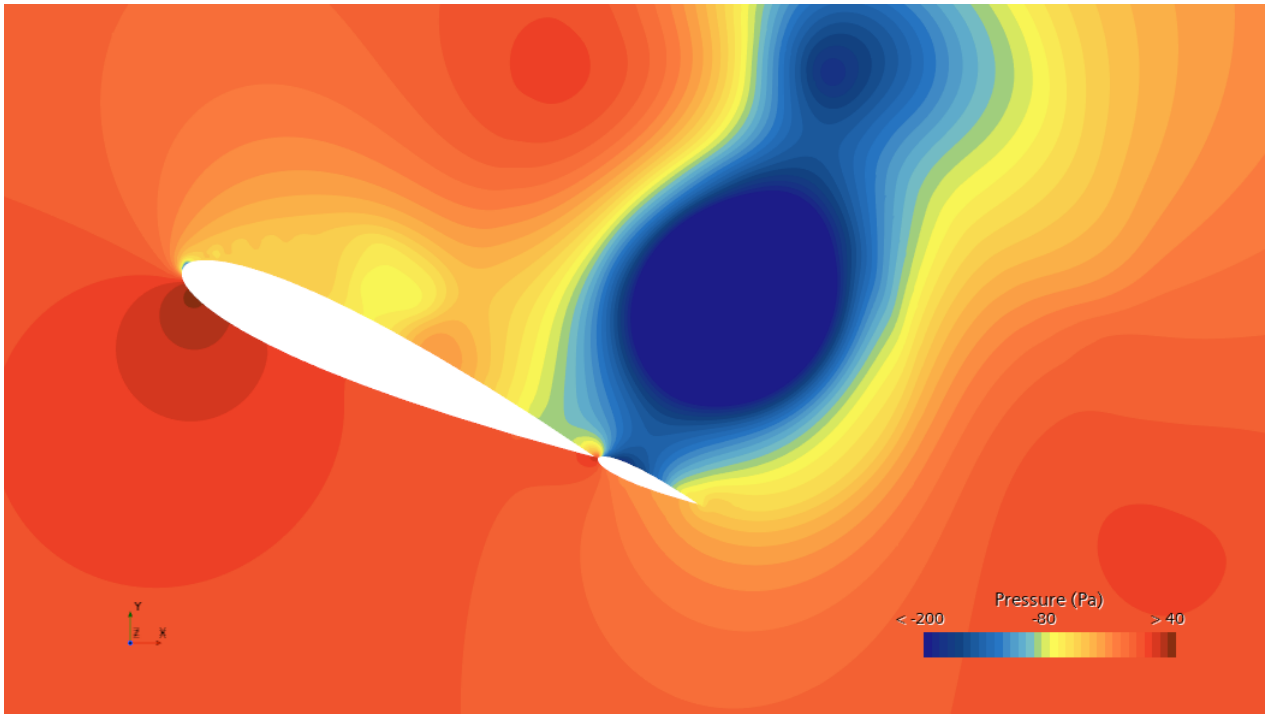

Figure 4.30: Pressure at 120 000 iterations

The velocity plot in figure 4.28 displays similar behaviour to what has been observed previously, with a velocity decrease at the leading edges upper and lower surfaces of the front foil, with a seemingly stronger decrease at the upper surface, suggesting

some flow separation. The increase in velocity closer to the trailing edge of the front foil and the leading edge of the aft foil also suggest a large low pressure region, followed by a decrease in velocity at the trailing edge of the aft foil, which could cause flow separation due to a big adverse pressure gradient. Looking at the pressure plot 4.30 the high velocity region coincides with the presence of low pressure. The vorticity 4.29 and Q-Criterion 4.27 plots show that there is some separation at the leading edge of the front foil, but not so much at the trailing edge of the aft foil. However these plots also show the presence of a large vortex above the upper surface of the aft foil.

4.2.1.5 Ratio 80/20 with 5% gap and no camber

Below the results for different AoA are presented for the setup of the two element foil sail with a chord length ratio of 80 and 20 for the front and aft foil respectively. In the setup of the simulations the distance between the aft of the bigger foil and the front of the smaller foil was set to be 0.7m, or 5% of the total length of the wings.

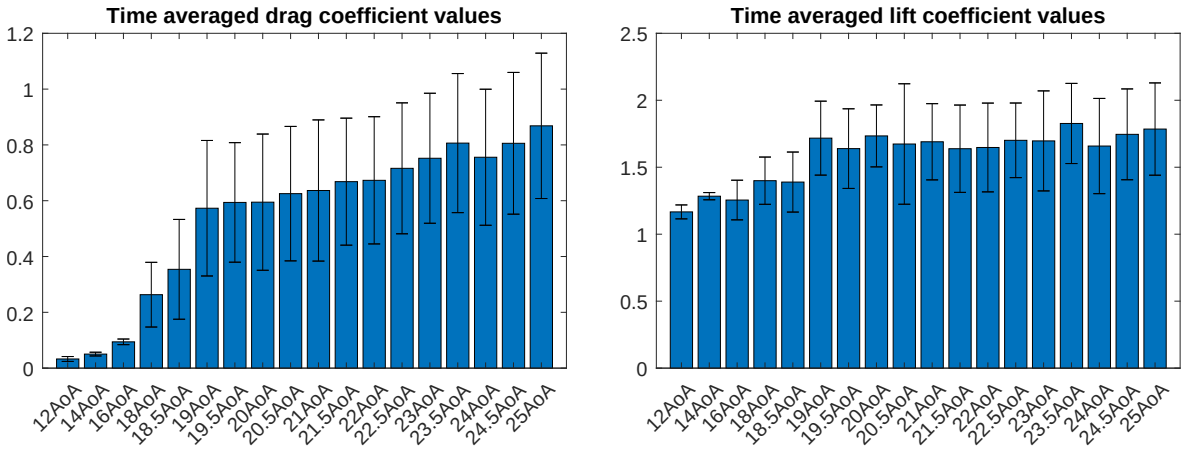

(a) Drag force coefficients **(b)** Lift force coefficients

Figure 4.31: Time averaged force coefficient values

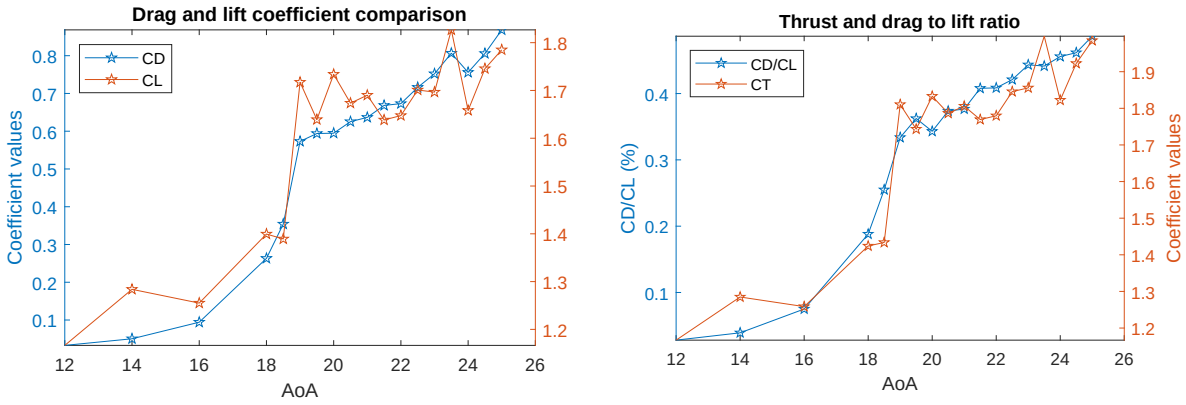

(a) Comparison of coefficients

(b) Thrust and size relation between coefficients

Figure 4.32: Time averaged force coefficient values

Inspecting figures 4.31 (b) and 4.32 (a) the highest lift is achieved at 23.5°AoA with a decrease in lift, but then some recovery, as seen in both the bar plot and in table 4.6. It is hard to say if a greater lift would be achieved at AoA higher than 25°, but since the lift first decreases after the observed maximum, and then increases rather than decreases as the AoA is increased, it is not impossible that stall occurs at an AoA not included in this study. However for this study, with the data available, it will be assumed that the stall angle is 23.5°AoA. The range of stall begins at the same AoA for this wingsail as for the previous one without any gap, that is at 14°AoA, and ends at 23.5°AoA.

The following table presents the AoA where the greatest thrust coefficient values were achieved

AoA	23.5AoA	25AoA	24.5AoA
C_T	1.9969	1.9850	1.9226

Table 4.6: The three greatest thrust coefficient values in descending order and the respective AoA

4.2.1.5.1 23.5AoA Here is a more in-depth look at the AoA which yielded the greatest maximum potential thrust.

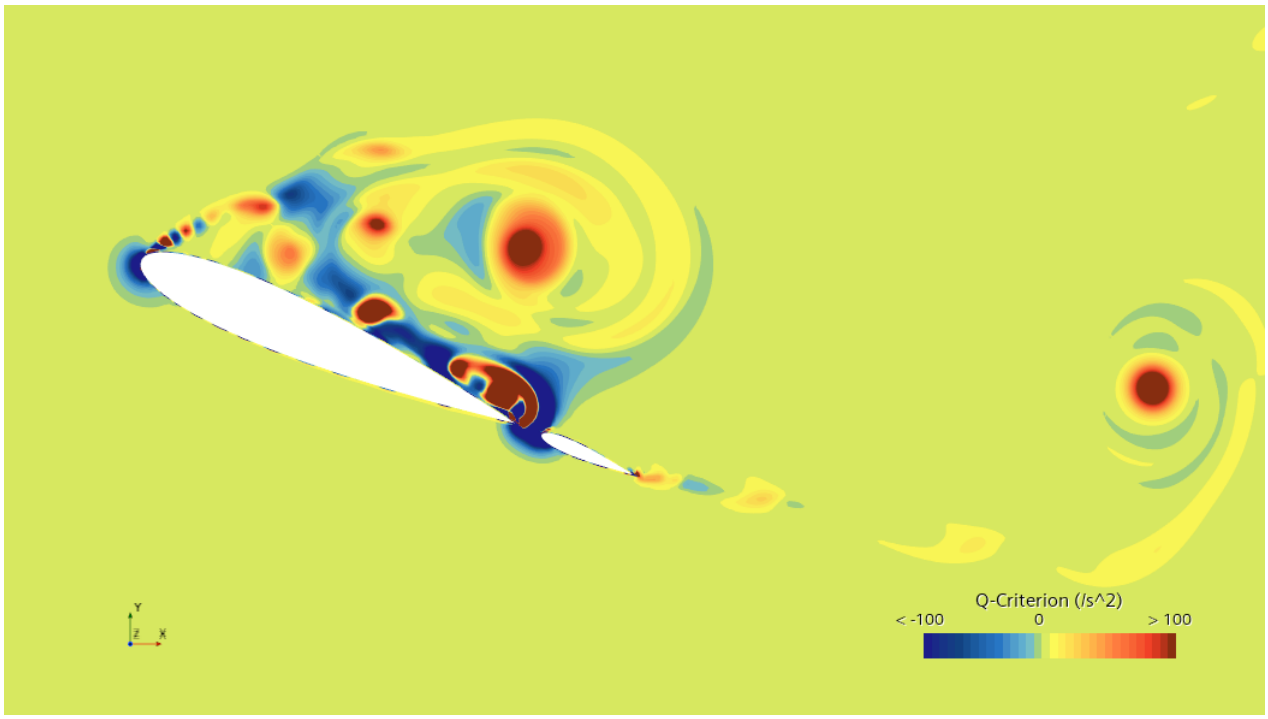

Figure 4.33: Q-Criterion at 120 000 iterations

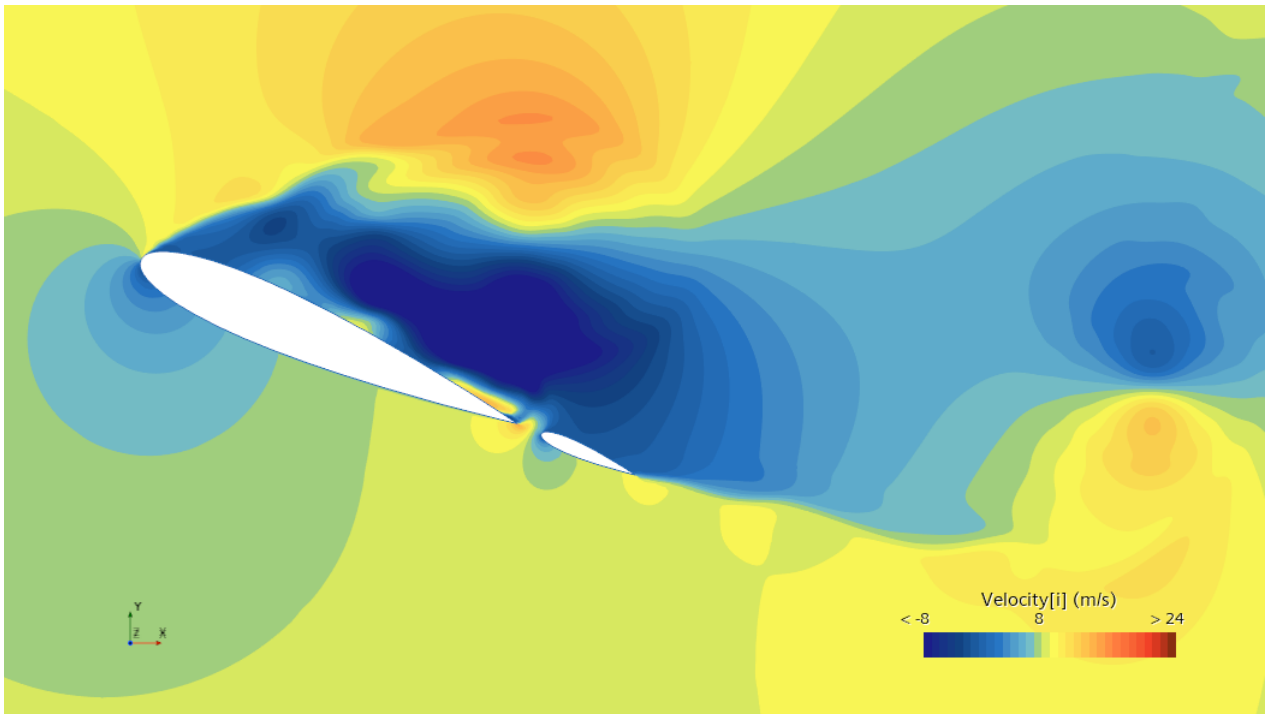

Figure 4.34: Velocity at 120 000 iterations

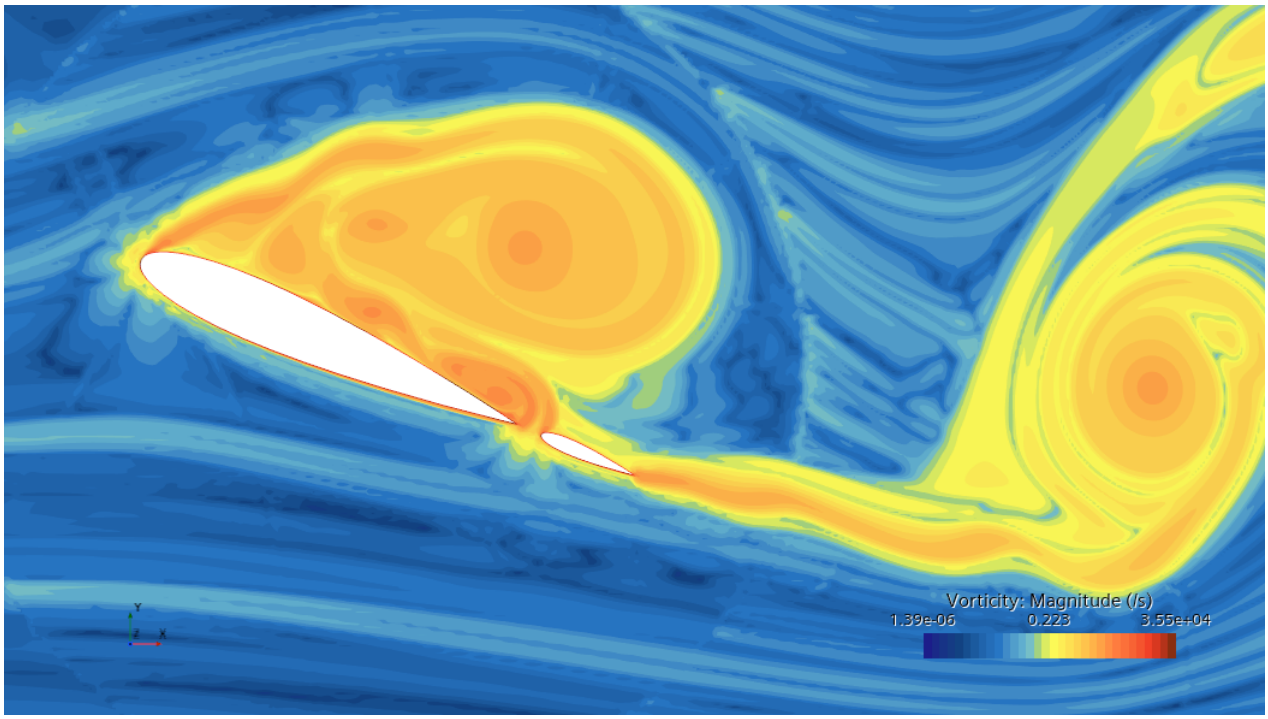

Figure 4.35: Vorticity at 120 000 iterations

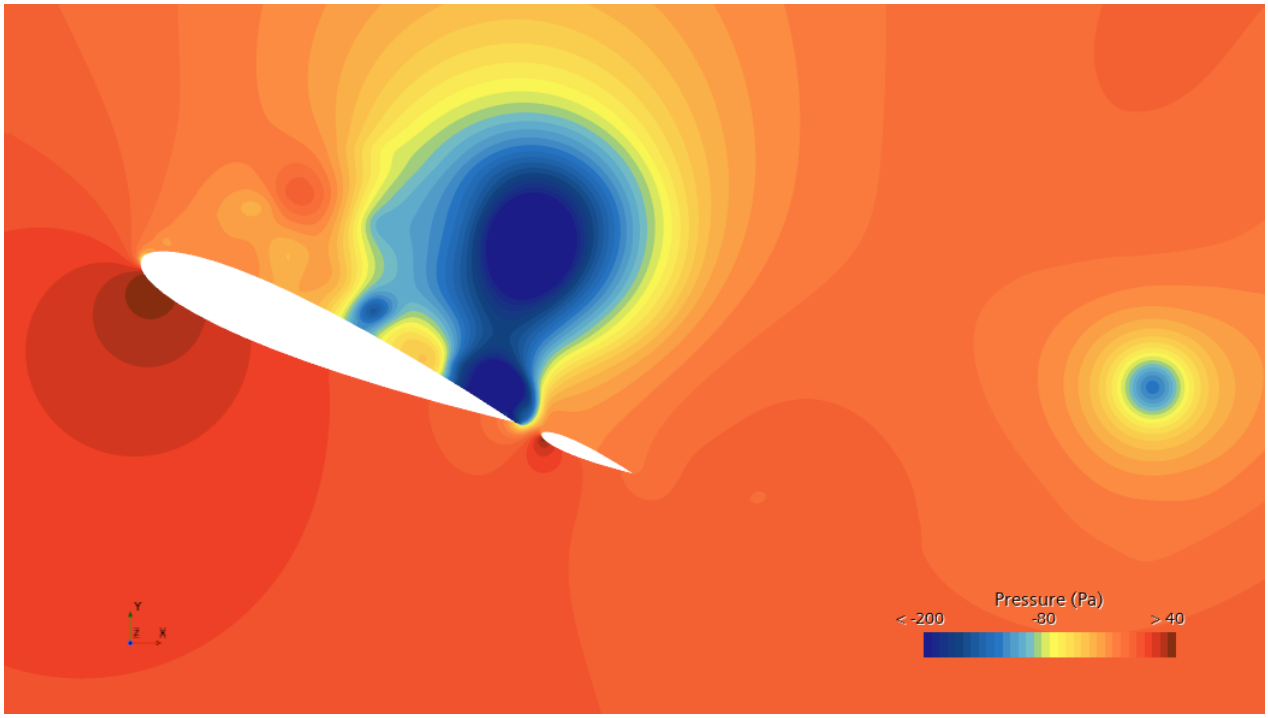

Figure 4.36: Pressure at 120 000 iterations

Interestingly in the velocity plot in figure 4.34 there are two two small regions along the upper surface of the front wing where the velocity increases and then decreases which suggest some local low pressure spots surrounded by higher pressure, thus

there might be some flow separation happening here. The pressure plot in figure 4.36 confirms this and looking at the vorticity and Q-Criterion plots in figures 4.35 and 4.33 respectively it can be seen that there is vorticity dominated flow here.

4.2.1.6 Ratio 80/20 with 10% gap and no camber

Below the results for different AoA are presented for the setup of the two element foil sail with a chord length ratio of 80 and 20 for the front and aft foil respectively. In the setup of the simulations the distance between the aft of the bigger foil and the front of the smaller foil was set to be 1.4m, or 10% of the total length of the wings.

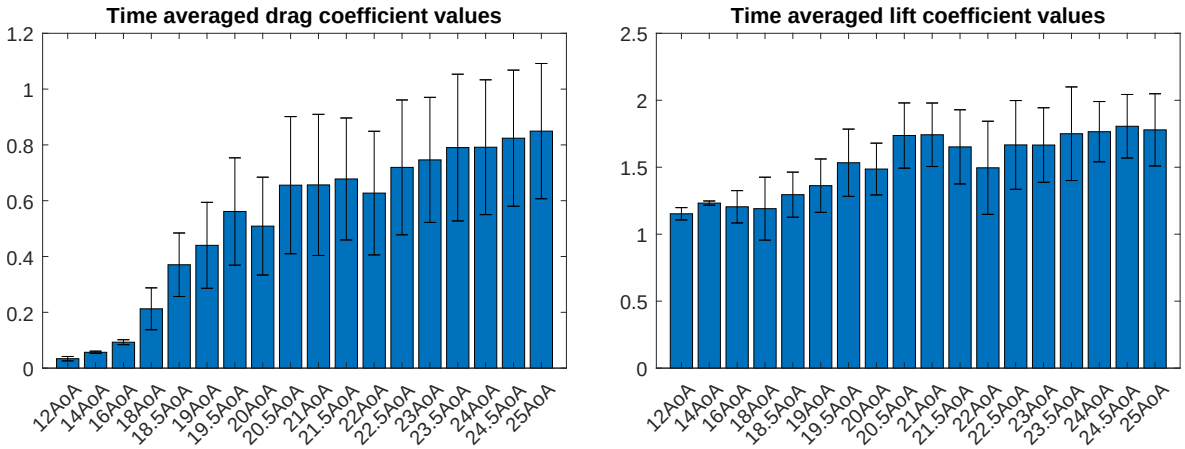

(a) Drag force coefficients

(b) Lift force coefficients

Figure 4.37: Time averaged force coefficient values

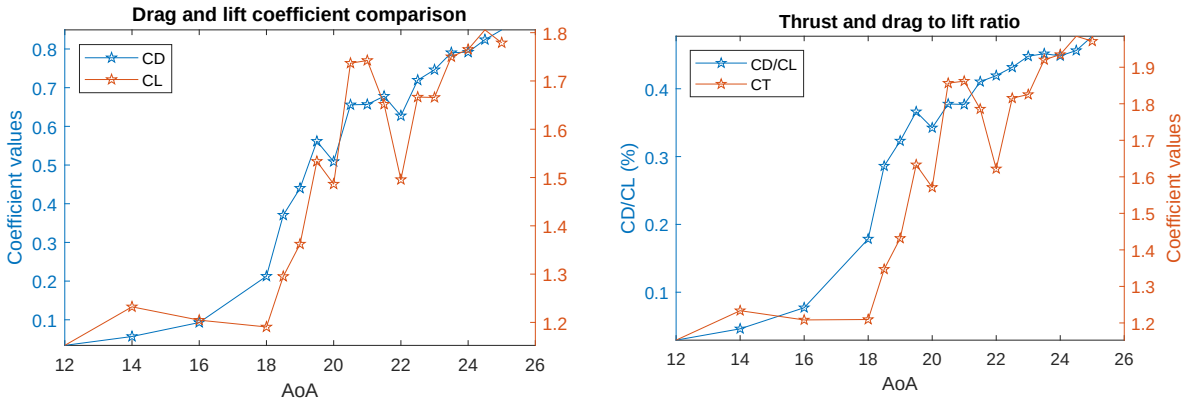

(a) Comparison of coefficients

(b) Thrust and size relation between coefficients

Figure 4.38: Time averaged force coefficient values

By looking at the bar plot in figure 4.37 (b) and the line plot in figure 4.38 (a) the greatest lift is achieved at 24.5 AoA. This is presumably the stall angle for this configuration of the sail as the lift decreases as the AoA increases beyond this point, as shown in table 4.7 and figure 4.37 (b). It is also interesting to note the significant loss of lift that occurs when passing 21 AoA which then recovers after 22.5 AoA. The onset of the range of stall remains unchanged with the changing of the gap distances, in contrast to the wingsail with ratio 70/30, and for this case ends at 24.5°AoA.

The following table presents the AoA where the greatest thrust coefficient values were achieved

AoA	24.5AoA	25AoA	24AoA
C_T	1.9849	1.9713	1.9347

Table 4.7: The three greatest thrust coefficient values in descending order and the respective AoA

4.2.1.6.1 24.5AoA Here is a more in-depth look at the AoA which yielded the greatest maximum potential thrust.

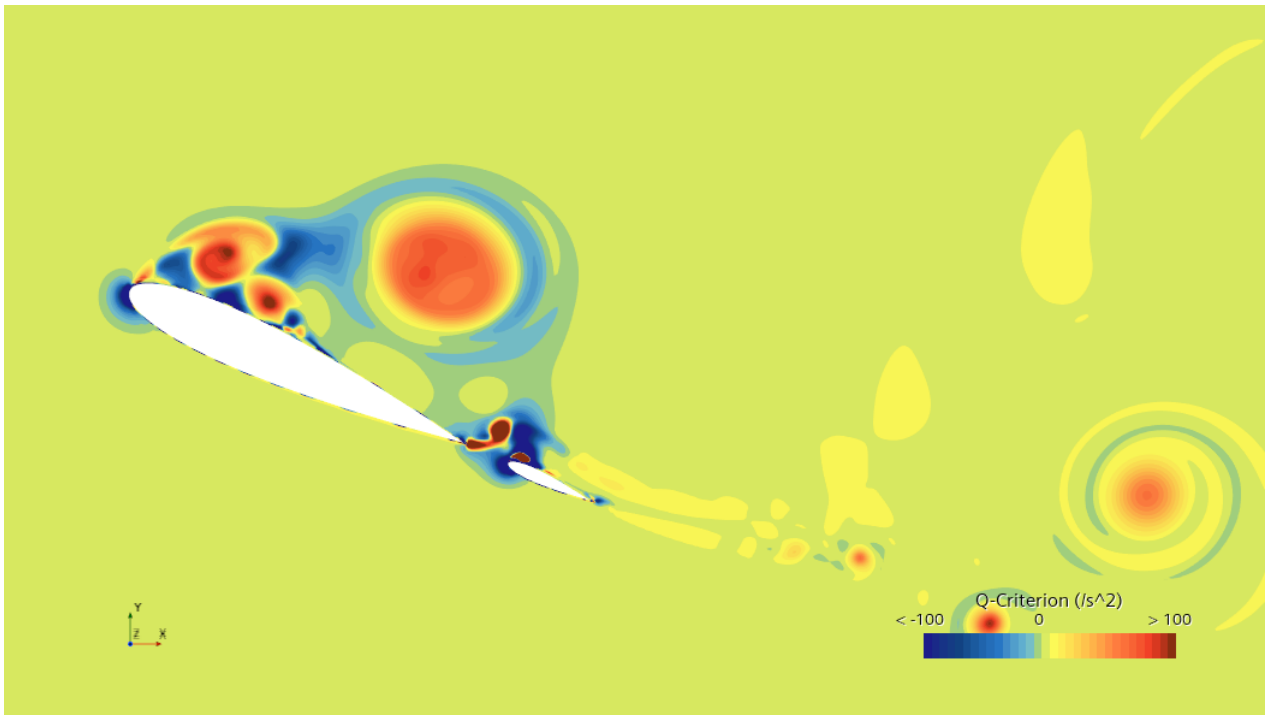

Figure 4.39: Q-Criterion at 120 000 iterations

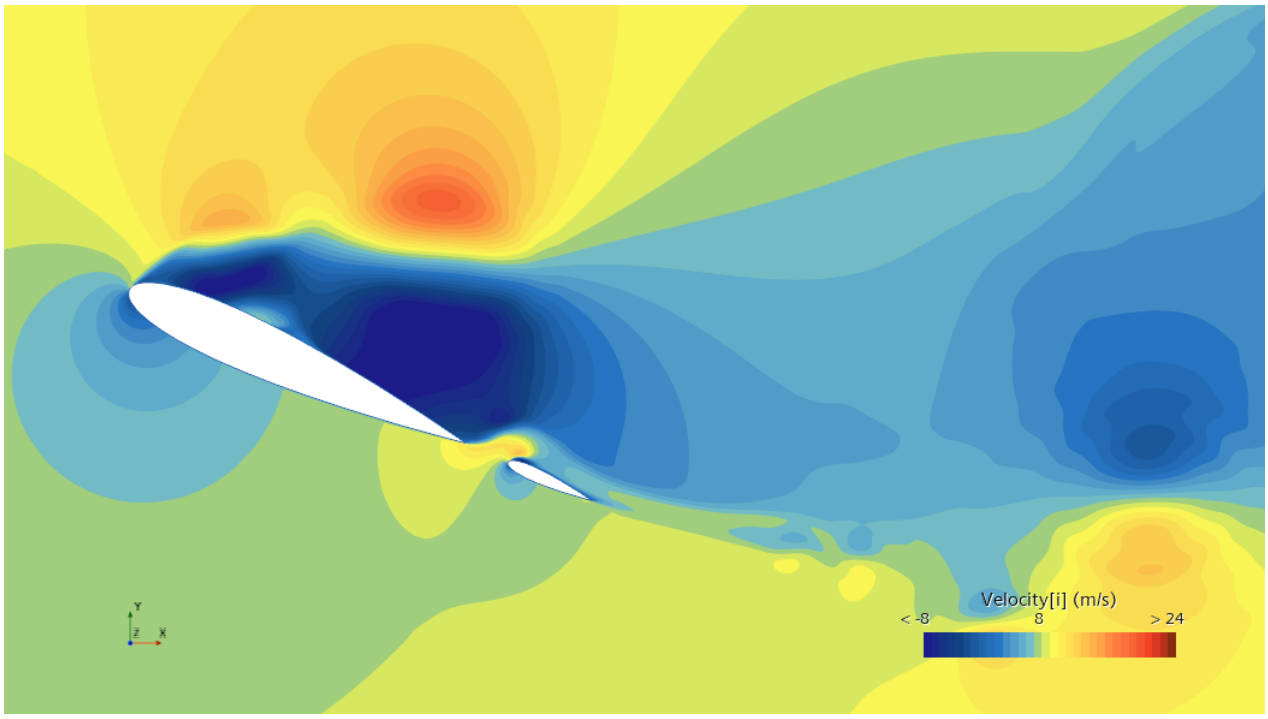

Figure 4.40: Velocity at 120 000 iterations

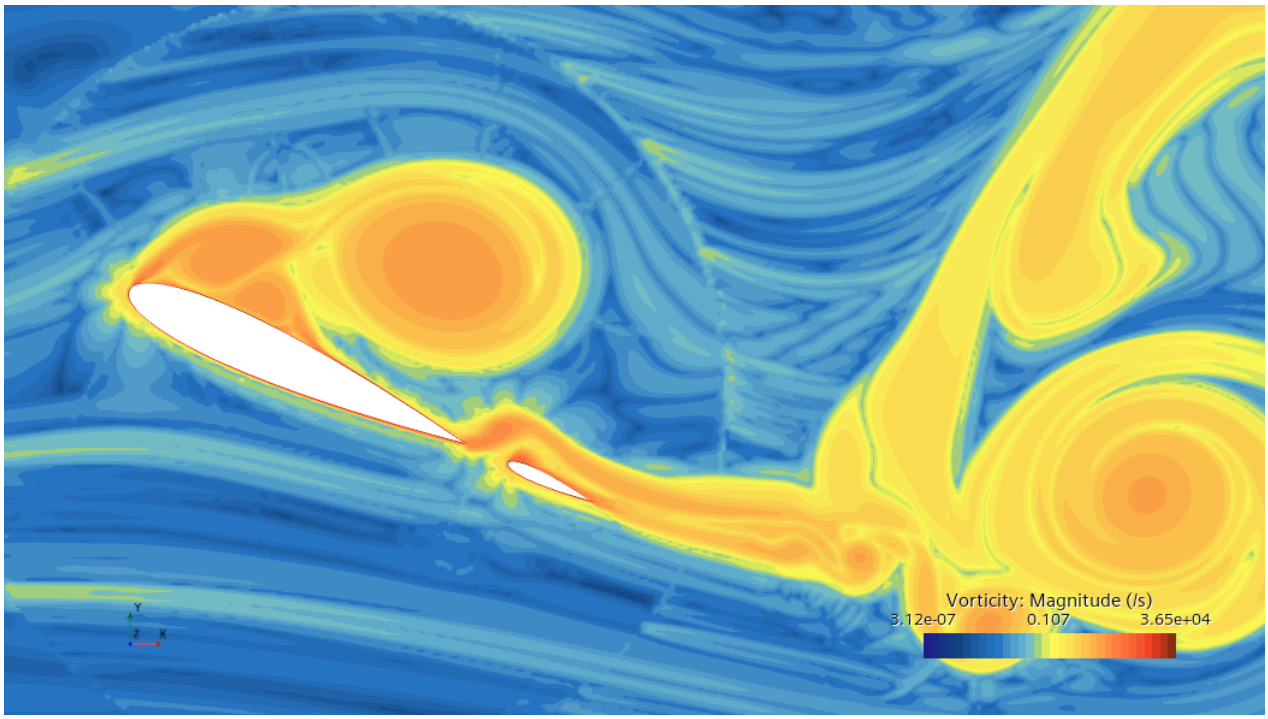

Figure 4.41: Vorticity at 120 000 iterations

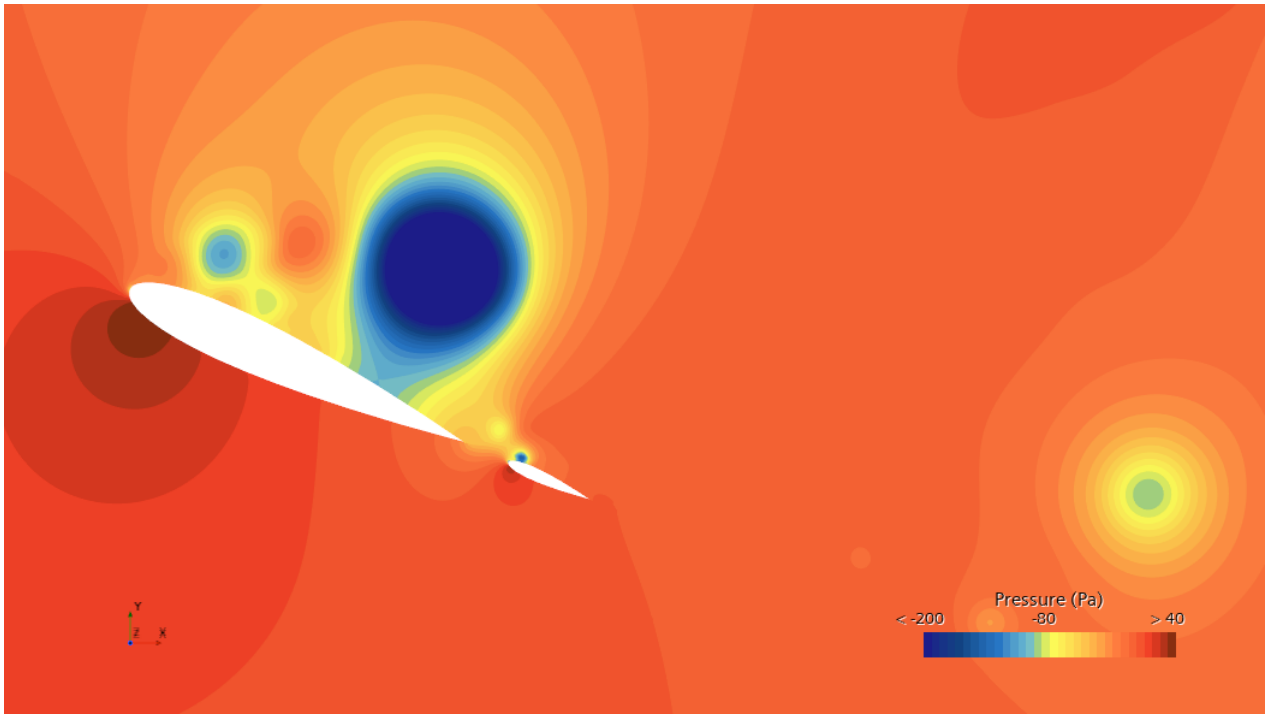

Figure 4.42: Pressure at 120 000 iterations

As seems common by now the velocity at the upper surface of the trailing edge of the front wing decreases a lot quite quickly compared to the lower surface, as seen in figure 4.40, which might cause some flow separation. The flow then increases a

small distance downstream along the foil and then decreases to very low velocities, which could add upon the suspected flow separation at the leading edge. At the aft foil the velocity increases and is met by a abrupt decrease in velocity at the leading edge, suggesting flow separation already at the leading edge of the aft foil. The pressure plot in figure 4.42 shows low pressure where one would suspect, but also surprisingly low pressure at the leading edge of the aft foil when compared the the previous sail configuration. However looking at the vorticity and Q-Criterion plots in figures 4.41 and 4.39 respectively the low pressure can be explained by the presence of vorticity dominated flow, which causes reduced pressure. As suspected there is some flow separation at the leading edge and vorticity dominated flow in the regions where velocity increases. Furthermore the flow separation on the leading edges of both foils is quite well illustrated in figure 4.41.

4.2.1.7 Ratio 90/10 with no gap and no camber

Below the results for different AoA are presented for the setup of the two element foil sail with a chord length ratio of 90 and 10 for the front and aft foil respectively. In the setup of the simulations the distance between the aft of the bigger foil and the front of the smaller foil was set to be zero.

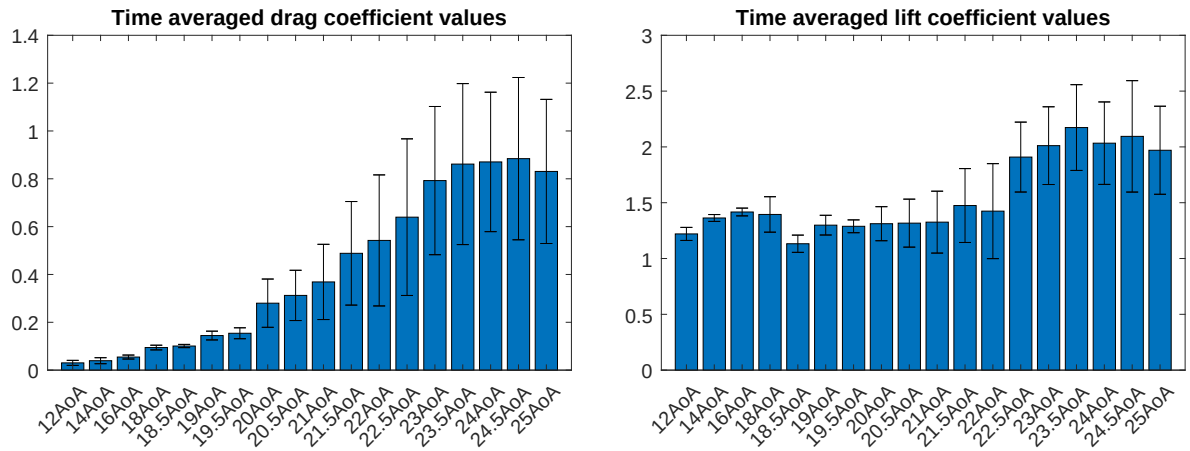

(a) Drag force coefficients **(b)** Lift force coefficients

Figure 4.43: Time averaged force coefficient values

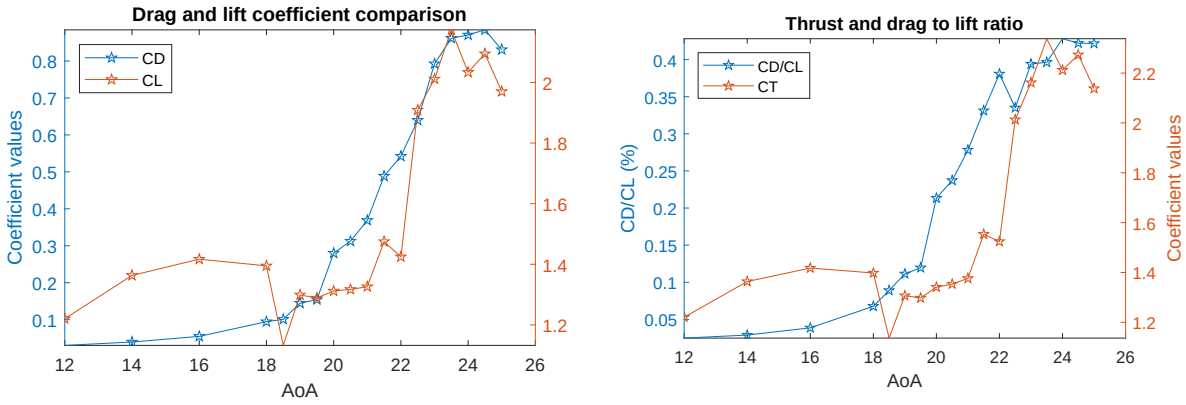

(a) Comparison of coefficients

(b) Thrust and size relation between coefficients

Figure 4.44: Time averaged force coefficient values

Interestingly in figure 4.43 (a) the drag coefficient values show almost no oscillation up until 19°AoA after which they begin to oscillate heavily, more so than the lift coefficient values for similar AoA in figure 4.43 (b). Another interesting thing to note is the appearance of a plateau in the lift coefficient values which can be observed in both figure 4.43 (b) and 4.44 (a). By looking at the previously mentioned figures it can also be seen that the maximum lift is achieved at 23.5°AoA followed by a decreasing trend, suggesting that stall occurs when the AoA is increased beyond this value. Lastly, stall behaviour is first observed after exceeding 16°AoA, which is later than for the other two wingsails with no gap and different ratios, and ends at 24.5°AoA.

The following table presents the AoA where the greatest thrust coefficient values were achieved

AoA	23.5AoA	24.5AoA	24AoA
C_T	2.3379	2.2735	2.2120

Table 4.8: The three greatest thrust coefficient values in descending order and the respective AoA

4.2.1.7.1 23.5AoA Here is a more in-depth look at the AoA which yielded the greatest maximum potential thrust.

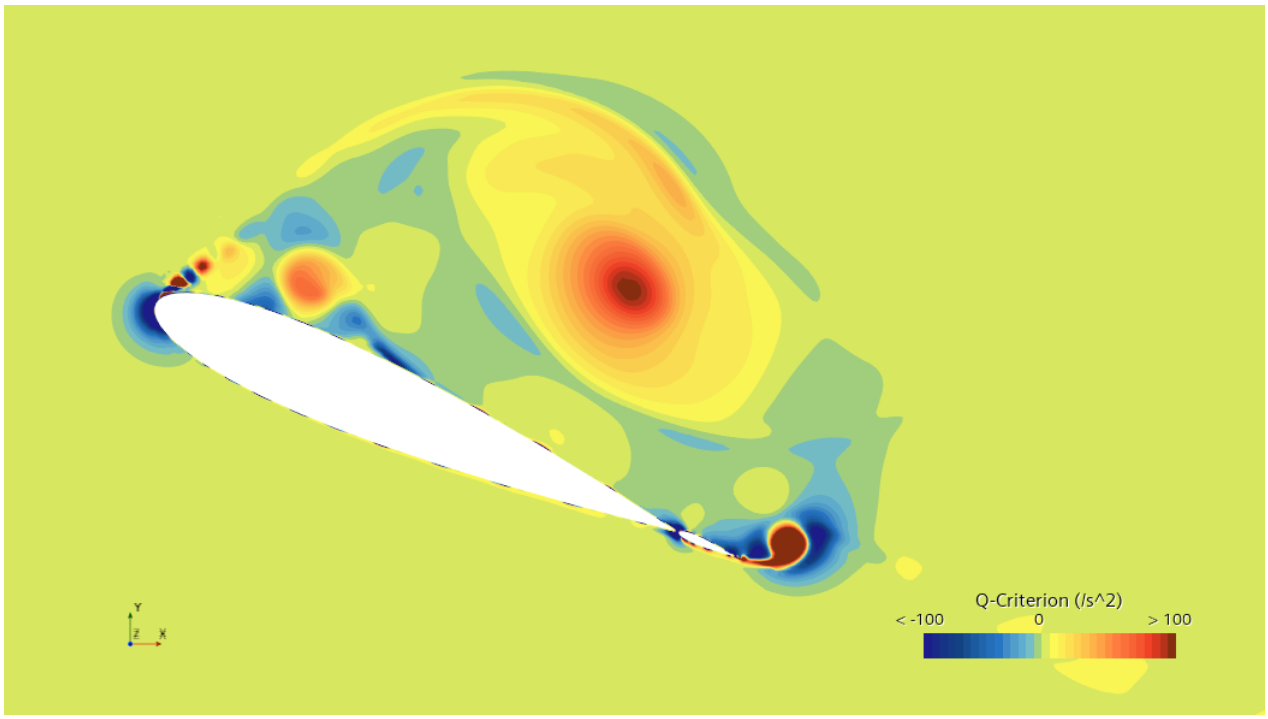

Figure 4.45: Q-Criterion at 120 000 iterations

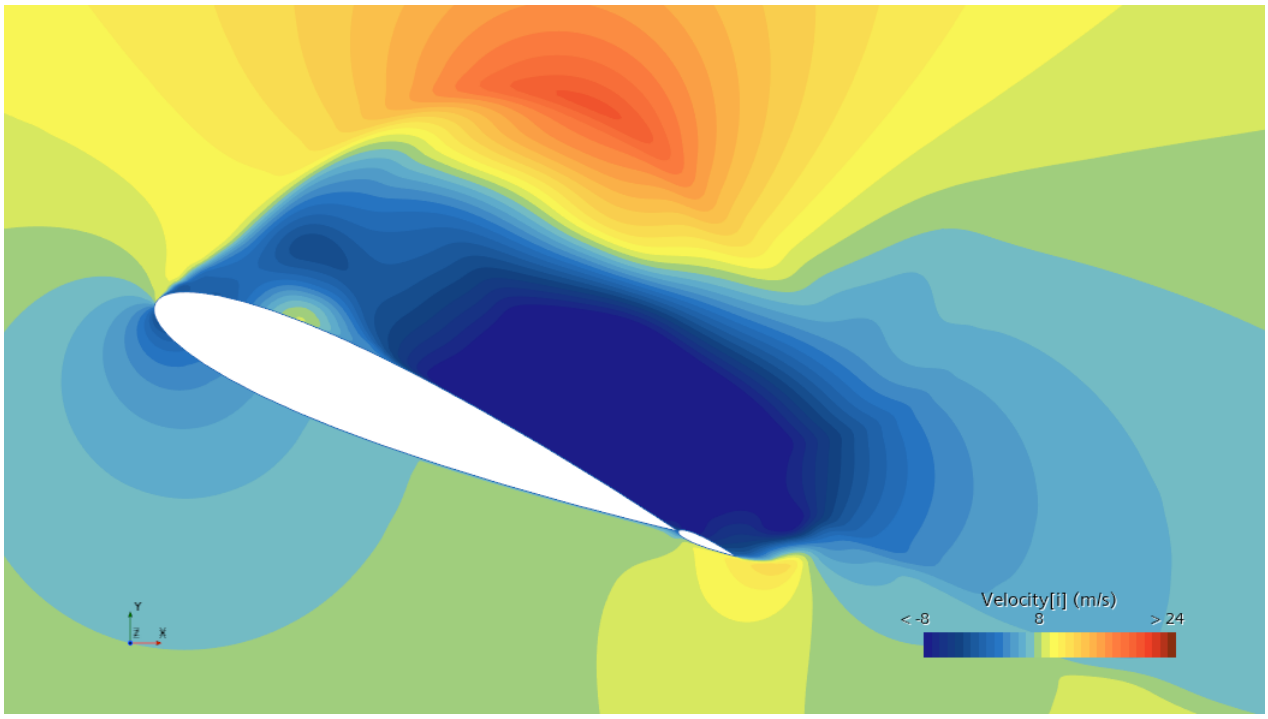

Figure 4.46: Velocity at 120 000 iterations

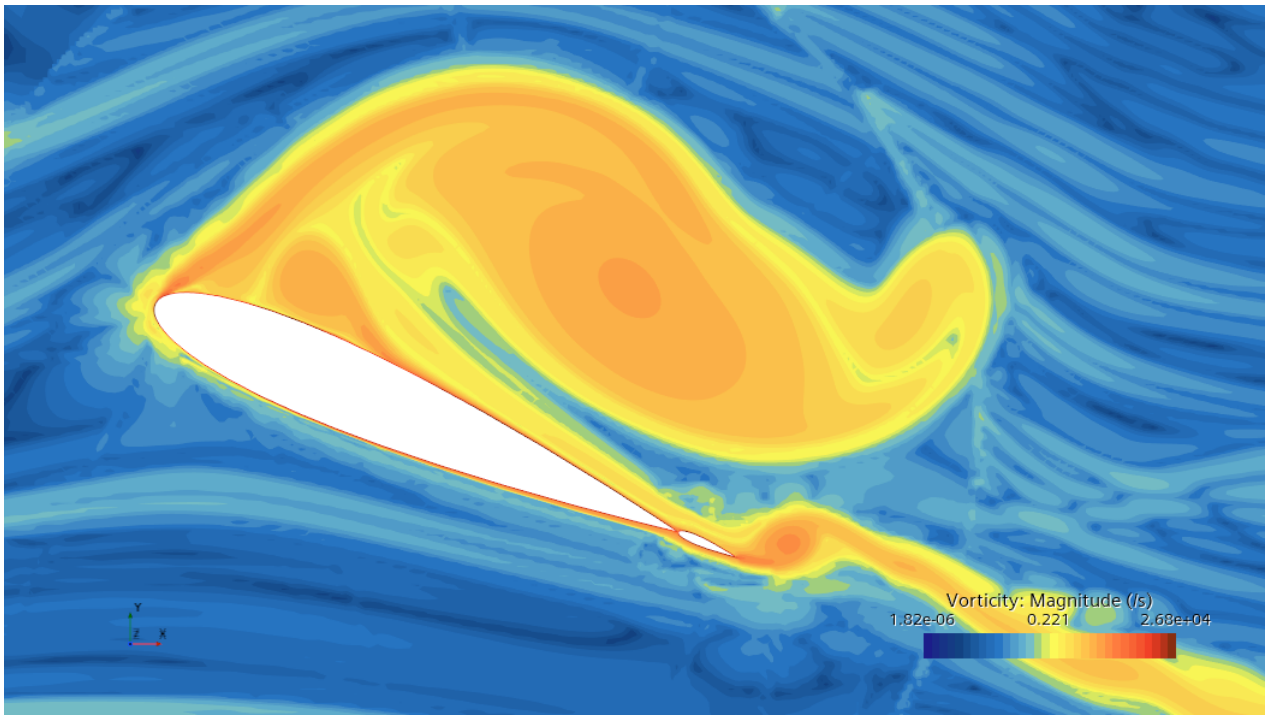

Figure 4.47: Vorticity at 120 000 iterations

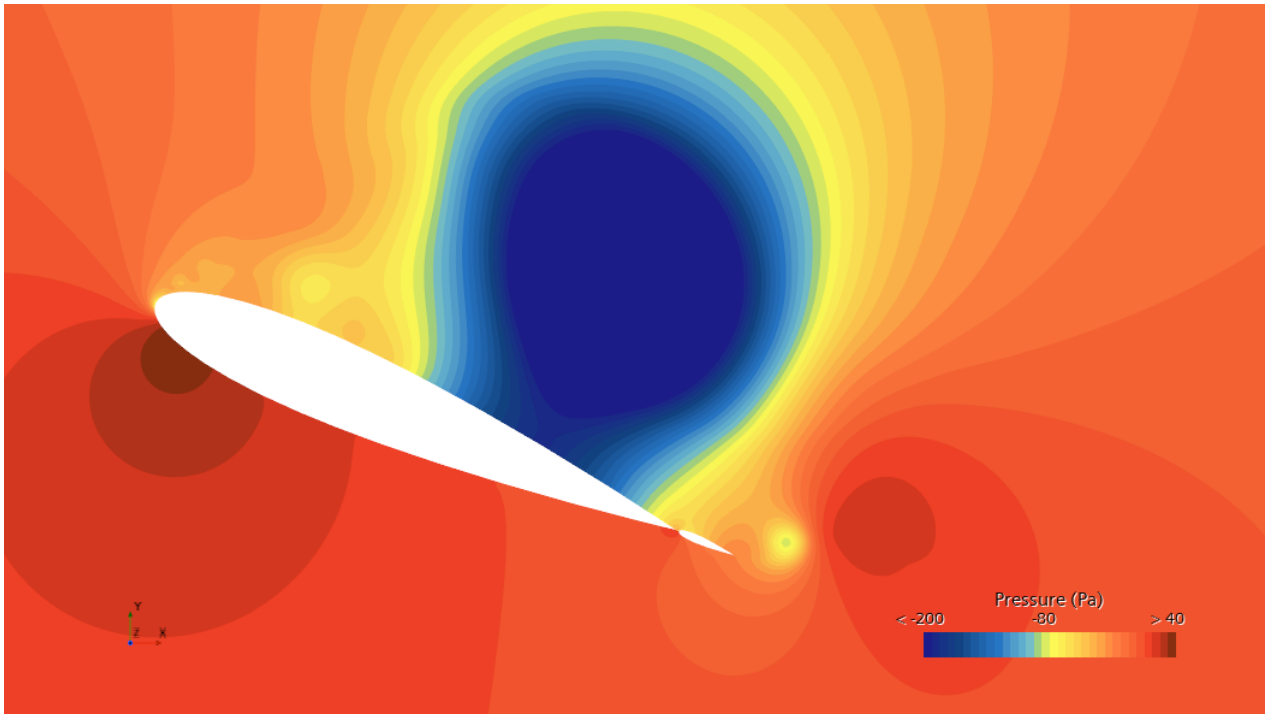

Figure 4.48: Pressure at 120 000 iterations

By observing the velocity plot in figure 4.46 a familiar sight is seen, with an increase in velocity on the upper surface close to the leading edge of the front foil, followed by a decrease to very low velocities. From prior results there is likely some separation

at the leading edge of the front foil with vortexes generated in the region with the velocity increase close to the trailing edge. However there is nothing yet to suggest any separation at the leading edge of the aft foil. Looking at the pressure plot in figure 4.48 it is possible that the APG will create flow separation on the surface of the foil where there is low pressure, which in turn might interact with the aft foil. The vorticity and Q-Criterion plots in figures 4.47 and 4.45 respectively however, show that vorticity dominates the flow above the foil and not at its upper surface, suggesting that the APG was not big enough. Furthermore the figures do show flow separation at the front foils leading edge and vorticity in the wake of the aft foils trailing edge.

4.2.1.8 Ratio 90/10 with 5% gap and no camber

Below the results for different AoA are presented for the setup of the two element foil sail with a chord length ratio of 90 and 10 for the front and aft foil respectively. In the setup of the simulations the distance between the aft of the bigger foil and the front of the smaller foil was set to be 0.7m, or 5% of the total length of the wings.

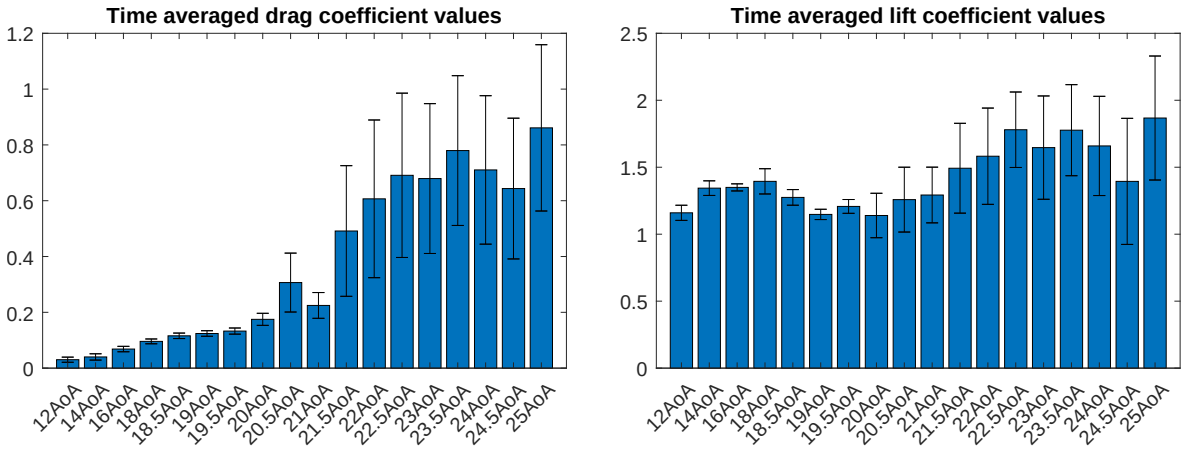

(a) Drag force coefficients **(b)** Lift force coefficients

Figure 4.49: Time averaged force coefficient values

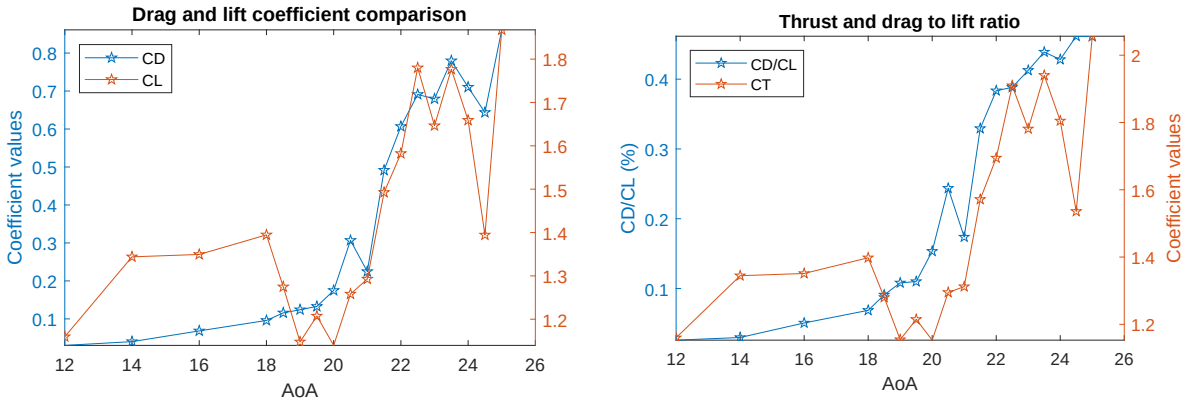

(a) Comparison of coefficients

(b) Thrust and size relation between coefficients

Figure 4.50: Time averaged force coefficient values

From figures 4.49 (b) and 4.50 (a) the maximum lift is seen at 25°AoA, hence making it the most likely stall angle for this gap distance configuration of the sail with ratio 90/10. Just as was the case for the wingsail with ratio 70/30, increasing the gap distance seems to have postponed the beginning of the stall range, now starting at 18°AoA and ending at 24°AoA.

The following table presents the AoA where the greatest thrust coefficient values were achieved

AoA	25AoA	23.5AoA	22.5AoA
C_T	2.0564	1.9402	1.9094

Table 4.9: The three greatest thrust coefficient values in descending order and the respective AoA

4.2.1.8.1 25AoA Here is a more in-depth look at the AoA which yielded the greatest maximum potential thrust.

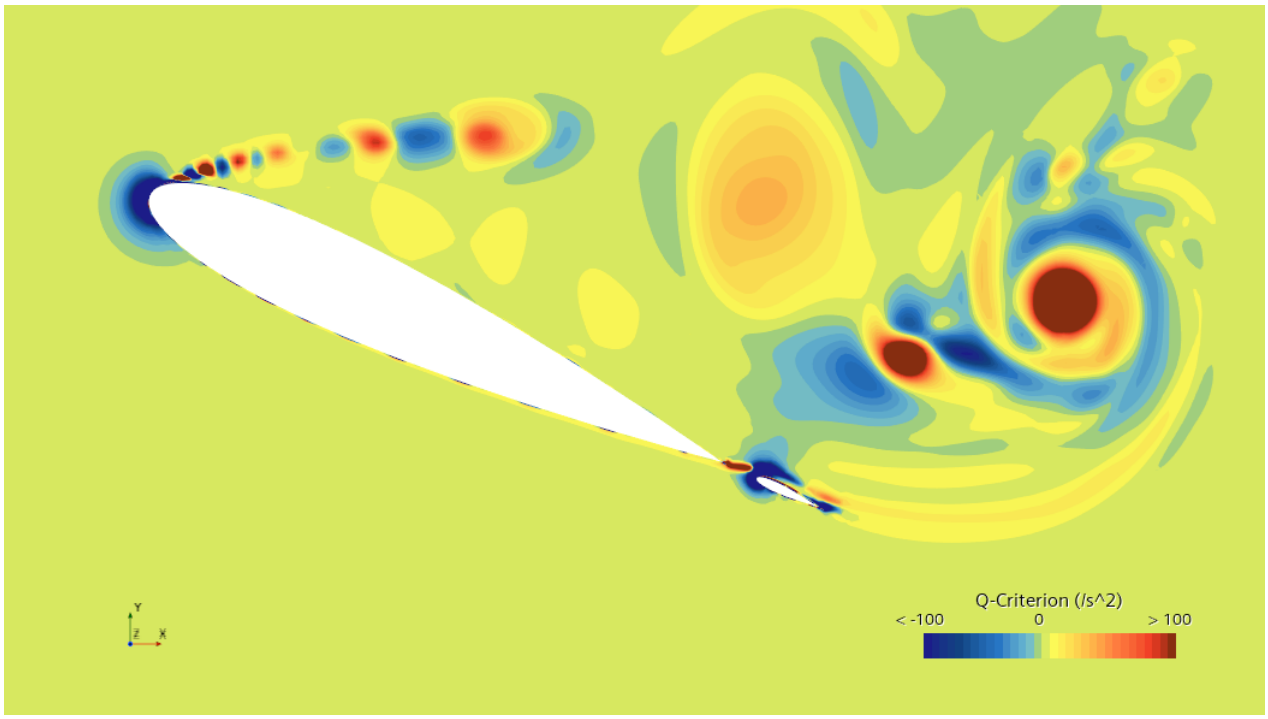

Figure 4.51: Q-Criterion at 120 000 iterations

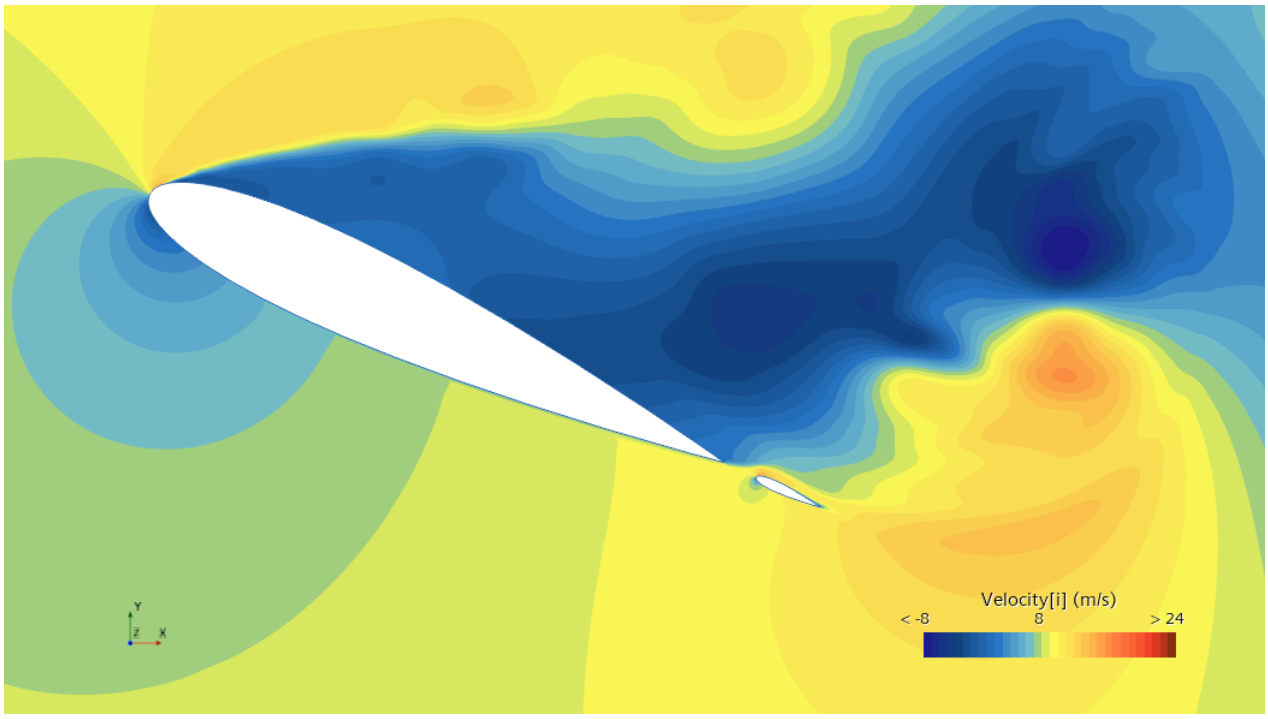

Figure 4.52: Velocity at 120 000 iterations

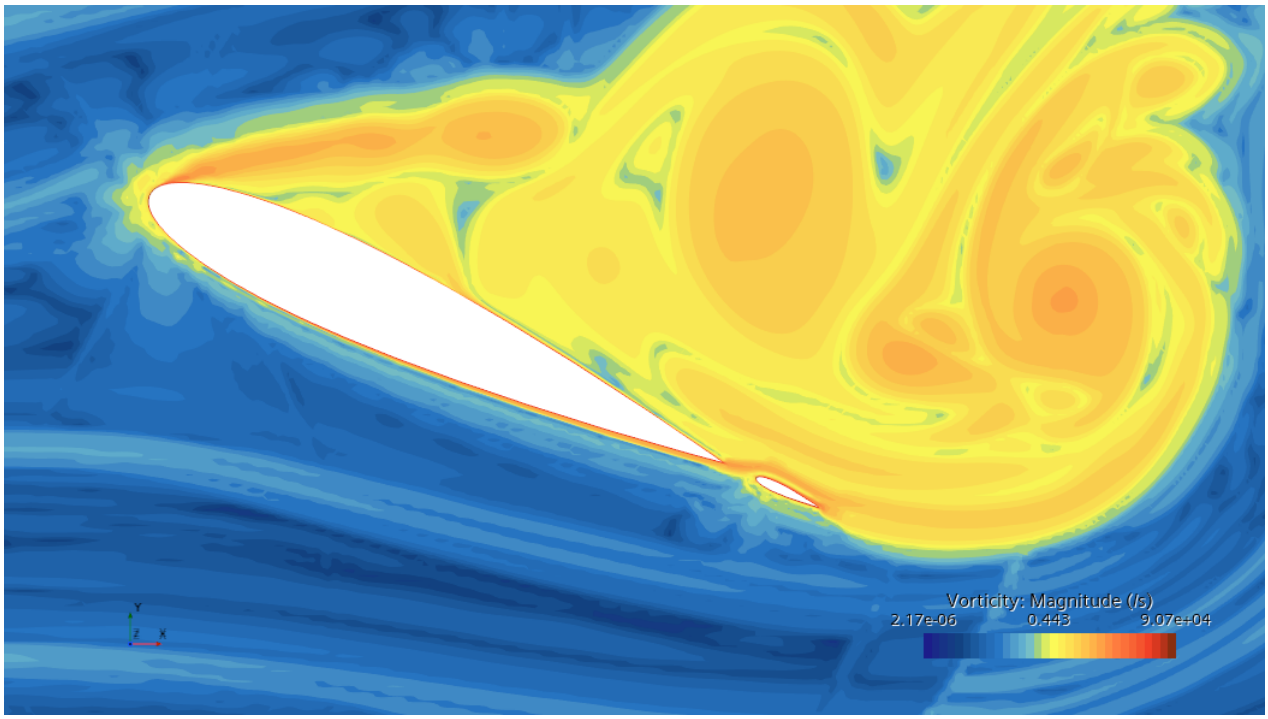

Figure 4.53: Vorticity at 120 000 iterations

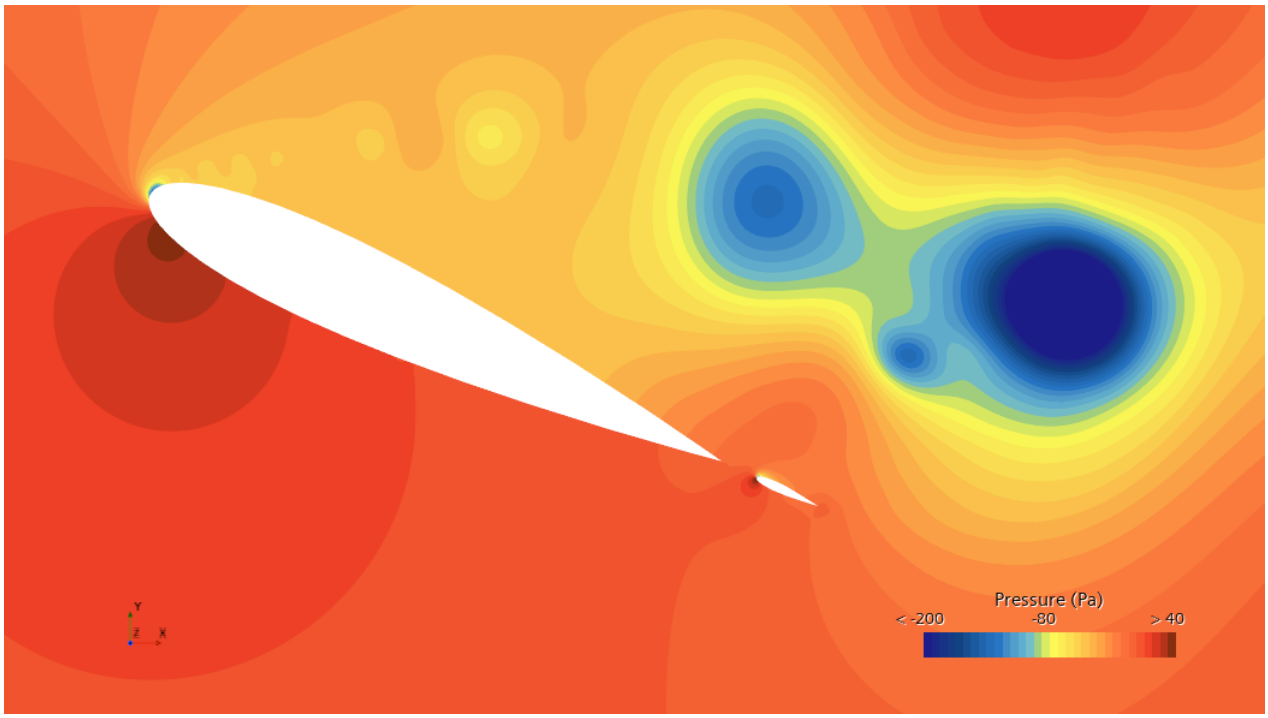

Figure 4.54: Pressure at 120 000 iterations

4.2.1.9 Ratio 90/10 with 10% gap and no camber

Below the results for different AoA are presented for the setup of the two element foil sail with a chord length ratio of 90 and 10 for the front and aft foil respectively.

In the setup of the simulations the distance between the aft of the bigger foil and the front of the smaller foil was set to be 1.4m, or 10% of the total length of the wings.

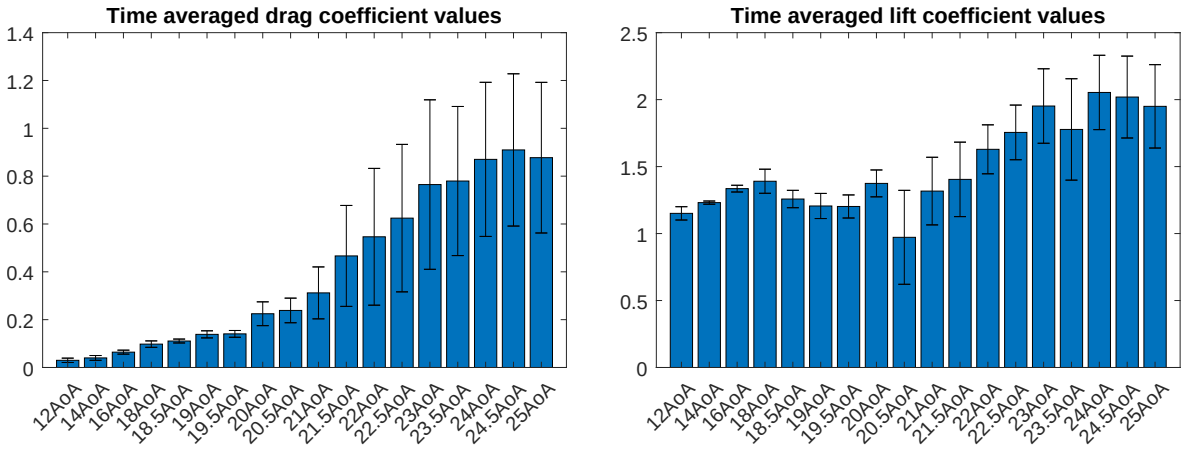

(a) Drag force coefficients

(b) Lift force coefficients

Figure 4.55: Time averaged force coefficient values

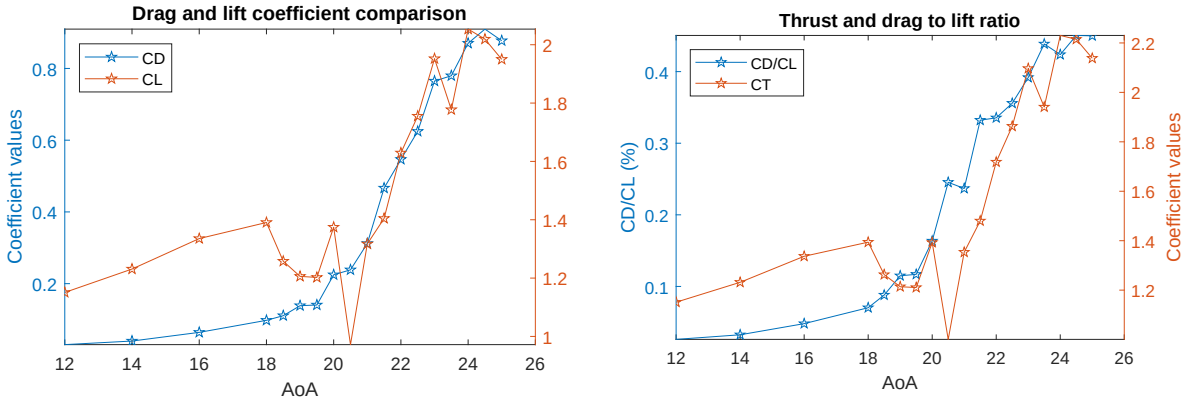

(a) Comparison of coefficients

(b) Thrust and size relation between coefficients

Figure 4.56: Time averaged force coefficient values

In figure 4.55 (b) a smooth decline in lift, followed by an increase and then immediate strong decrease followed by a steep increase can be seen, but perhaps best observed in figure 4.56 (a). Increasing the gap distance from 5 to 10% does not seem to have postponed the stall behaviour as it did for the wingsail with ratio 70/30, as it once again begins at 18°AoA and ends at 24.5°AoA. The most likely stall angle is

24°AoA as maximum lift is achieved at this point, and further increasing the AoA does not increase lift, as shown in table 4.10.

The following table presents the AoA where the greatest thrust coefficient values were achieved

AoA	24AoA	24.5AoA	25AoA
C_T	2.2303	2.2147	2.1381

Table 4.10: The three greatest thrust coefficient values in descending order and the respective AoA

4.2.1.9.1 24AoA Here is a more in-depth look at the AoA which yielded the greatest maximum potential thrust.

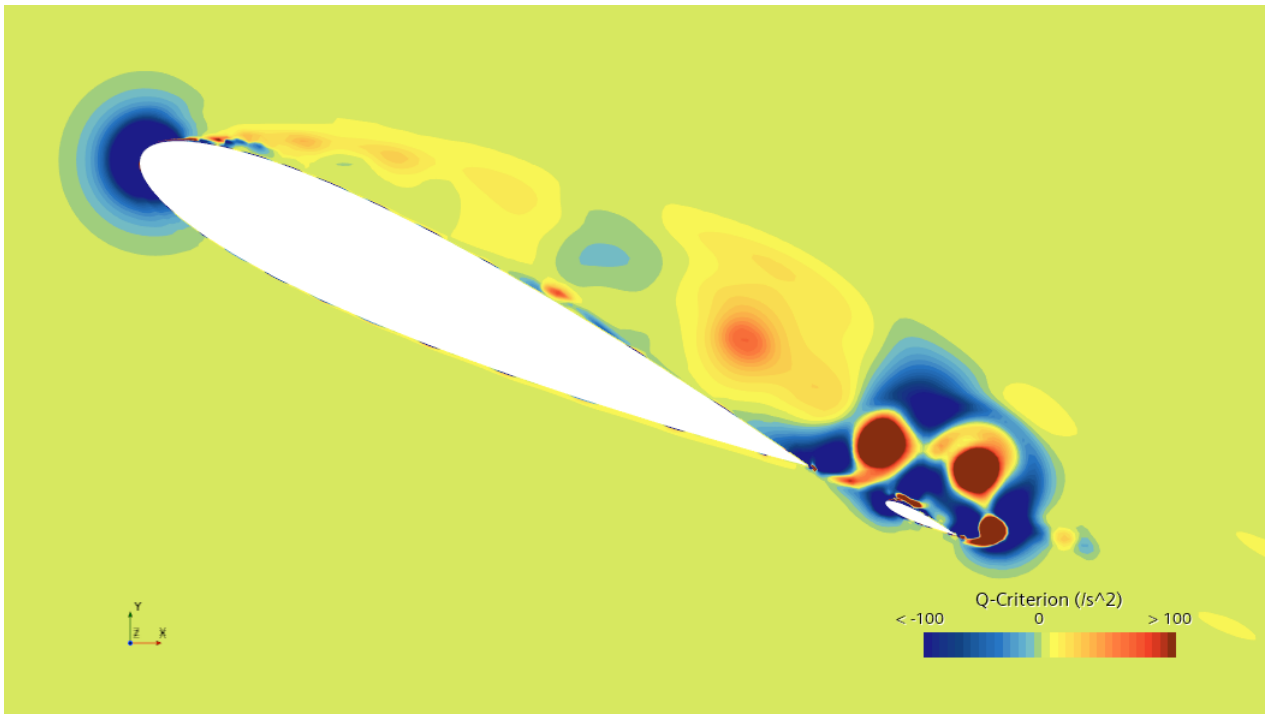

Figure 4.57: Q-Criterion at 120 000 iterations

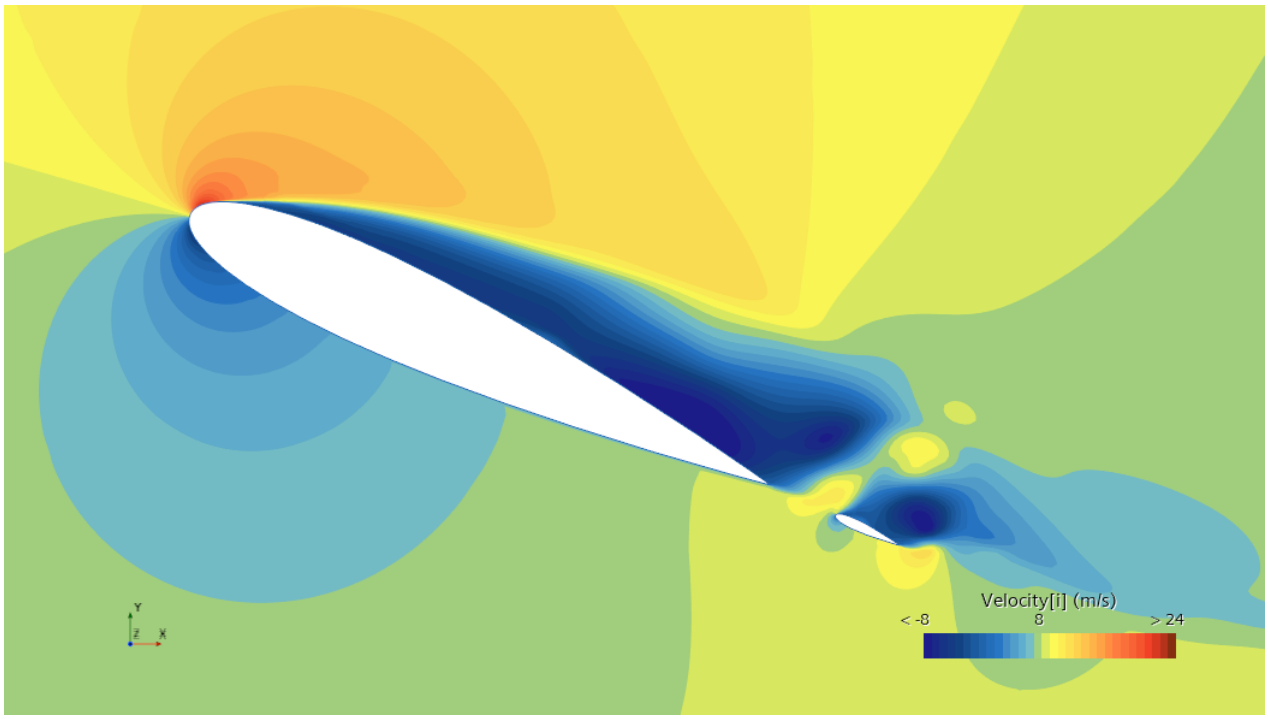

Figure 4.58: Velocity at 120 000 iterations

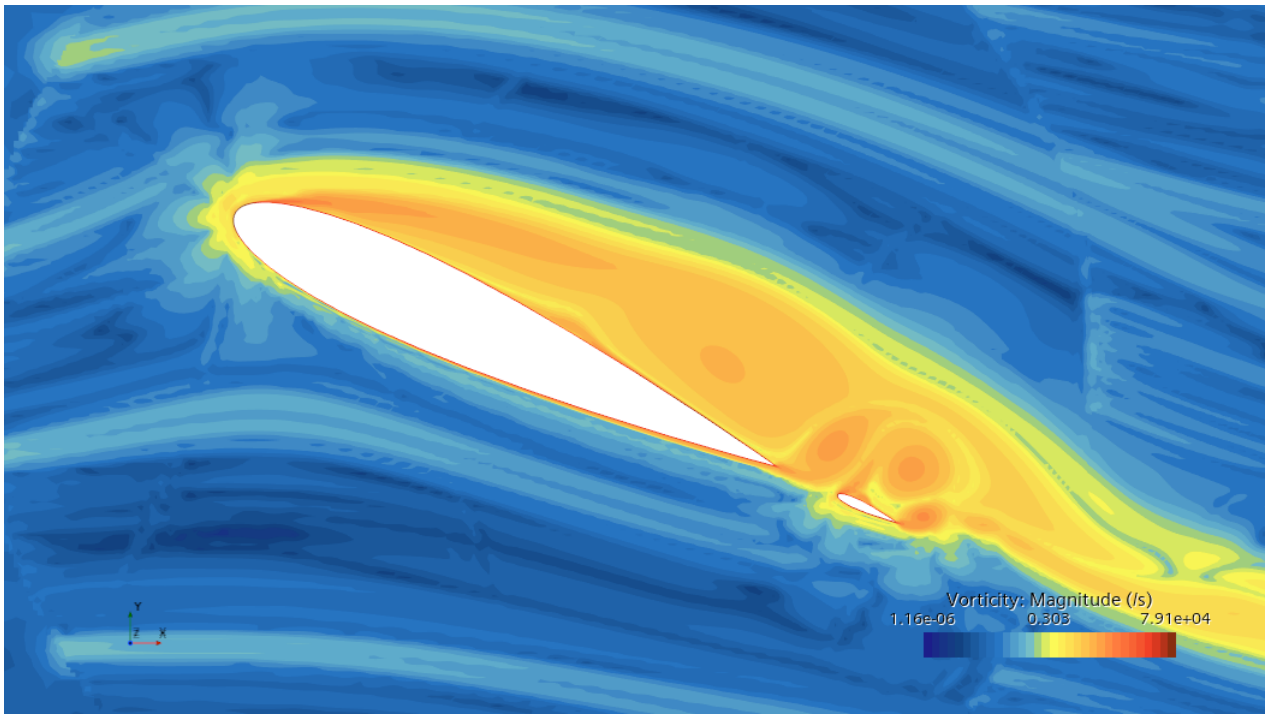

Figure 4.59: Vorticity at 120 000 iterations

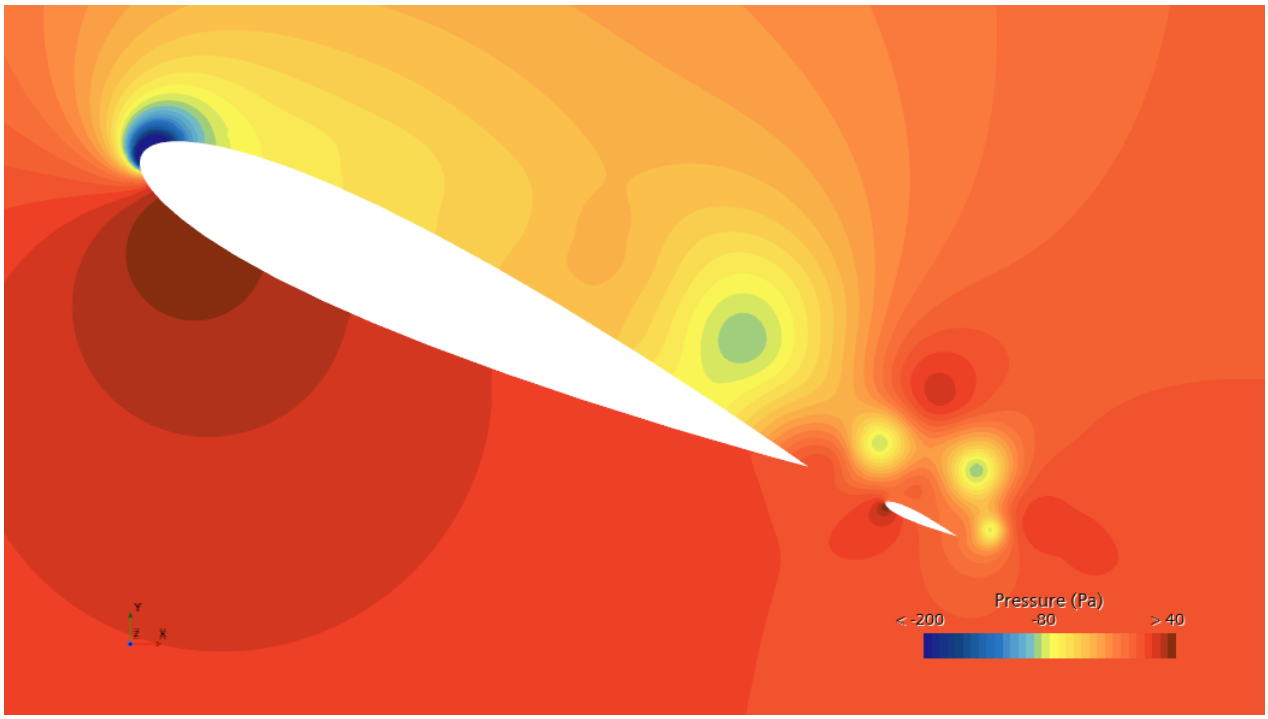

Figure 4.60: Pressure at 120 000 iterations

In comparison to what has previously been observed there is now a rather large increase in velocity at the leading edge upper surface of the front foil, as seen in figure 4.58, which then quickly decreases close to the surface and suggests, as usual, that there might be a high APG there. At about half the chord-length of the front foil the velocity increases slightly and then reduces to very low velocities, which might also indicate a high APG. Looking at the pressure plot in figure 4.60 there is indeed quite low pressure at the front foils leading edge surrounded by higher pressure along the surface downstream. However when looking at figure 4.59 it can be seen that there isn't a lot of vorticity in comparison to previous cases and figure 4.57 shows that the flow at the leading edge is majorly dominated by strain. The figure also shows that there is some vorticity dominated flow close to the half-chord length mentioned earlier, and vorticity dominated flow leaving the trailing edges of both foils and the leading edge of the aft foil, which is also well illustrated in figure 4.59.

4.2.2 Comparison of gap distance effect on force coefficients

This section will present results in order to try and measure the amount of influence the gap distance has on the performance of the rigid wingsails.

4.2.2.1 Ratio 70/30

Below are the 2D results from the two element foil sail with ratio 70/30.

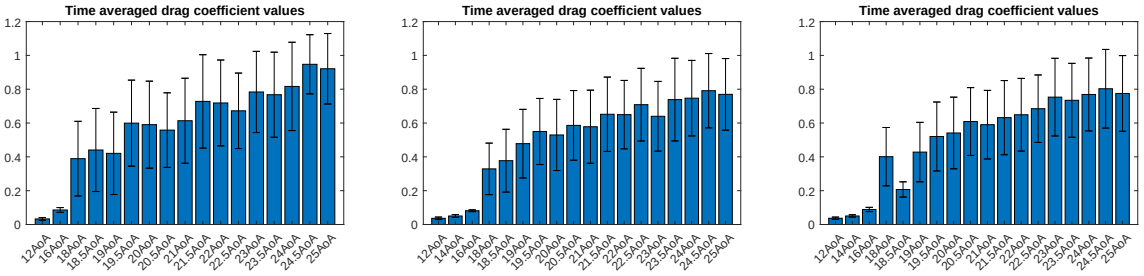

Figure 4.61: From left to right: No gap, 5% gap and 10 % gap

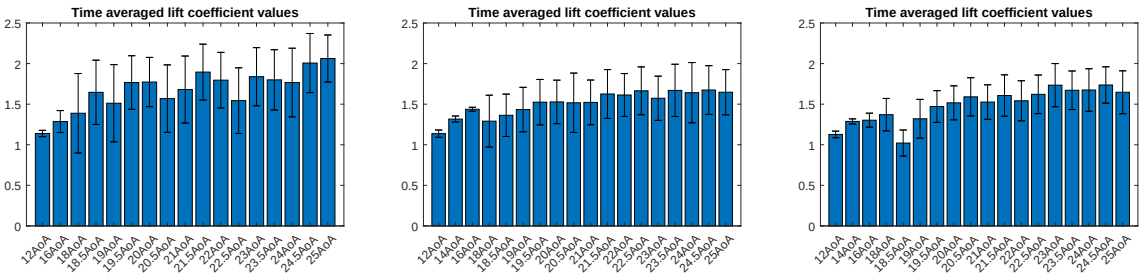

Figure 4.62: From left to right: No gap, 5% gap and 10 % gap

From the bar plots in figures 4.61 and 4.62 it is seems like the sail setup with no gap between the front and aft wing is a quite superior design to the ones with gaps, which does seem to have similar performance to each-other. Furthermore, as was previously mentioned, looking at figure 4.62 it can be seen that the AoA at which stall behaviour can first be observed changes slightly with altering gap distances.

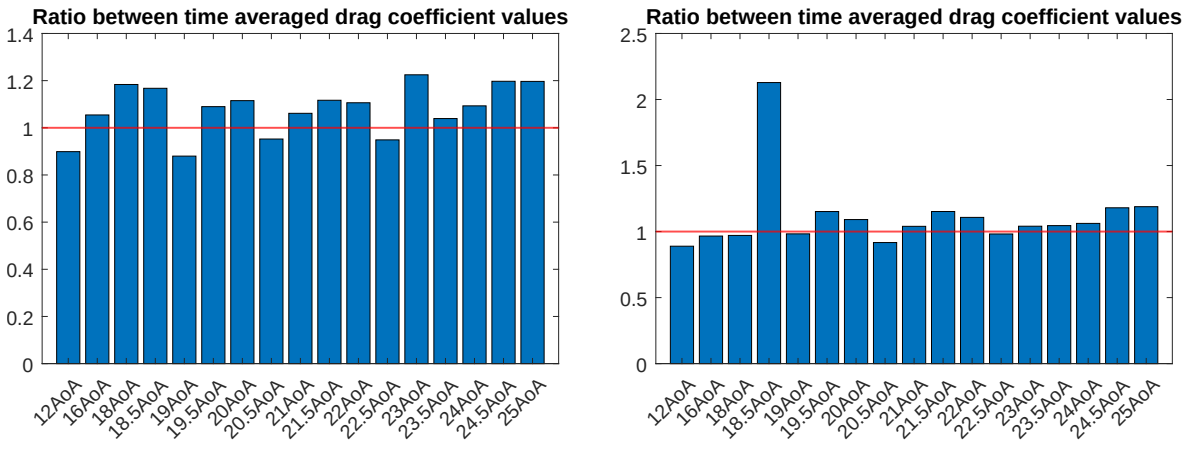

(a) Coefficient ratios between 0% and 5% gap

(b) Coefficient ratios between 0% and 10% gap

Figure 4.63: Comparison of ratios of time averaged force coefficient values

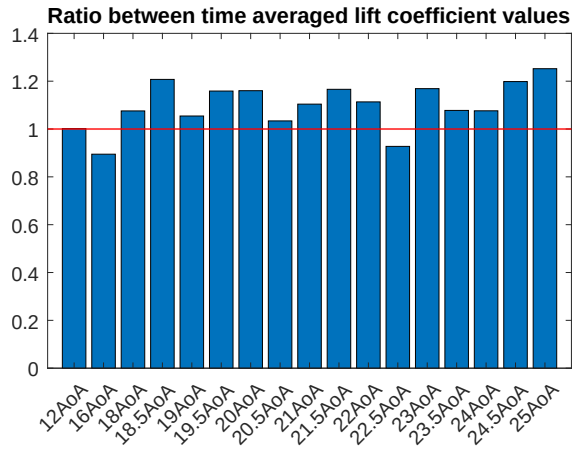

(a) Coefficient ratios between 0% and 5% gap

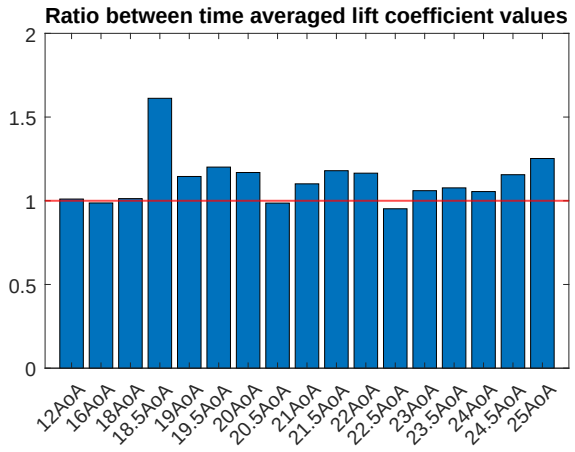

(b) Coefficient ratios between 0% and 10% gap

Figure 4.64: Comparison of ratios of time averaged force coefficient values

From figures 4.63 and 4.64 it is observed that for the majority of the AoA studied in this project, the setup with no gap yields better results compared to those with a gap. Furthermore there are some notable peaks for the largest gap distance in these graphs, but overall it is visually hard to discern which gap distance between 5 and 10% is better.

The following table shows the mean ratios calculated from the force coefficient ratios of all AoA for both lift and drag, for different gap sizes.

Gap ratio	Lift	Drag
No gap / 5% gap	1.0983	1.0780
No gap / 10% gap	1.1248	1.1114

Table 4.11: Mean ratios of force coefficients between different gap sizes

From table 4.11 it can be seen that a larger gap distance has a negative effect on the performance when looking at both drag and lift. The larger the gap distance, the worse the performance. This can also be seen if the mean values of the time averaged lift and drag coefficients for 10 percent are divided by those for 5 percent, in which case one can see that the mean time averaged lift force coefficient for a 10 percent gap, is 98 percent of that for a 5 percent gap, and for the drag it is in the case of a 10 percent gap 99.7 percent of the case of a 5 percent gap.

4.2.2.2 Ratio 80/20

Below are the 2D results from the two element foil sail with ratio 80/20.

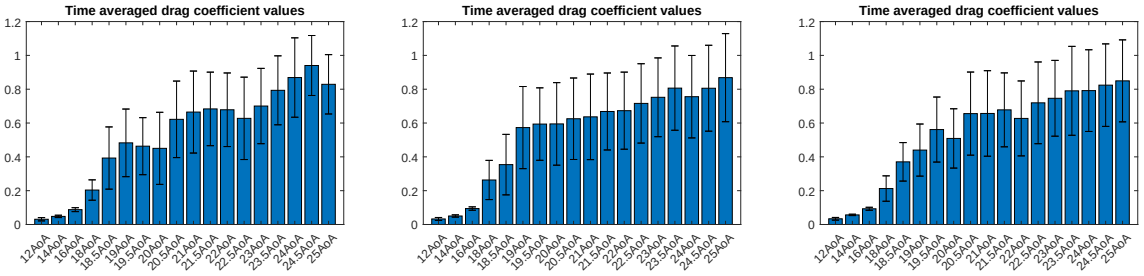

Figure 4.65: From left to right: No gap, 5% gap and 10 % gap

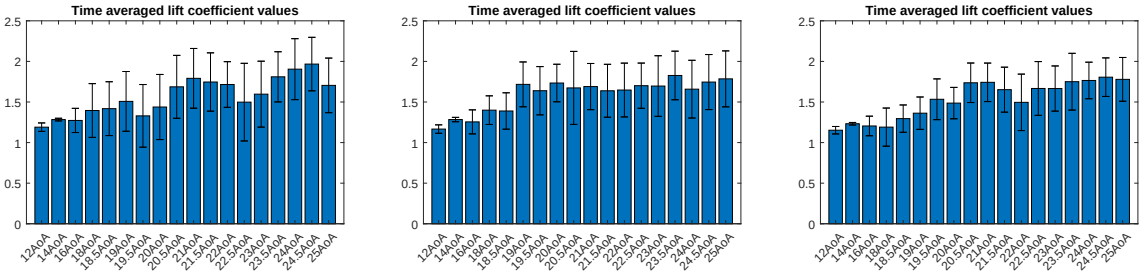

Figure 4.66: From left to right: No gap, 5% gap and 10 % gap

From figures 4.65 and 4.66 alone it is hard to easily discern which gap distance would be favourable. However by inspecting the barplots in figure 4.67 it can be seen that in a majority of the cases having a gap of 5 and 10% yields greater drag values than having no gap at all. In contrast the option of no gap distance seem to give better lift for more cases in figure 4.68, but it actually performs worse overall, as seen in table 4.12.

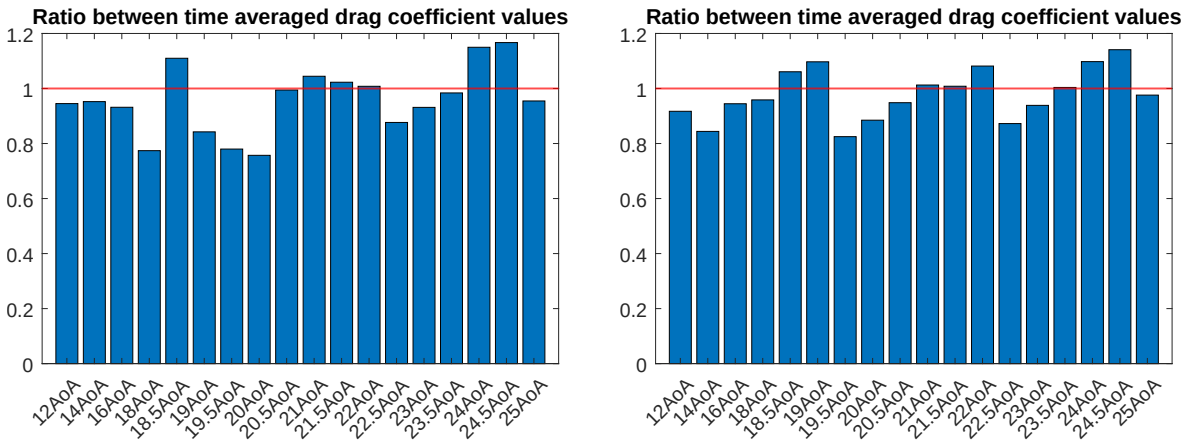

(a) Coefficient ratios between 0% and 5% gap

(b) Coefficient ratios between 0% and 10% gap

Figure 4.67: Comparison of ratios of time averaged force coefficient values

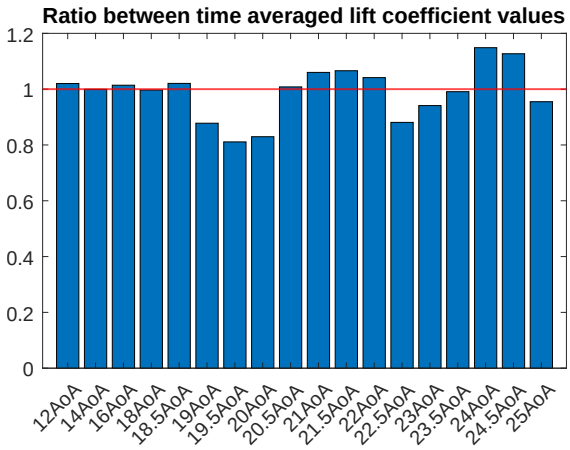

(a) Coefficient ratios between 0% and 5% gap

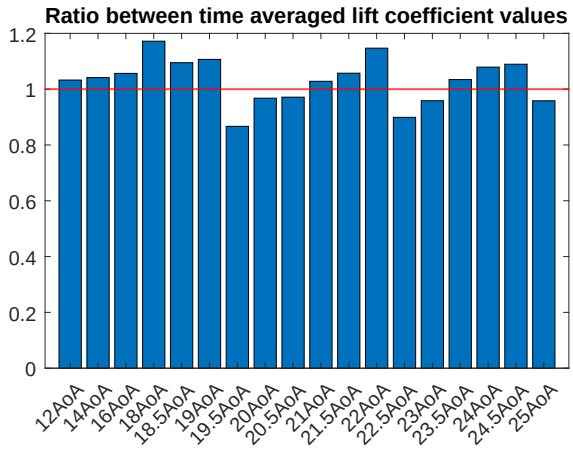

(b) Coefficient ratios between 0% and 10% gap

Figure 4.68: Comparison of ratios of time averaged force coefficient values

The following table shows the mean ratios calculated from the force coefficient ratios of all AoA for both lift and drag, for different gap sizes.

Gap ratio	Lift	Drag
No gap / 5% gap	0.9883	0.9570
No gap / 10% gap	1.0311	0.9785

Table 4.12: Mean ratios of force coefficients between different gap sizes

From table 4.12 it can be seen that, in contradiction to table 4.11, a larger gap distance seems to increase performance. However as the gap distance increases further the performance of both the lift and drag decreases. If the mean values of the time averaged lift and drag coefficients for 10 percent are divided by those for 5 percent, then once can see that the mean time averaged lift force coefficient for a 10 percent gap is 96 percent of that for a 5 percent gap, and for the drag it is in the case of a 10 percent gap, 98 percent of the case of a 5 percent gap.

4.2.2.3 Ratio 90/10

Below are the 2D results from the two element foil sail with ratio 90/10.

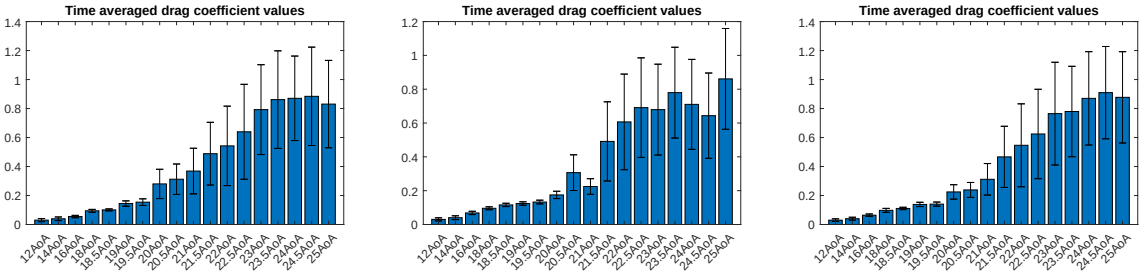

Figure 4.69: From left to right: No gap, 5% gap and 10 % gap

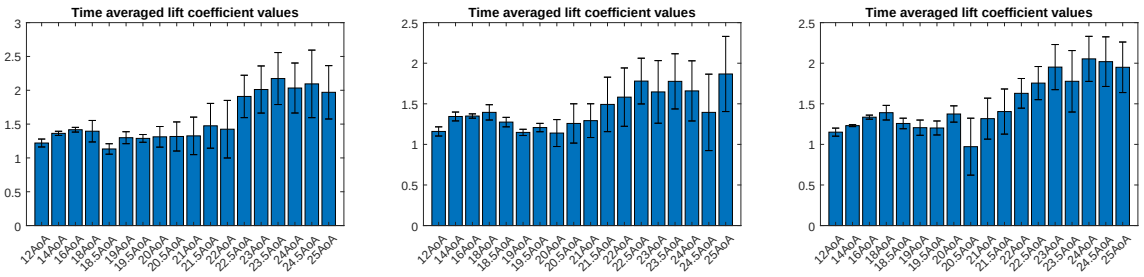

Figure 4.70: From left to right: No gap, 5% gap and 10 % gap

Inspecting figure 4.69 and 4.70 it can be seen that all cases follow a similar curve but it seems like the case of no gap reaches greater peaks if the standard deviations are taken into account.

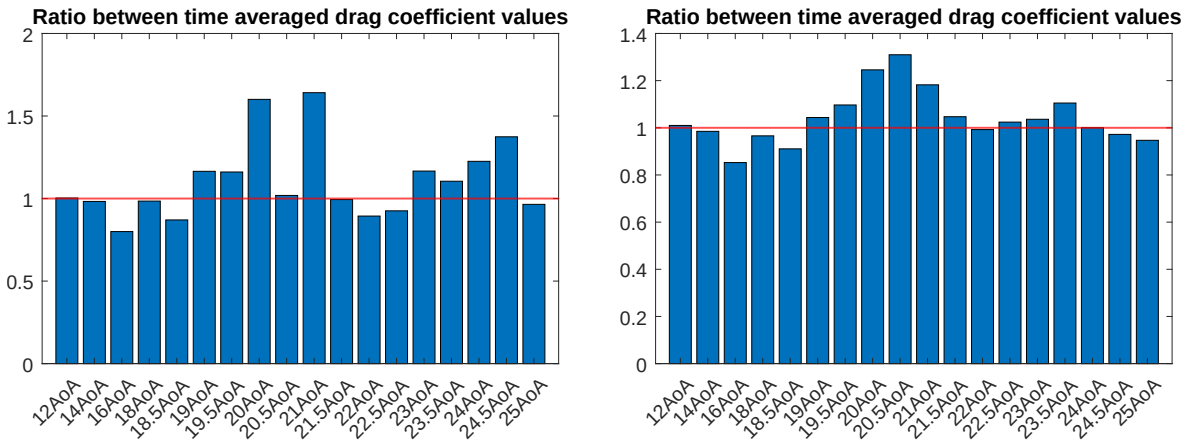

(a) Coefficient ratios between 0% and 5% gap

(b) Coefficient ratios between 0% and 10% gap

Figure 4.71: Comparison of ratios of time averaged force coefficient values

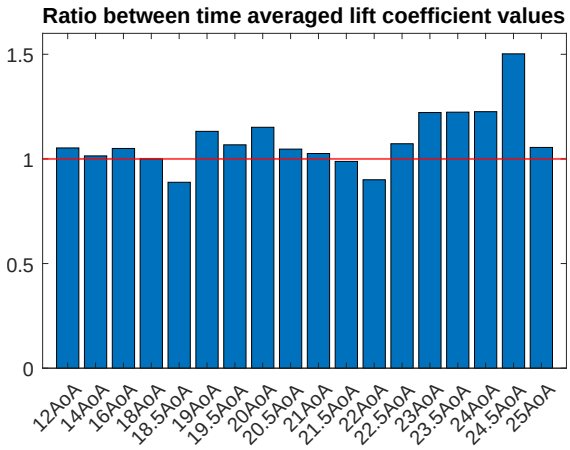

(a) Coefficient ratios between 0% and 5% gap

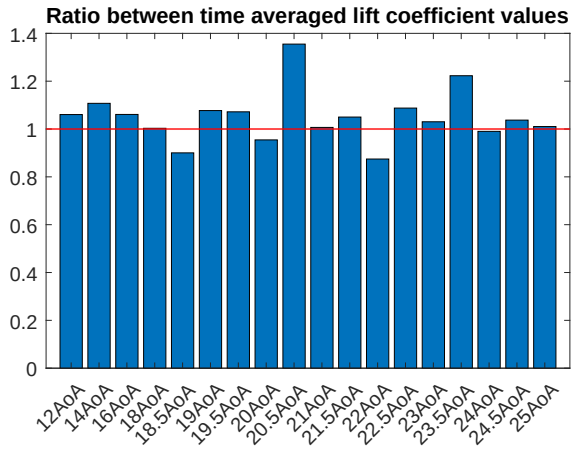

(b) Coefficient ratios between 0% and 10% gap

Figure 4.72: Comparison of ratios of time averaged force coefficient values

In figure 4.71 the case of no gap yields greater drag coefficient values in a slight majority of the AoA cases studied, while figure 4.72 it gives better lift coefficient in a confident majority of the cases studied. The peaks that can be observed in these figures are explained by a loss of lift, which can be observed if figures 4.69 and 4.71 are compared to each-other for the drag, and likewise with the corresponding figures for the lift.

The following table shows the mean ratios calculated from the force coefficient ratios of all AoA for both lift and drag, for different gap sizes.

Gap ratio	Lift	Drag
No gap / 5% gap	1.0898	1.1043
No gap / 10% gap	1.0500	1.0404

Table 4.13: Mean ratios of force coefficients between different gap sizes

From table 4.13 it can be seen that, in some contradiction to table 4.12, and in some agreement with table 4.11 a greater gap distance affects the performance in a negative manner, initially. However it is interesting to note that unlike any of the other two tables it seems like a gap distance of 10% performs better than a gap distance of 5%, since the ratios in table 4.13 decreases for a greater gap. The mean value of the ratios of the time-averaged lift coefficients for 10% gap divided by those for a 5% gap show that having a 10% gap is 4.4% better than a 5% gap. If the same is done for the time-averaged drag coefficients then the option of a 10% gap is 5.9% better than having a 5% gap.

4.2.2.4 Polar plot comparison between non-cambered two element foils and crescent-shaped sail

The first polar plots in this section compares each two-foil sails configurations for all possible apparent wind angles to see which configuration gives the greatest results. Please be reminded that the configurations that are included in these polar plots are those which yielded the greatest maximum potential thrust according to equation (2.5), but the thrust in the polar plots are calculated using equation (2.1). Meaning that the vertical axis in the polar plots denote the thrust coefficient value according to equation (2.1). Since each gap-configuration shown in the polar plots respond to an AoA that yielded the biggest maximum potential thrust, the AoA in question will be denoted as α_0, α_5 and α_{10} for the distances 0%, 5% and 10% respectively.

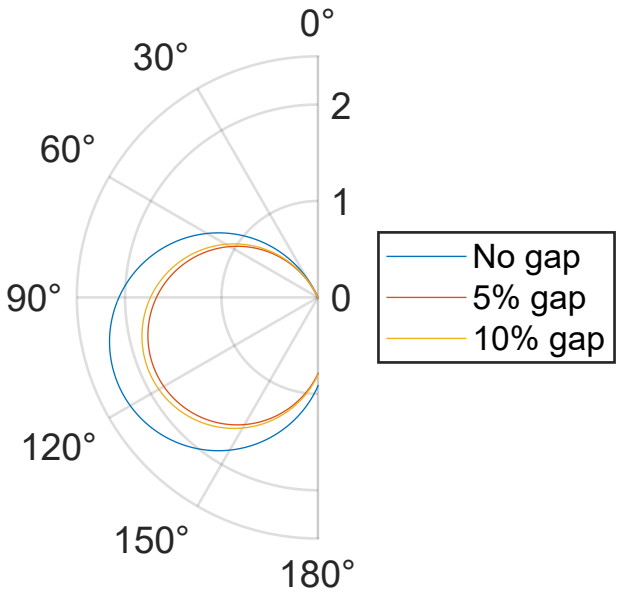

Figure 4.73: Polar plot of the thrust coefficient for the two element foil sail with a ratio of 70/30, at a wide span of apparent wind angles for $\alpha_0 = 25$, $\alpha_5 = 24.5$ and $\alpha_{10} = 24.5$

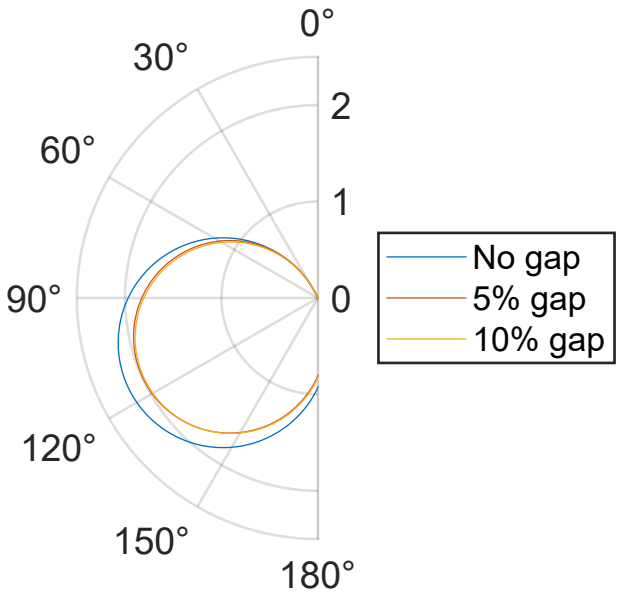

Figure 4.74: Polar plot of the thrust coefficient for the two element foil sail with a ratio of 80/20, at a wide span of apparent wind angles for $\alpha_0 = 24.5$, $\alpha_5 = 23.5$ and $\alpha_{10} = 24.5$

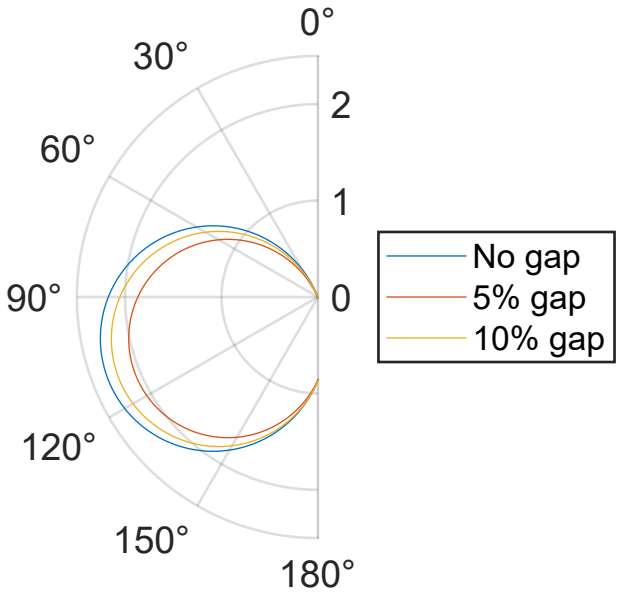

Figure 4.75: Polar plot of the thrust coefficient for the two element foil sail with a ratio of 90/10, at a wide span of apparent wind angles for $\alpha_0 = 23.5$, $\alpha_5 = 25$ and $\alpha_{10} = 24$

Although previous results from tables 4.13 and 4.12 make it seem like having a gap might give better results the polar plots 4.73, 4.74 and 4.75 above give a more comprehensive overview. The plots clearly show that having no gap between the foils is the superior design choice. However, somewhat unintuitively the figures also seem to show that a bigger gap performs better than a smaller one.

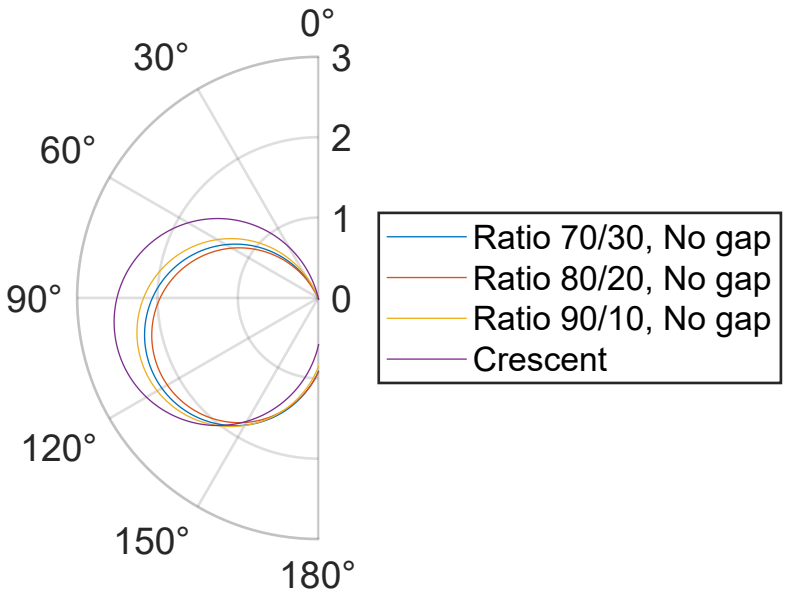

Figure 4.76: Polar plot comparison for different sail types where $\alpha_{70/30} = 25$, $\alpha_{80/20} = 24.5$, $\alpha_{90/10} = 23.5$, $\alpha_{D2R8} = 20.5$.

Comparing the best designs in the previous three plots 4.73, 4.74 and 4.75 at their respective AoA to each-other and to the crescent-shaped wingsail at an AoA of $\alpha_{D2R8} = 20.5°$ in figure 4.76 it becomes clear that, at least without any camber to them, the crescent-shaped wingsail performs significantly better than any of the two foil designs.

4.2.3 Cambered two foil results

Remember that for each ratio there was a gap distance that yielded the best propulsive performance, as seen in figures 4.73, 4.74 and 4.75 above. The thrust from these gap distances were in turn calculated at the AoA, (denoted α_0, α_5 and α_{10} in the aforementioned polar plots), for each respective distance, that yielded the greatest maximum potential thrust. The cambered results below are from the two foil simulations for all ratios at these gap distances and angles of attack.

4.2.3.1 Cambered 70/30

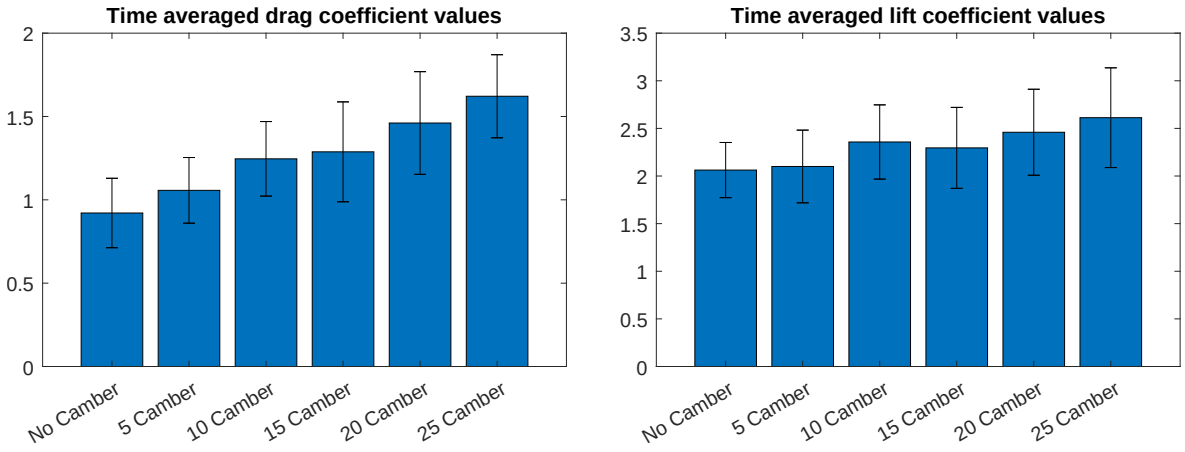

(a) Drag force coefficients

(b) Lift force coefficients

Figure 4.77: Time averaged force coefficient values

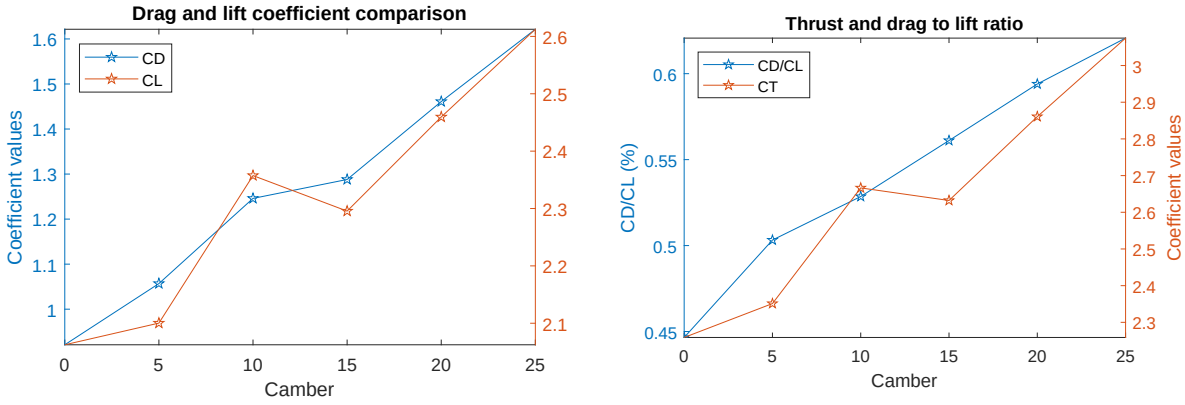

(a) Comparison of coefficients

(b) Thrust and size relation between coefficients

Figure 4.78: Time averaged force coefficient values

The following table presents the camber angles where the greatest thrust coefficient values were achieved

Camber	25	20	10
C_T	3.0748	2.8607	2.6664

Table 4.14: The three greatest thrust coefficient values in descending order and the respective camber angle

From the bar and line plots above the positive effect that camber has on the maximum potential thrust is hard to miss. If the greatest value in table 4.14, which is for a camber angle of 25°is compared to the greatest value in table 4.2 which is for no camber angle, then it can be seen that the maximum potential thrust has increased by 36%.

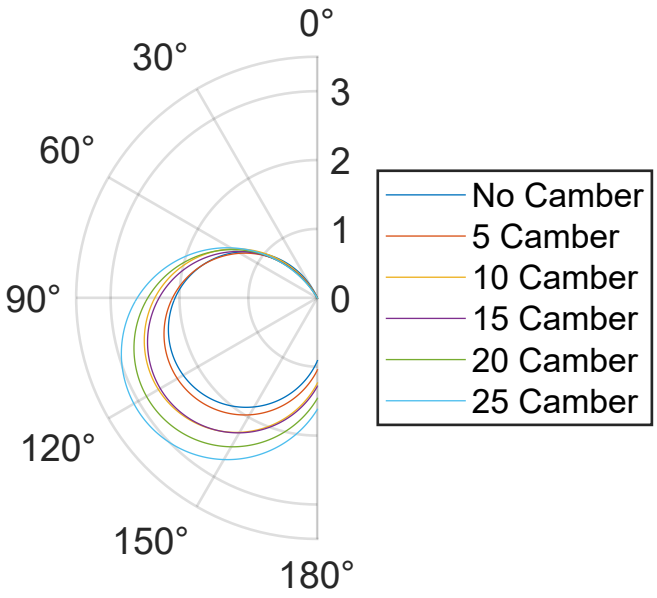

Figure 4.79: Polar plot comparison of the effect of different camber angles on the thrust of the sail at a wide span of apparent wind angles

Looking at figure 4.79 the positive difference that camber makes on the full range of apparent wind angles can not be understated. From the figure it can be inferred that greater camber gives better propulsion, with the exception of 10° and 15° which have some overlap.

4.2.3.2 Cambered 80/20

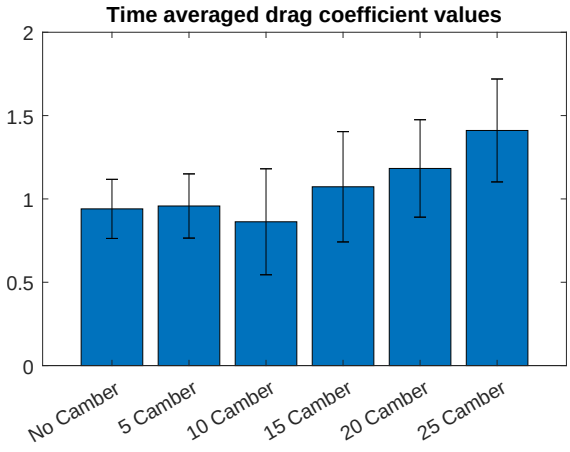

(a) Drag force coefficients

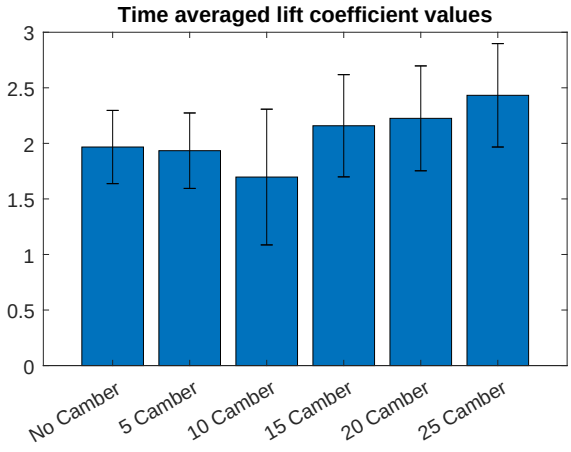

(b) Lift force coefficients

Figure 4.80: Time averaged force coefficient values

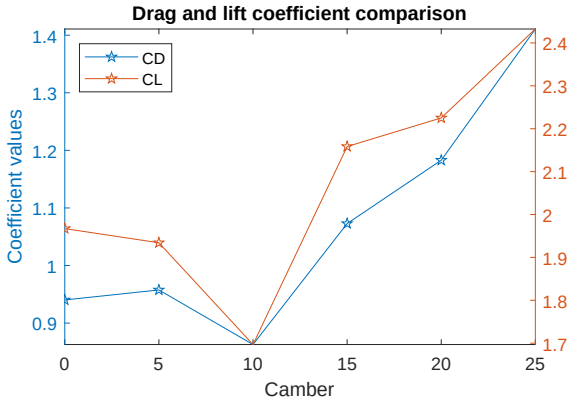

(a) Comparison of coefficients

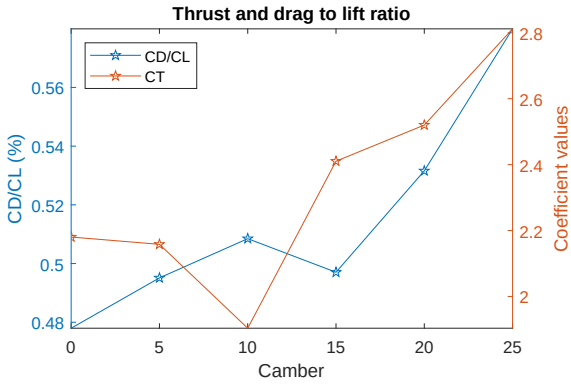

(b) Thrust and size relation between coefficients

Figure 4.81: Time averaged force coefficient values

As can be seen in the figures above, if the camber is increased enough then the performance will increase, with emphasis on enough.

The following table presents the camber angles where the greatest thrust coefficient values were achieved

Camber	25	20	15
C_T	2.8120	2.5200	2.4104

Table 4.15: The three greatest thrust coefficient values in descending order and the respective camber angle

Comparing the greatest cambered result in table 4.15 to the greatest non cambered result in table 4.5 as before, a 29% increase in maximum potential thrust can be observed.

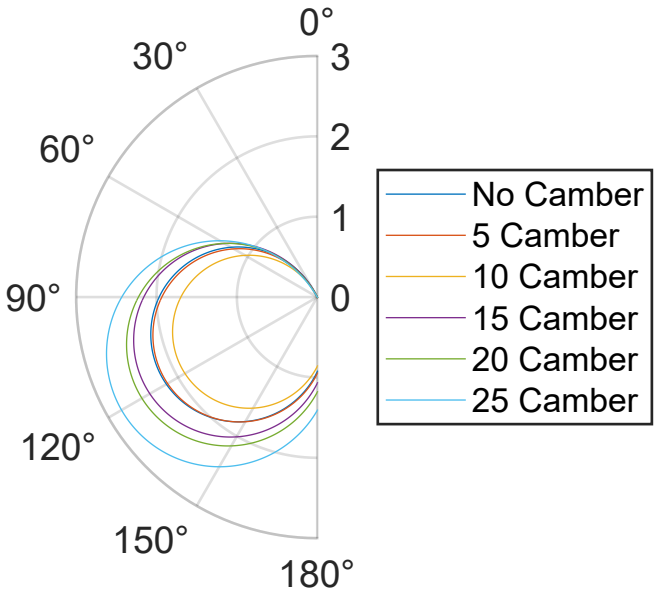

Figure 4.82: Polar plot comparison of the effect of different camber angles on the thrust of the sail at a wide span of apparent wind angles

Just like in the previous figure (4.79) for the wingsail with a ratio of 70/30, it can be seen that an increase in camber leads to an increase in propulsion, with the exception of the first two increments in camber, where the performance actually decreases before it increases.

4.2.3.3 Cambered 90/10

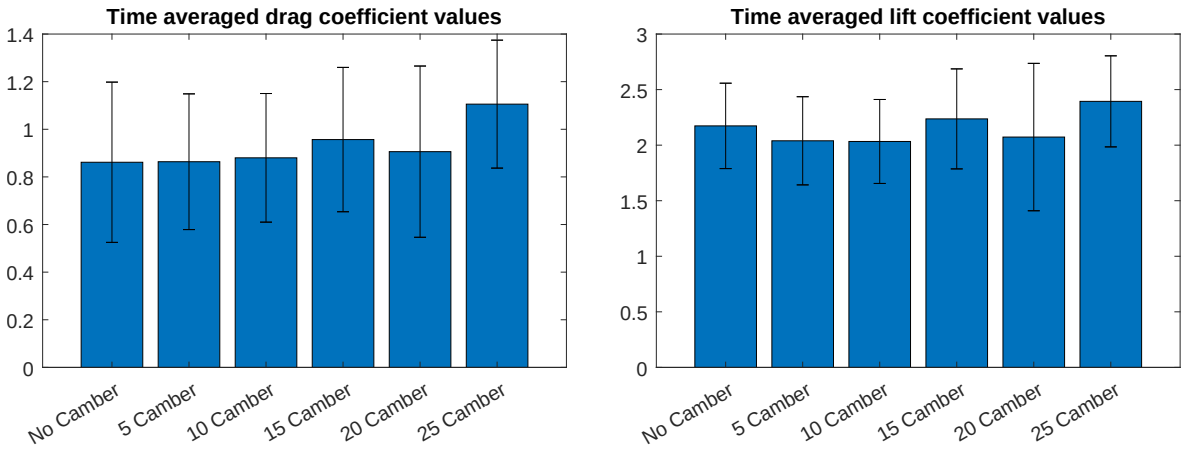

(a) Drag force coefficients

(b) Lift force coefficients

Figure 4.83: Time averaged force coefficient values

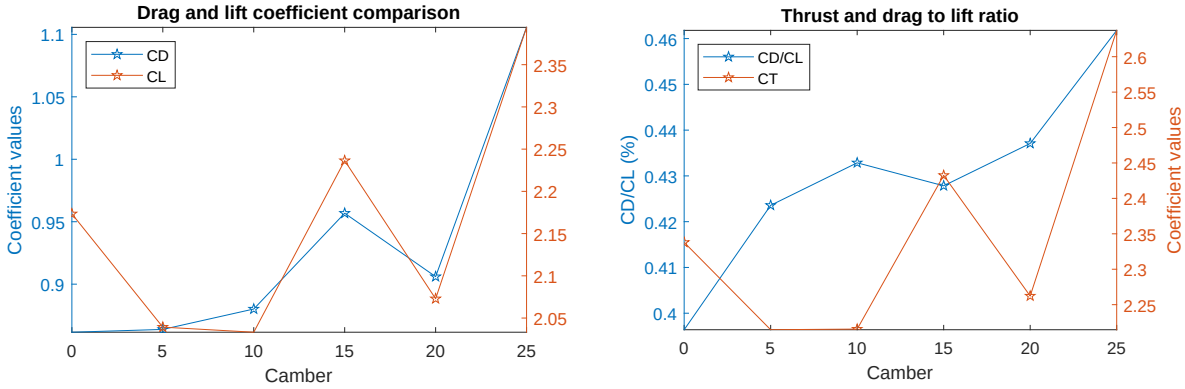

(a) Comparison of coefficients

(b) Thrust and size relation between coefficients

Figure 4.84: Time averaged force coefficient values

At this point the latter two of the three studied wingsail ratios have shown a behaviour where the propulsive performance decreases with the initial increase of the camber angle before increasing. However all two element foil wingsails show that if the camber angle is increased enough then the gain in potential maximum thrust is significant compared to a non-cambered setup.
The following table presents the camber angles where the greatest thrust coefficient values were achieved

Camber	25	15	0
C_T	2.6371	2.4324	2.3379

Table 4.16: The three greatest thrust coefficient values in descending order and the respective camber angle

Once again comparing the best result in table 4.16 with its non-cambered counterpart in table 4.8 the increase in maximum potential thrust is 13%. Comparing the three different wingsails it seems as if the design with a ratio of 70/30 benefits the most from an increase in camber as the increase in maximum potential thrust decreased for each wingsail presented in this section.

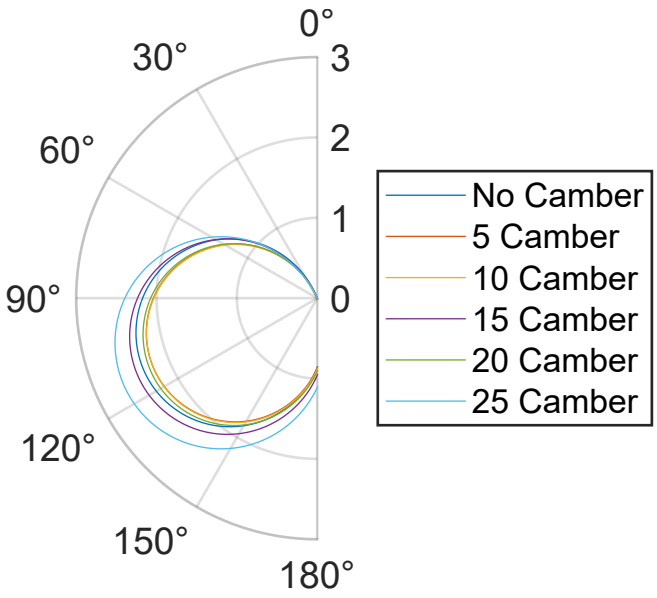

Figure 4.85: Polar plot comparison of the effect of different camber angles on the thrust of the sail at a wide span of apparent wind angles

The results of 5, 10 and 20° camber are quite similar to each-other, and notably worse than the option of no camber, but just like the previous polar plot 4.82 the performance decreases for the first two increments in camber, and then starts to increase, with the exception of 20°.

4.2.4 Comparison between cambered and crescent results

The best cambered results from the previous polar plots 4.79, 4.82 and 4.85 are now plotted together with the crescent result that showed the most promise.

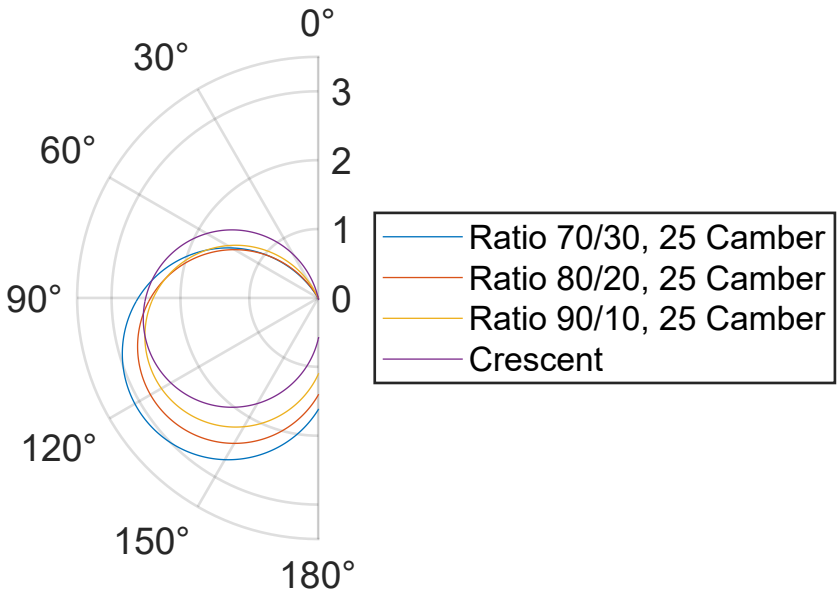

Figure 4.86: Comparison of thrust for the full range of θ_{AW} for the crescent-shaped wingsail and the most promising designs of the two element foil wingsails.

The performance of the crescent-shaped wingsail in figure 4.86 is more symmetrical around the 90° mark than for the other wingsails, which are more skewed towards the lower half of the graph. Naturally this means that the crescent-shaped wingsail performs better when θ_{AW} is somewhere between 0 and 90°. After this point however, the other wingsails quickly excel in their performance, most notably the wingsail with ratio 70/30 which far outclasses all other sails. The overall performance of the crescent-shaped wingsail seems to be the closest to the two foil wingsail with ratio 90/10, and worse than the one with ratio 80/20. From this figure one might infer that a bigger aft foil yields better propulsive performance, which would make sense as a bigger aft foil would be able to deflect more flow downwards.

4.3 Three Foil

This section presents the results from the three foil element sail design for the different camber angles and AoA with a fixed gap distance and chord length ratio.

4.3.1 Ratio 15/70/15 with no gap and no camber

Below the results for different AoA are presented for the setup of the three element foil sail with a chord length ratio of 15, 70 and 15 for the front, middle and aft foil respectively. In the setup of the simulations the distance between the trailing edge of the smaller front foil and the leading edge of the bigger middle foil was set to be zero. Likewise the distance between the leading edge of the smaller back foil and the trailing edge of the bigger middle foil was set to be zero.

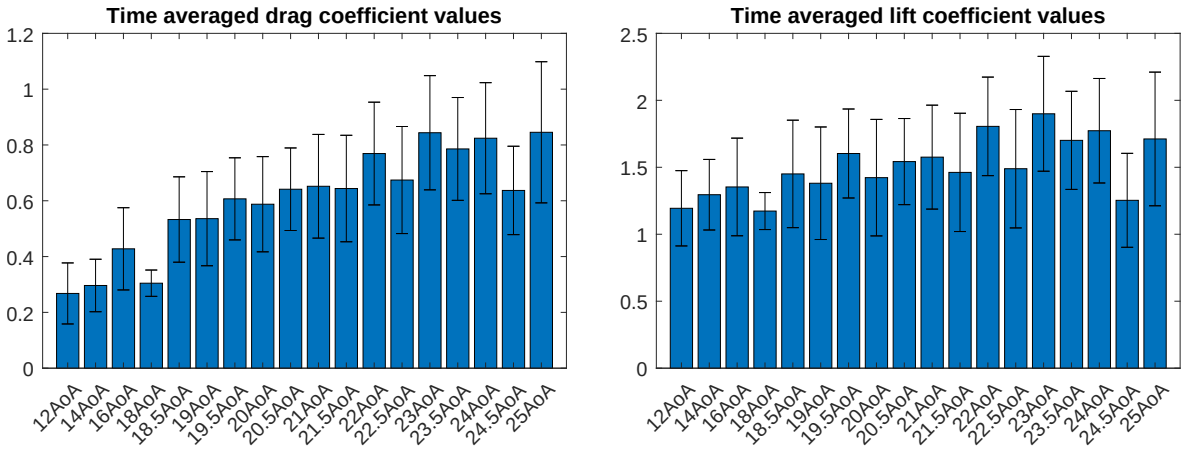

(a) Drag force coefficients

(b) Lift force coefficients

Figure 4.87: Time averaged force coefficient values

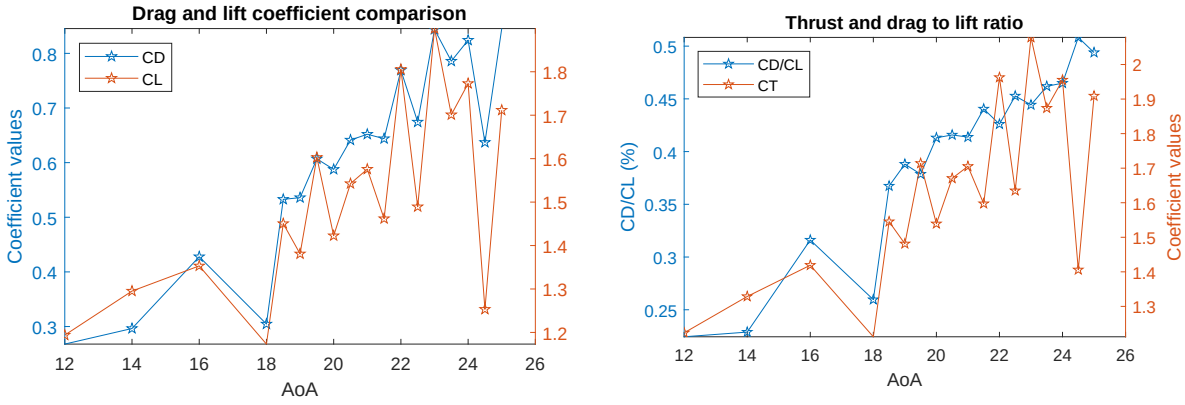

(a) Comparison of coefficients

(b) Thrust and size relation between coefficients

Figure 4.88: Time averaged force coefficient values

Looking at the bar plots in figure 4.87 it can be seen that there is some significant oscillations of the force coefficients, which is also reflected on the time-averaged force coefficient values. In figures 4.87 (b) and 4.88 (a) several points where loss of lift occurs can be observed, ranging from 18°AoA to 24.5°AoA, making the range of stall 16°AoA to 24°AoA. Since it can be observed that the lift recovers after 24.5°AoA it is hard to predict whether or not it will exceed the maximum found at 23 AoA or begin to decline, and while it seems like this airfoil experiences a large range of stall, the angle at which the largest lift is observed and thus presumed the more definite stall angle, is 23 AoA. Comparing it to it's two element foil counterparts with no

gap distance it can be seen that stall behaviour appears at the same angle as for the two foil wingsail with ratio 90/10, but at a later and earlier angle than for the wingsails with ratio 80/20 and 70/30 respectively.

The following table presents the AoA where the greatest thrust coefficient values were achieved

AoA	23AoA	22AoA	24AoA
C_T	2.0784	1.9625	1.9551

Table 4.17: The three greatest thrust coefficient values in descending order and the respective AoA

4.3.2 23AoA

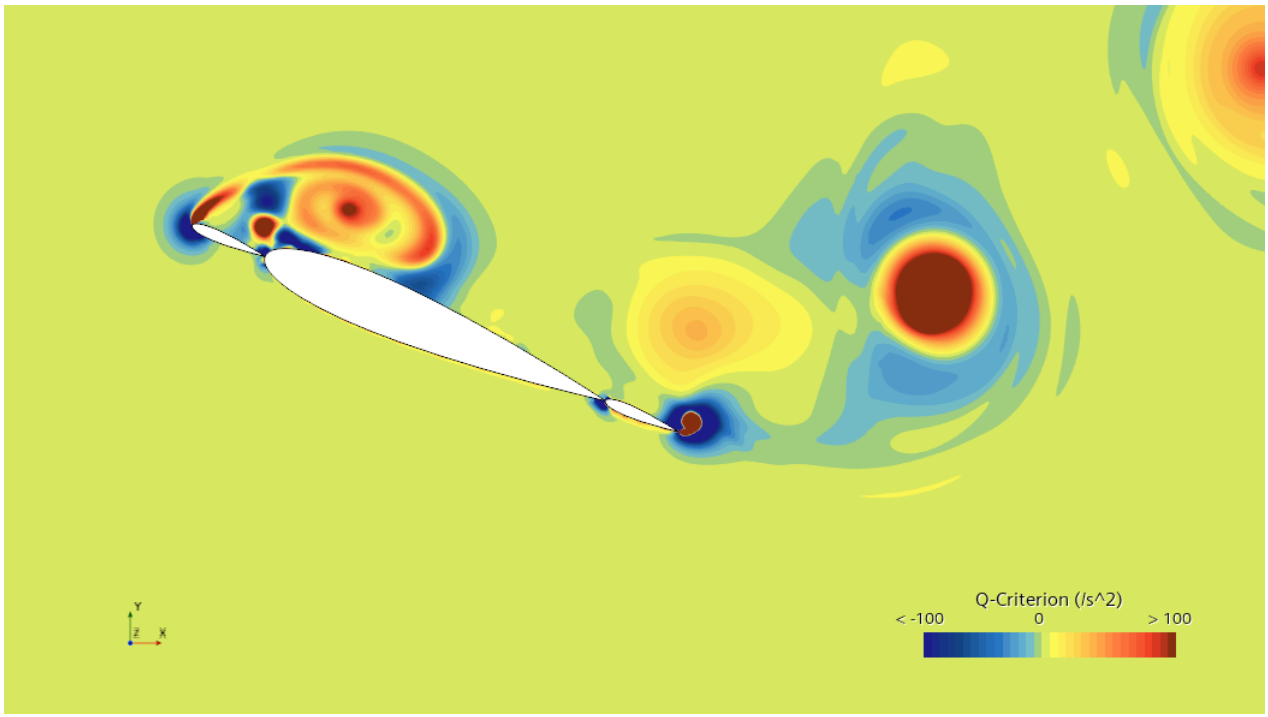

Figure 4.89: Q-Criterion at 120 000 iterations

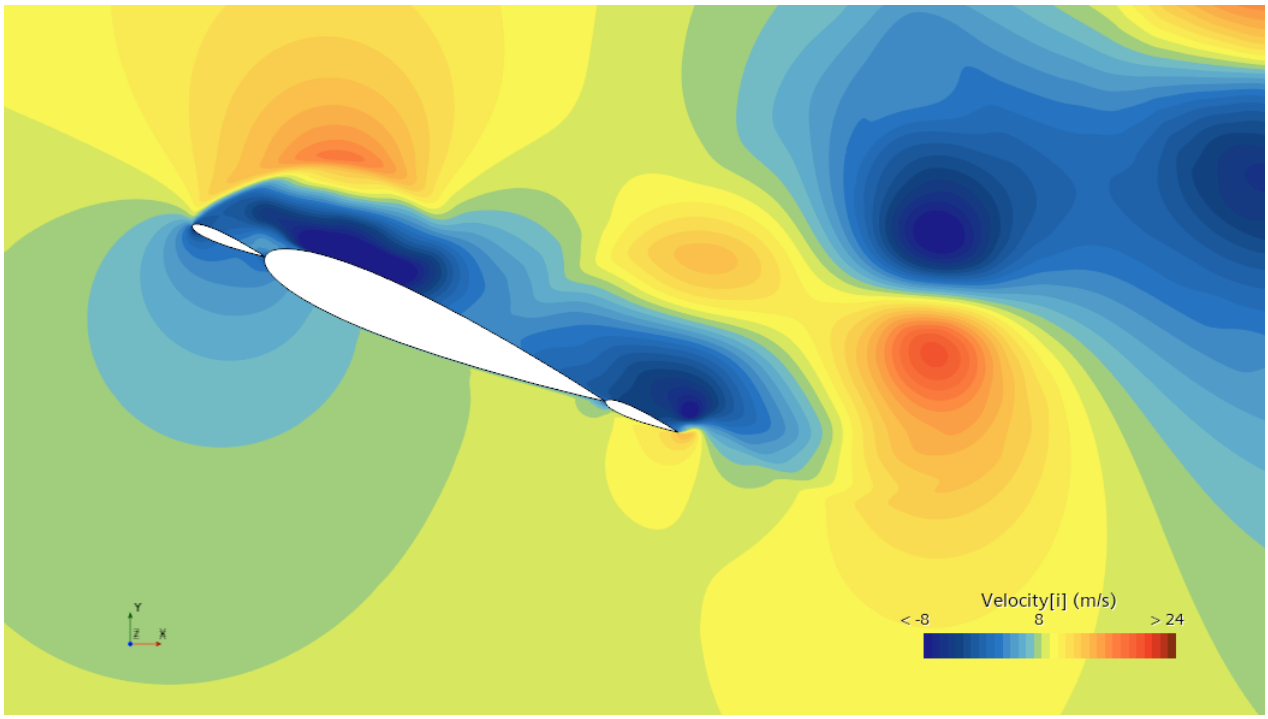

Figure 4.90: Velocity at 120 000 iterations

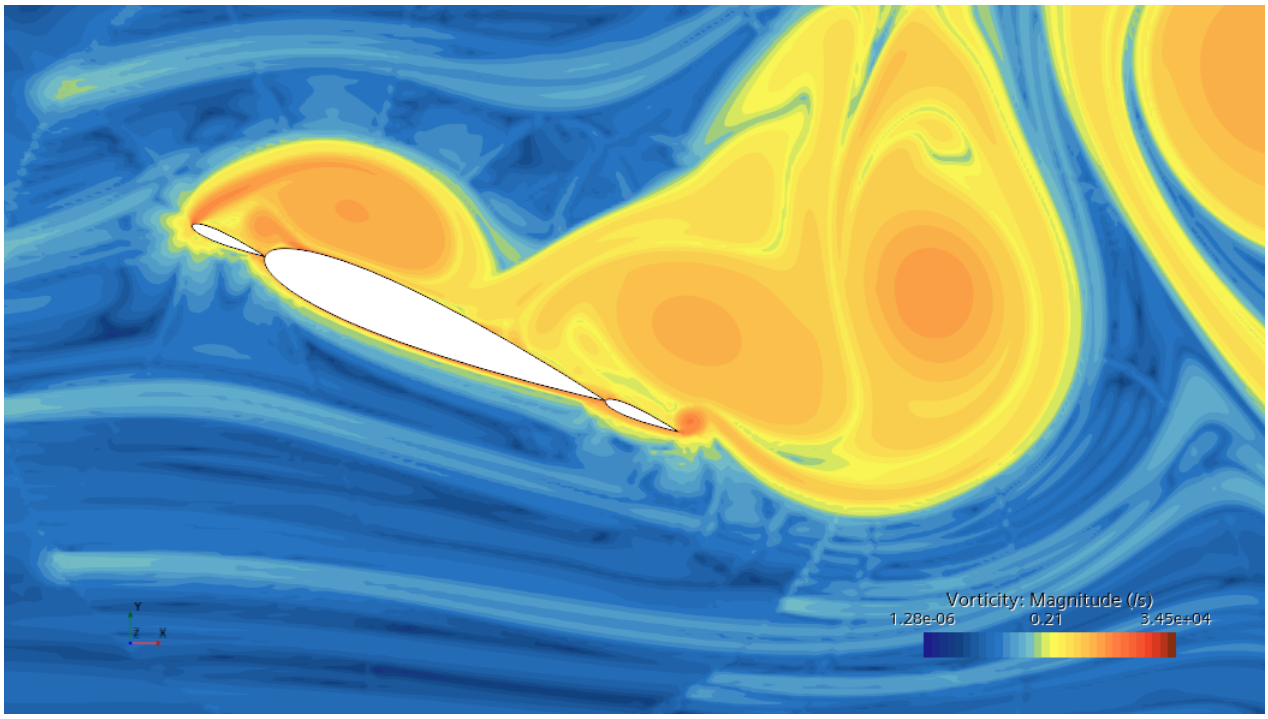

Figure 4.91: Vorticity at 120 000 iterations

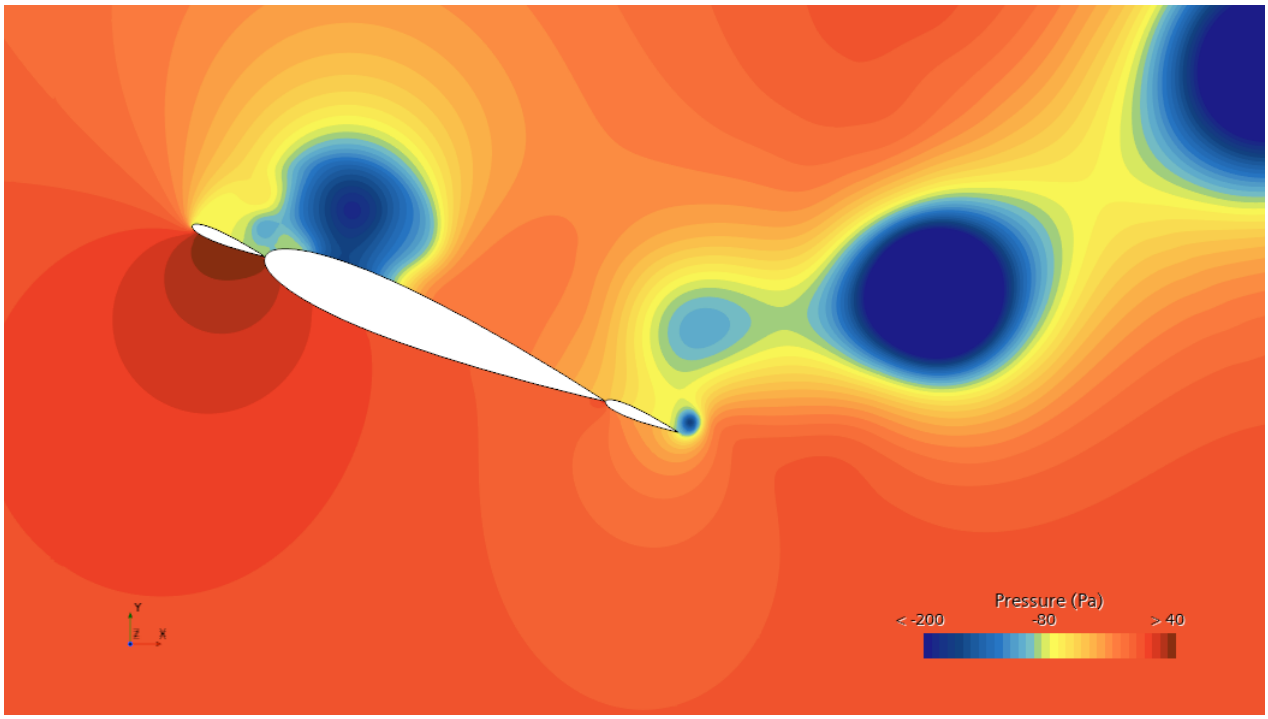

Figure 4.92: Pressure at 120 000 iterations

In the velocity plot in figure 4.90 one might notice that the entire small foil at the front of the wingsail acts similar as the leading edge does for the bigger foil in the two element foil cases. As in previous cases the decrease in velocity at the leading edge of the front foil hints of some flow separation. The increase in velocity at the front foils trailing edge that later slows down a little bit downstream of the middle foils leading edge, might be cause for some vorticity. As might also be the case for the increase and later decrease in velocity that can be seen at about the half-chord length of the middle foil. Studying the pressure plot in figure 4.92 it seems that it is more likely to observe vorticity closer to the leading edge of the middle foil, which is confirmed by figure 4.91. The Q-Criterion plot in figure 4.89 shows that the flow is mostly vorticity dominated at the leading edge of the front and middle foil, as well as a pocket of vorticity dominated flow at the trailing edge of the aft foil, surrounded by strain dominated flow, which appears to dissipate or transition into vorticity dominated flow in the wake.

4.3.3 Cambered three foil results

Below the results from the cambered three foil simulations are presented for the ratio 15/70/15.

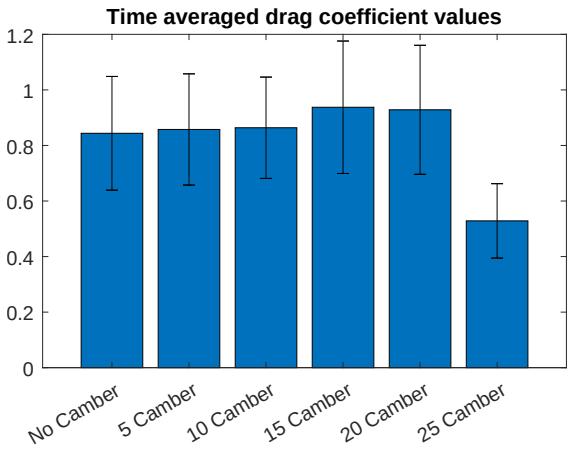

(a) Drag force coefficients

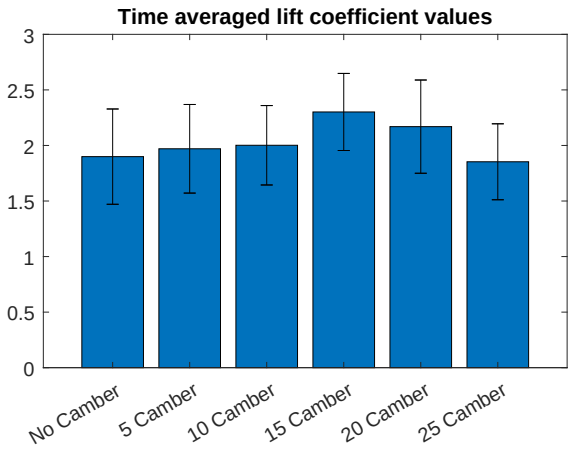

(b) Lift force coefficients

Figure 4.93: Time averaged force coefficient values

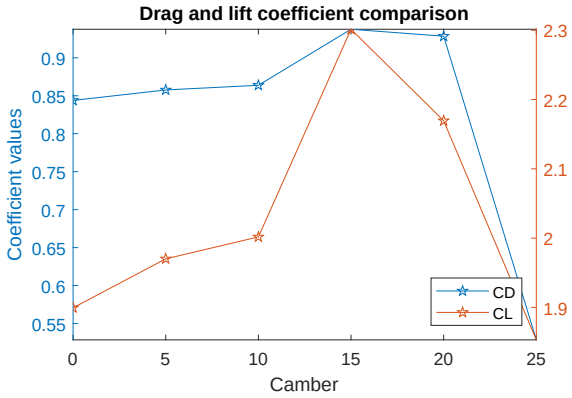

(a) Comparison of coefficients

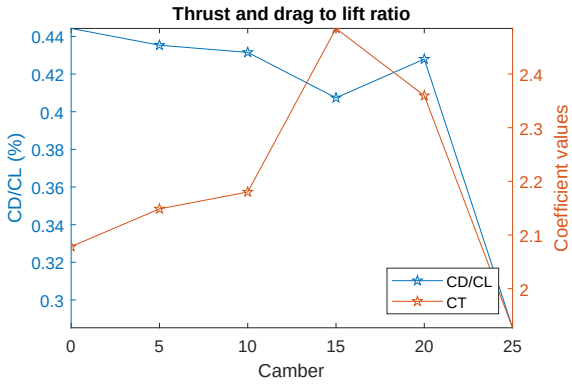

(b) Thrust and size relation between coefficients

Figure 4.94: Time averaged force coefficient values

The figures 4.93 and 4.94 above show, unlike the previous cases, that if the camber is increased then the performance will increase up until 15° of camber without any dips along the way. However, in contrast to the other cases the absolute worst performance is found at the greatest camber, which although puzzling, might indicate that slightly before 23°AoA is the stall angle for this three element foil sail with a camber of 25°.

The following table presents the camber angles where the greatest thrust coefficient values were achieved

Camber	15	20	10
C_T	2.4850	2.3597	2.1801

Table 4.18: The three greatest thrust coefficient values in descending order and the respective camber angle

If the best result presented in table 4.18 is divided by that from table 4.17 then a increase in the maximum potential thrust of 20% can be observed. Note that this increase is greater than that of the two element foil with ratio 90/10, but less than those with the ratio 80/20 and 70/30. It does seem that sail designs with bigger flaps also benefit the most from increased camber.

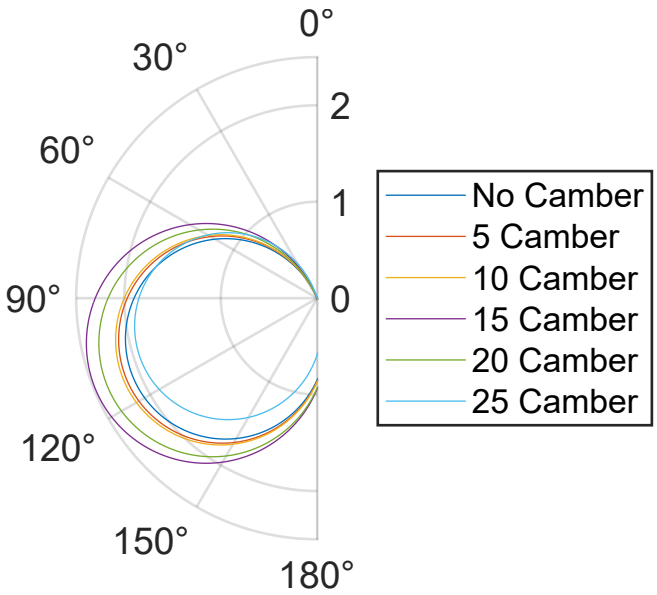

Figure 4.95: Polar plot comparison of the effect of different camber angles on the performance of the sail

As can be seen in the polar plot in figure 4.95 and in agreement with what was shown in both figure 4.93 (b) and 4.94 (b) the performance only increases for the first three increment increases in camber, in contrast to the two element foils with ratio 90/10 and 80/20 which decreased in performance when the camber was initially increased. Notably it can also be observed that in stark contrast to the previous results, the greatest camber yielded the worst performance.

4.3.4 Polar plot comparison between non-cambered two and three element foils and crescent-shaped sail

Here the different designs of the two element foil sails will be compared to the three element foil design in order to see if there is any significant difference between them. The crescent-shaped profile will also be added to give some further perspective on the performance.

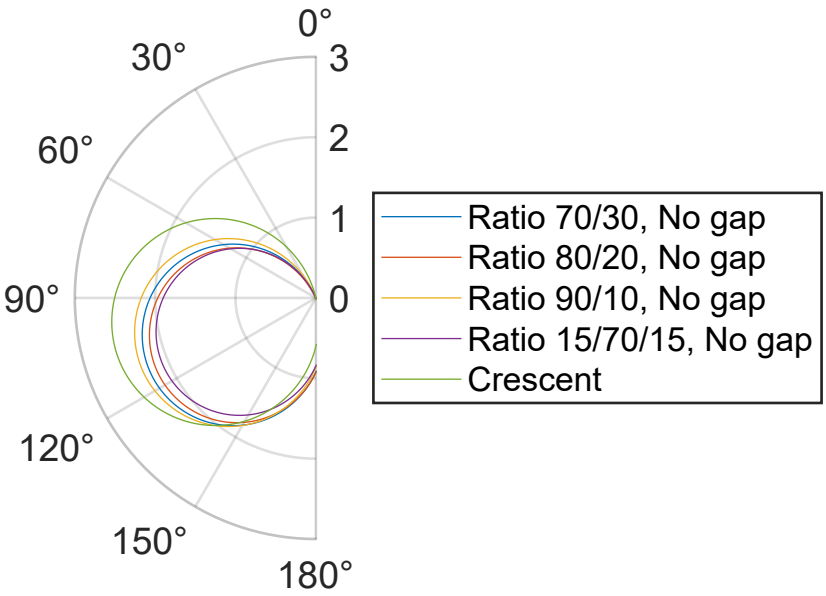

Figure 4.96: Comparison between the crescent-shaped sail, different configurations of the two foil sail and a three foil sail

Although it is hard to draw any just conclusions from figure 4.96, it does appear from the cases studied that having a three element foil design is not inherently superior to any two element foil design.

4.3.5 Polar plot comparison between cambered two and three element foils and crescent-shaped sail

In the figure below all cambered multi-element foil sail designs which yielded the greatest results for each respective sail, is compared to the crescent-shaped wingsail.

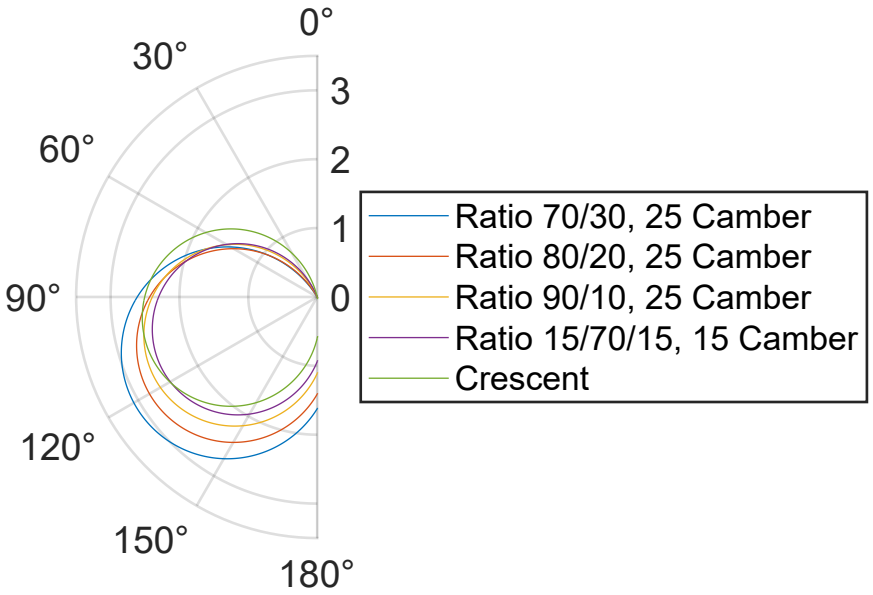

Figure 4.97: Comparison between different configurations of the two foil setup, a three foil setup and the crescent-shaped sail

Just as was observed earlier, the crescent-shaped wingsail performs best in the range 0° to roughly 90° of θ_{AW}, and overall performs better than the three element foil wingsail, although the three element foil wingsail does display better performance in the range 120° to 180° θ_{AW}. The introduction of camber to the three element foil sail did not improve its overall performance beyond what has been seen for the cambered two element foil designs, but it should be noted that it between roughly 0° and 60°+ does perform slightly better than the two element foil designs.

4.4 Summary of presumed stall angles and onset of stall behaviour for all rigid wingsails

This section will compile all the presumed stall angles and the AoA at which the first stall can be observed into a table for ease of viewing and comparing.

Sail	Type of stall	No gap [AoA]	5% gap [AoA]	10% gap [AoA]
Crescent	Onset angle	19.5		
Crescent	Stall angle	20.5		
Two Foil				
70/30	Onset angle	18.5	16	18
70/30	Stall angle	25	24.5	24.5
80/20	Onset angle	14	14	14
80/20	Stall angle	24.5	23.5	24.5
90/10	Onset angle	16	18	18
90/10	Stall angle	23.5	25	24
Three Foil				
15/70/15	Onset angle	16		
15/70/15	Stall angle	23		

Table 4.19: Comparison of stall angles for the crescent-shaped wingsail and all non-cambered multi-element foil sails

4.5 3D Results

Due to restrictions in allocated time on the cluster for this study, only two rigid wingsails will be subject to further simulations in 3D. The wingsails that were chosen were the crescent-shaped wingsail and the two element foil sail with a ratio of 70/30 and a camber angle of 25°.

4.5.1 Crescent

This section will touch on the flow field characteristics, wake flow and tip vortices of the crescent-shaped wingsail as well as some time-averaged results.

4.5.1.1 Flow field characteristics

In figure 4.98 the difference in flow field between the LES and uRANS models for the crescent-shaped profile can be observed.

(a) Velocity in spanwise direction with uRANS flow field

(b) Velocity in spanwise direction with LES flow field

Figure 4.98: Comparison of turbulence models

Due to the shape of the crescent profile there is significant flow separation on the suction side close to its trailing edge. Furthermore significant tip vortices can be observed which cause a reduction of lift. Both the tip vortices and numerous other vortex tubes extend into the wake region. Figure 4.99 also illustrates the limitations of 2D simulations as the figure shows noticeable variation of velocity in the spanwise direction, displaying interesting three dimensional characteristics such as the reduction of velocity when approaching the tip of the wingsail.

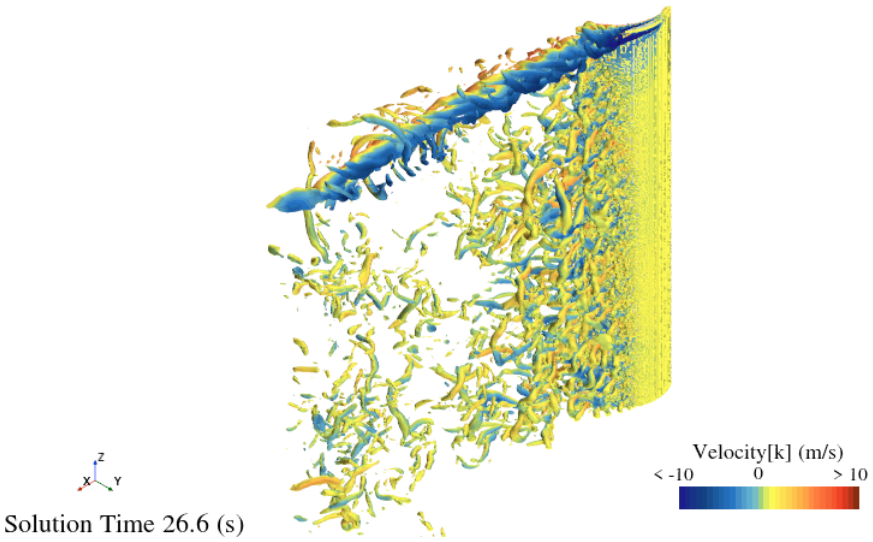

Figure 4.99: Velocity in spanwise direction with LES flow field

4.5.1.2 Wake flow

As was shown in the previous figures 4.98 (a) and (b) there is significant vortex shedding which affects the flow downstream of the wingsail. However it would be interesting to see how far downstream these effects can be felt before they eventually dissipate, as any real-world application of rigid wingsails would likely have multiple sails installed. Figure 4.100 helps to visualize the characteristics of the wake flow, and perhaps illustrates better what appears to be tip-leaking vortices, also seen in figures 4.99 and 4.101.

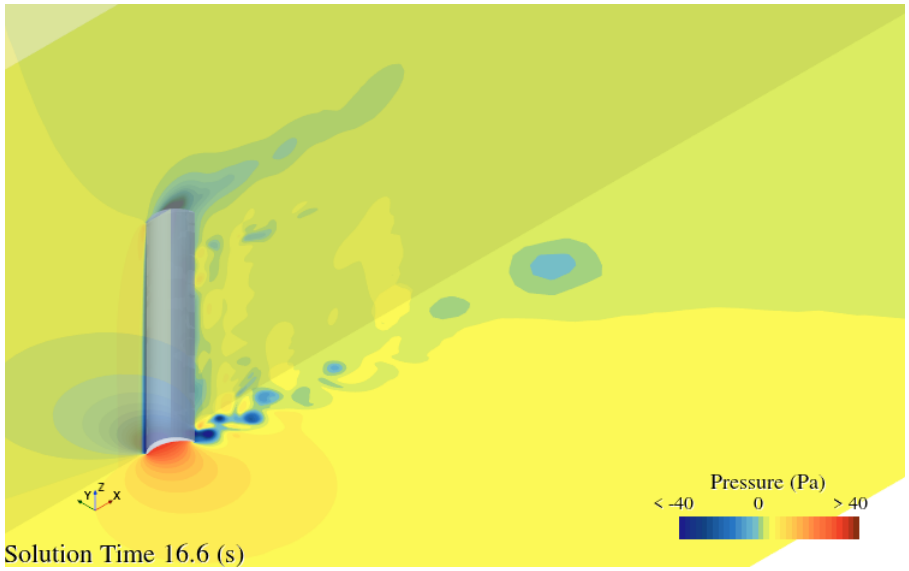

Figure 4.100: 3D visualization of the pressure propagation in the wake region

In order to better understand what figure 4.101 shows, it is recommended to revisit figure 3.4 to remind yourself of the coordinate system. The first figure is a cross-

section of the YZ-plane at the half-chord of the sail (X = 0m) in figure 4.100 where the pressure and suction sides can be viewed clearly. The second figure is right at the trailing edge (X = 7m) of the crescent profile, and the subsequent figures are further and further downstream (increasing X) in the wake of the sail. From the trailing edge and far into the wake region the presence of low pressure can still be detected which is of interest, since low pressure in this instance is indicative of the presence of vortices.

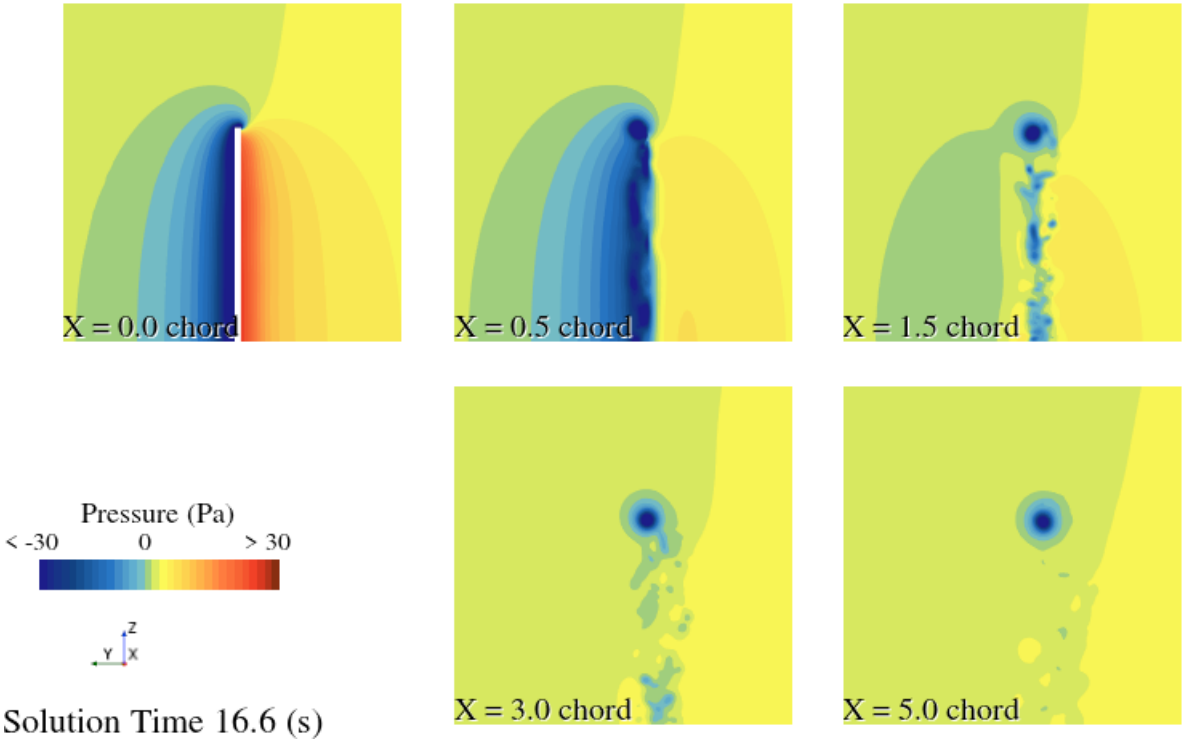

Figure 4.101: Propagation of pressure in the downstream direction

4.5.1.3 Tip vortices

To get a more detailed view of the tip vortices the streamlines of the velocity in the z-direction are plotted, as shown in figure 4.102. From the figure a flow between the pressure side (high velocity) and suction side (low velocity) can be observed, with a large tip vortex at the top of the wingsail and what appears to be a smaller tip vortex at the top edge of the suction side. The location of these tip vortices coincide with the observed low pressure in figures 4.101 and 4.100, as well as the flow field in figure 4.99. These tip vortices do affect the characteristics of the flow in a quite big surrounding of the tip of the sail, considering that the half-chord width is 2m meaning that the spanwise flow extends about 10m around the tip.

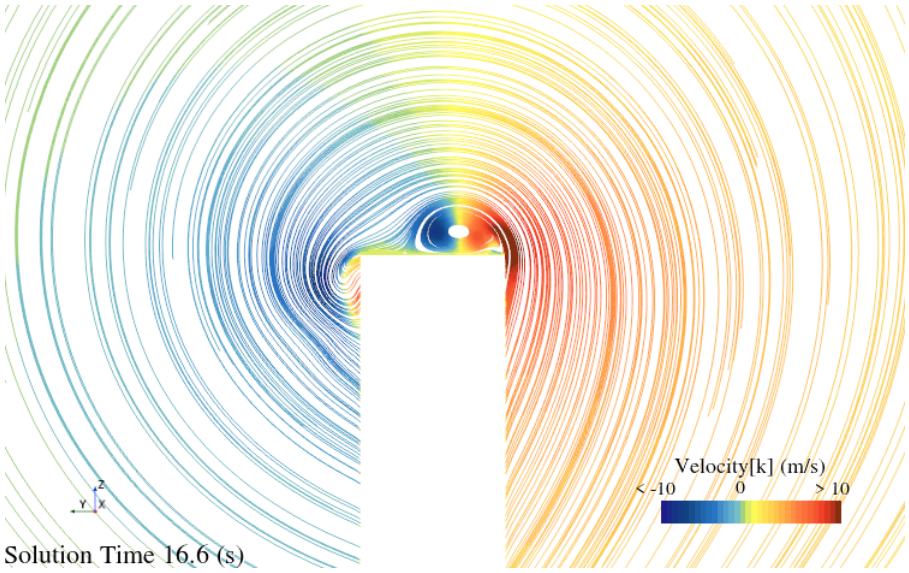

Figure 4.102: Streamlines of velocity in the z-direction

4.5.1.4 Time-Averaged results

As before with the 2D simulations the results have been time-averaged in order to present the force coefficients, now also with the benefit of more physical time simulated. The figure below illustrates the difference between the two turbulence models that have been applied to the 3D simulations and the results given by the 2D simulation of the same case. It should be clarified that the bar named "20.5AoA" is the 2D simulation result, which used the same turbulence model as the bar named "RANS", that is, unsteady Reynolds-Averaged Navier-Stokes with the $k - \omega$ SST model. Also note that since no wind tunnel experiments have been conducted it is assumed that the LES results are the greatest indication of what the true value might be, as it is the more accurate model out of the two. From figure 4.103 (a) it becomes clear that the 2D simulations have over-predicted the drag coefficients and while the 3D simulations are better, the RANS model still over-predicts the value and is less accurate than LES which has quite small standard deviation. Although it should be noted that one of the reasons of the larger standard deviation for the RANS model might be the fact that the flow hadn't fully developed in the beginning of the time-span which was averaged upon. Surprisingly from figure 4.103 (b) the time-averaged result from the 2D simulation predicts the lift coefficient very well, although its standard deviation is notably bigger than its 3D counterpart, which underestimated the force coefficient.

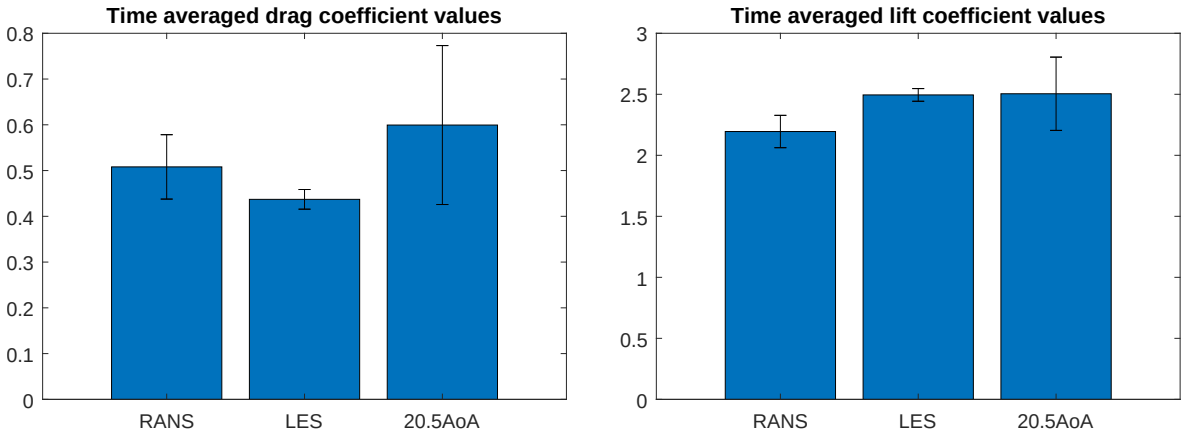

(a) Drag coefficients of the two 3D results (left and middle) and the 2D result (right)

(b) Lift coefficients of the two 3D results (left and middle) and the 2D result (right)

Figure 4.103: Comparison of turbulence models effect on force coefficients as well as difference between 3D and 2D results

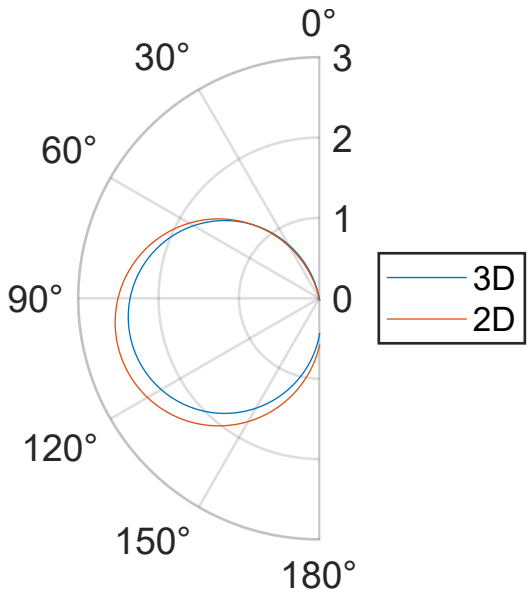

Figure 4.104: Polar plot comparison of performance predicted by 3D LES and 2D uRANS simulations

4.5.2 Two Foil 70/30

This section will touch on the flow field characteristics, wake flow and tip vortices as well as some time-averaged results of the two element foil wingsail with ratio 70/30, without gap and with 25 °camber.

4.5.2.1 Flow field characteristics

In figure 4.105 the difference in flow field between the LES and uRANS models for the two element foil wingsail can be observed.

(a) Velocity in spanwise direction with uRANS flow field

(b) Velocity in spanwise direction with LES flow field

Figure 4.105: Comparison of turbulence models

In contrast to the crescent-shaped profile flow separation for the two element foil wingsail can be observed closer to the leading edge. Furthermore the figures show clear and significant tip vortices originating from where the top of the front and aft foils trailing and leading edges, respectively, meet. Just as for the crescent-shaped profile noticeable variations in velocity can be observed in the spanwise direction when approaching the tip of the wingsail. Lastly it can be seen that both the tip vortices and several vortex tubes extend into the wake of the wingsail.

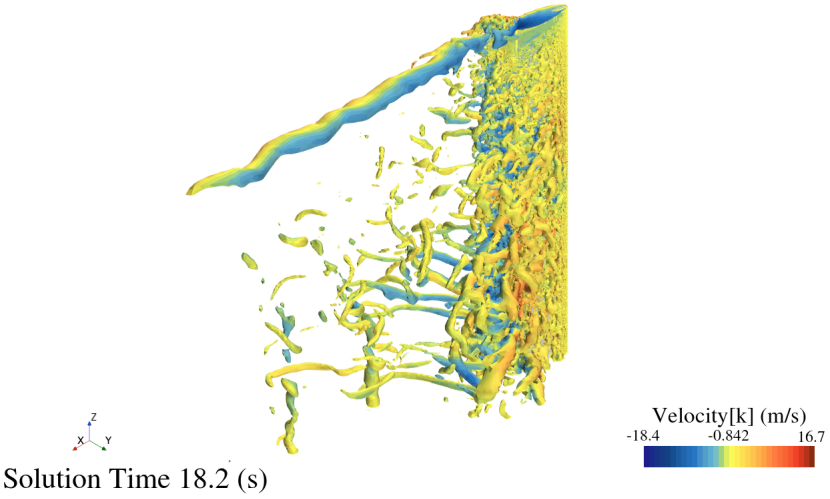

Figure 4.106: Velocity in spanwise direction with LES flow field

4.5.2.2 Wake flow

Just as for the crescent-shaped profile there is some significant vortex shedding and tip vortices as seen in figure 4.106 and it is interesting to observe the presence of any effects caused by the sail in the wake. Figure 4.107 might facilitate the perception of the depth at which low pressure appears in the wake, and also illustrate what is presumably the tip vortices.

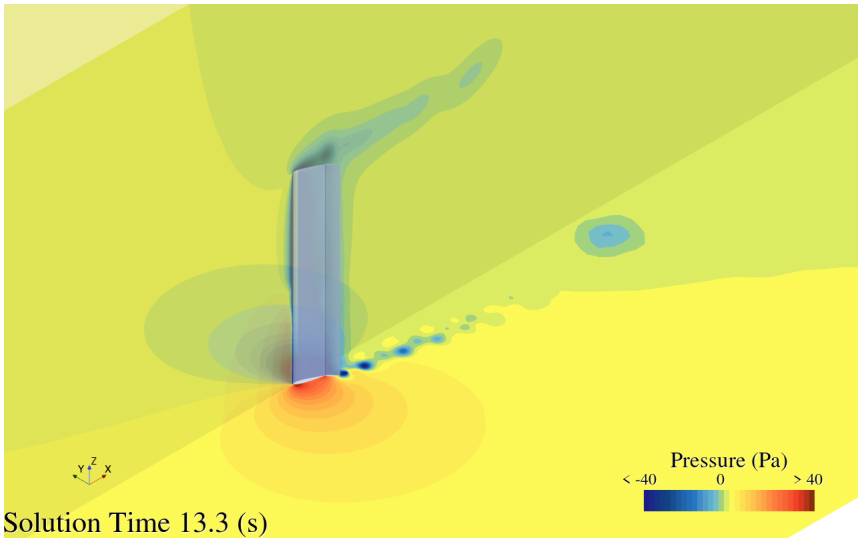

Figure 4.107: 3D visualization of the pressure propagation in the wake region

Remember that the images shown in figure 4.108 are the images of the pressure in figure 4.107 taken at different cross-sections of the YZ-plane, starting at X = 0m and then increasing. As can be seen in figure 4.108 there is a presence of low pressure far into the wake region of the wingsail and what appears to be the somewhat dissipated tip vortices. To the keen observer it can also be seen that at the tip of the wingsail low pressure from the suction side appears to leak over to the pressure side.

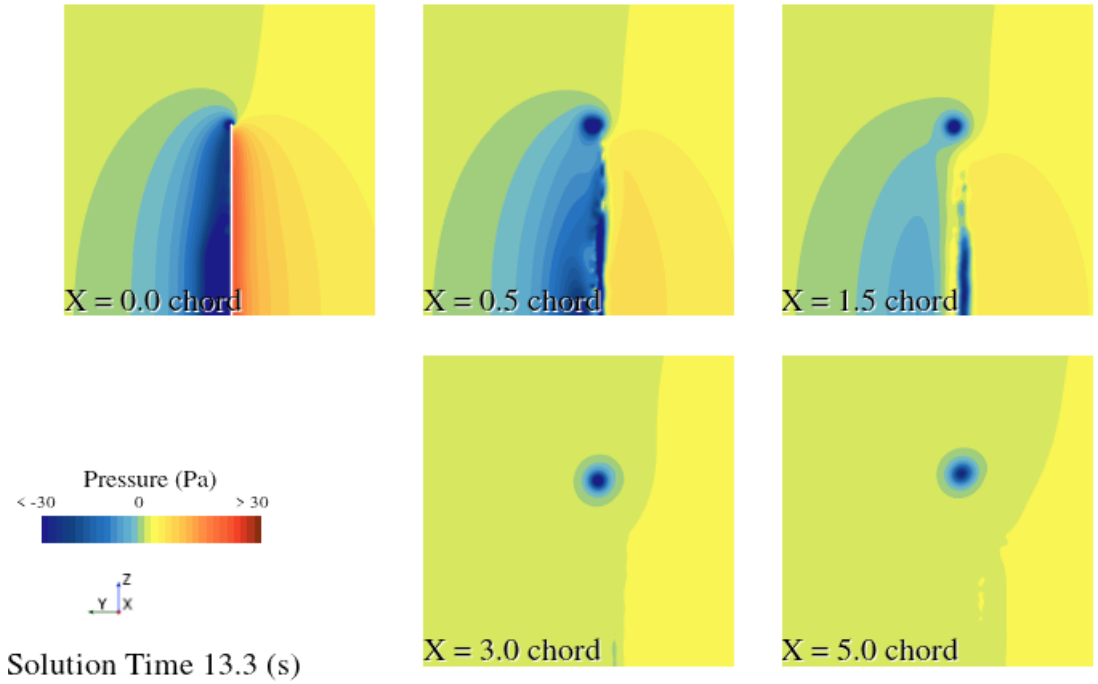

Figure 4.108: Propagation of pressure in the downstream direction

4.5.2.3 Tip vortices

Once again flow from the pressure side to the suction side can be observed, with what appears to be one large tip vortex located at the top of the wingsail and bending over towards the suction side of the wing. The location of this tip vortex also coincides with the low pressure at the tip as shown in figures 4.107 and 4.108 as well as the tip vortex shown in the flow field in figure 4.106. The increase in velocity close to the wingsail on the suction side can also be observed for the crescent-shaped profile in figure 4.102, but to a much lesser extent than what is shown here. These tip vortices do not affect the characteristics of the flow field in as big of a surrounding as in the case of the crescent-shaped profile. The width of the wingsail at half-chord is roughly 0.9m meaning that the spanwise flow extends about 4m around the tip.

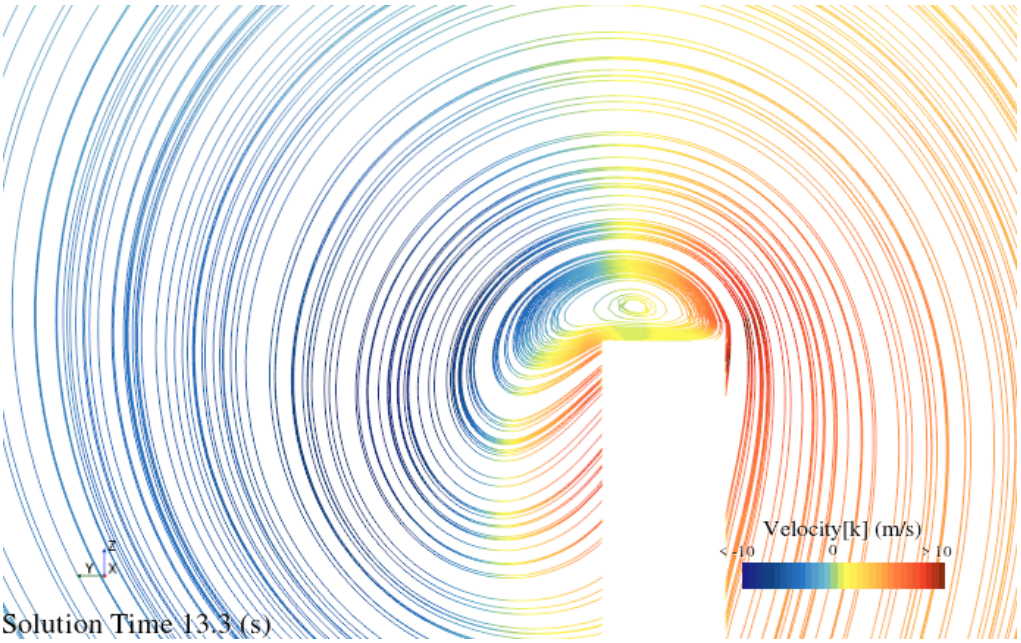

Figure 4.109: Streamlines of velocity in the z-direction

4.5.2.4 Time-Averaged results

Below are comparisons of time-averaged results between two 3D simulations and one 2D simulation, which in figure 4.110 is the bar denoted as "25AoA" and uses the same turbulence model as the bar denoted "RANS". Remember that the LES results are assumed to be the closest to the actual or true value for the wingsail, as was previously stated for the case with the crescent-shaped profile. From figure 4.110 (a) the overestimation of the drag coefficient can be seen to be more than threefold of the actual value, which is similar to the observed drag value for the crescent-shaped profile. In figure 4.110 (b) the lift was over-predicted in the 2D simulations as well, showing the actual value to be lower than what was seen for the crescent-shaped profile in figure 4.103 (b).

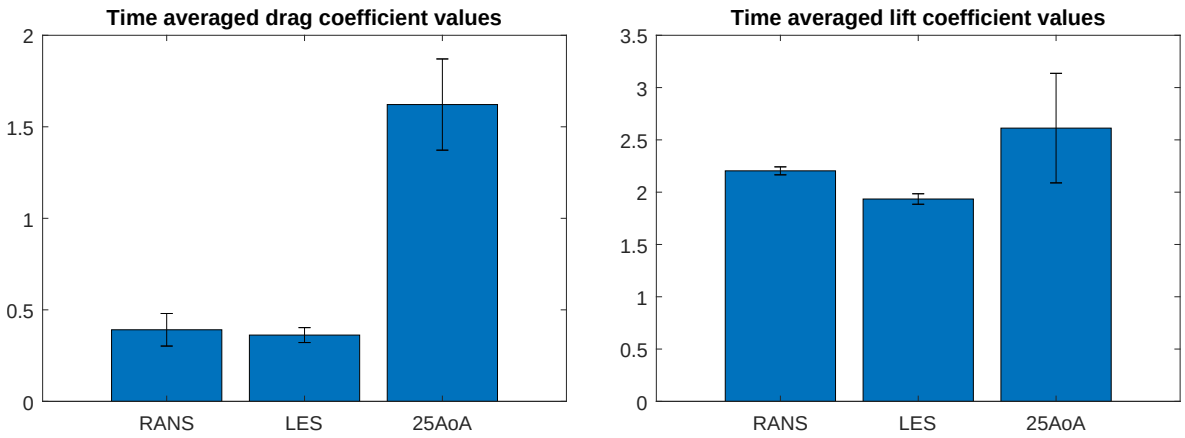

(a) Drag coefficients of the two 3D results (left and middle) and the 2D result (right)

(b) Lift coefficients of the two 3D results (left and middle) and the 2D result (right)

Figure 4.110: Comparison of turbulence models effect on force coefficients as well as difference between 3D and 2D results

A better grasp of the overestimation of the performance is given when inspecting figure 4.111, where it can be seen that apart from the range between 0 and roughly 60°the performance of the two foil wingsail was severely overestimated.

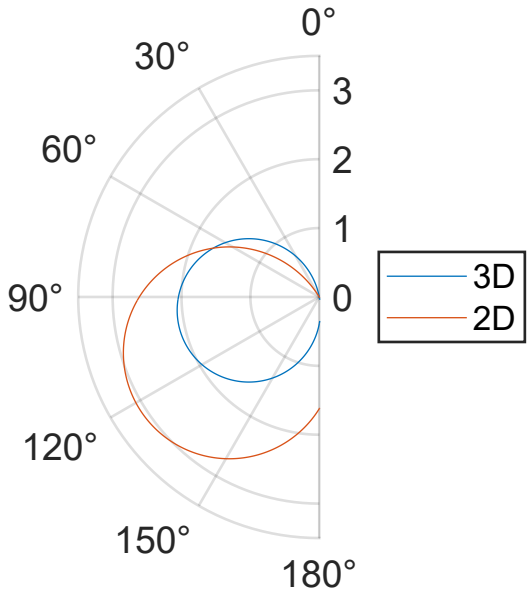

Figure 4.111: Polar plot comparison of performance predicted by 3D LES and 2D uRANS simulations

4.5.3 Comparison between Crescent and Two foil

A brief comparison between the crescent-shaped profile and the two element foil wingsail previously presented will be made here, starting with a comparison of the polar plots. Figure 4.112 displays results that are in great contrast to what the 2D results in figure 4.97 suggested and highlights the inaccuracy that may accompany 2D simulations.

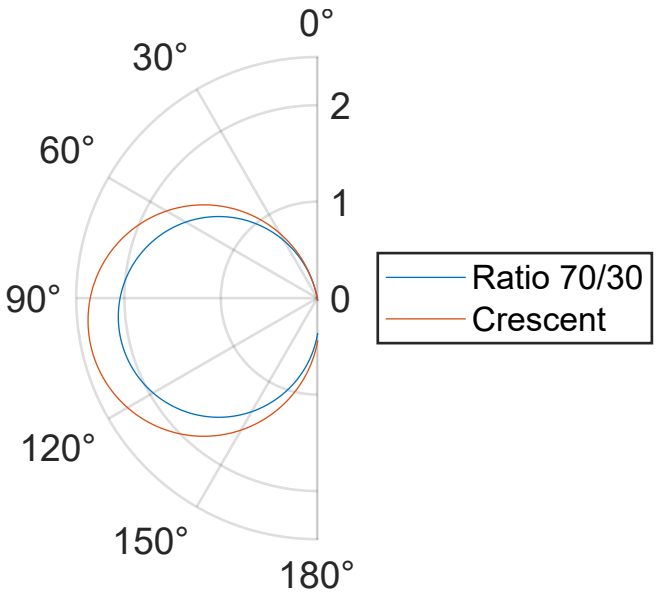

Figure 4.112: Comparison of propulsive performance between the crescent-shaped profile and the two element foil wingsail for a wide range of apparent wind angles, as predicted by the 3D LES model

The following two figures 4.113 (a) and (b) show the flow field characteristics of the two sails and as have been previously mentioned the flow separates closer to the trailing edge for the crescent-shaped profile and closer to the leading edge for the two element foil wingsail. Furthermore it appears that the tip vortices of the crescent-shaped profile are larger and have a more complex structure than those of the two element foil wingsail.

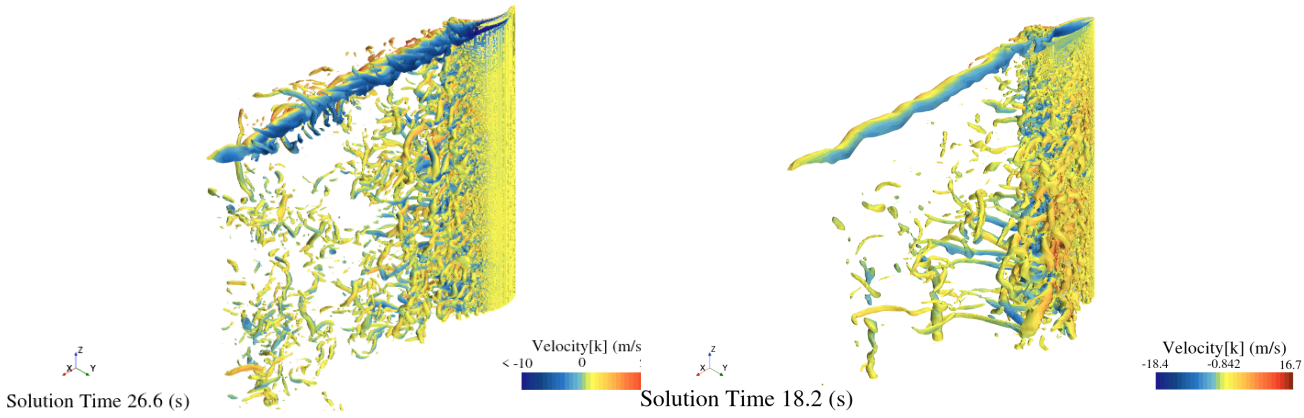

(a) Velocity in spanwise direction for the crescent profile with LES flow field

(b) Velocity in spanwise direction for the two element foil sail with LES flow field

Figure 4.113: Comparison of flow field characteristics between the crescent (left) and two element foil (right) sails

5
Conclusion

From table 4.19 one of the advantages of the crescent-shaped wingsail is made clear, as it can be seen that the appearance of stall behaviour is more delayed when compared to the multi-element foil designs. From the data available it does also seem like the three element foil sail displays similar behaviour as the two element foil sails when it comes to the angle at which the sail begins to experience stall behaviour. Although stall behaviour is delayed for the crescent-shaped wingsail, it also attains its maximum lift the earliest. Furthermore when comparing the bar plots between the crescent and non-cambered multi-element foil wingsails it becomes clear that the crescent-shaped wingsail generally generates a lot less drag than the others, with the exception of the wingsail with ratio 90/10 which seems to generate quite low drag for the majority of AoA studied. While this is unfavourable for propulsion, it also means that the crescent-shaped wingsail won't act as a parachute and slow the ship down as much if the wind suddenly changes. As expected thanks to previous studies [3] the bar plots also show that the crescent-shaped wingsail is superior in generating lift compared to the non-cambered multi-element wingsails. However when camber is introduced to the multi-element foil wingsails the drag generated is more than double that of the crescent-shaped wingsail, save for the wingsails with ratio 90/10 and 15/70/15 which are slightly and notably less than twice the drag, respectively. The lift coefficients of the multi-element foil wingsail do see a significant improvement when camber is introduced, however the coefficient values do not exceed the best value for the crescent-shaped wingsail, except for the wingsail with ratio 70/30 which actually surpasses it. However our perception changes as wee look at the 3D results which reveal that the drag has been severely overestimated for the two element foil sail with ratio 70/30 and 25°camber with no gap. From this revelation it seems likely that the drag would have been overestimated for the other two element foil designs as well. This seems to indicate that introducing camber has a greater effect on lift compared to drag, although this might seem intuitive already. Furthermore 3D simulations indicate that the crescent-shaped profile suffers from more severe tip vortices than the two element foil wingsail. Despite this however, the results showed that the performance of the crescent-shaped profile surpasses the two element foil wingsail with ratio 70/30 for all apparent wind angles, but it is hard to infer its performance in relation to the other designs without further 3D simulations.

Bibliography

[1] International Maritime Organization (IMO). (2021). Fourth IMO GHG Study 2020

[2] International Chamber of Shipping. (2014). Shipping, World trade and the reduction of CO_2 emissions. London: International Chamber of Shipping.

[3] Zhu, H. (2023). Methods for the Evaluation of Wingsails with a Crescent-Shaped Profile. [Licentiate thesis, Chalmers University of Technology].

[4] Cunliffe, T. (2016).The Complete Day Skipper: Skippering with Confidence Right From the Start (5 ed). Bloomsbury Publishing.

[5] Kimball, J. (2009). Physics of Sailing. CRC Press. https://doi.org/10.1201/9781420073775

[6] Sheldahl, R E, & Klimas, P C. Aerodynamic characteristics of seven symmetrical airfoil sections through 180-degree angle of attack for use in aerodynamic analysis of vertical axis wind turbines. United States. https://doi.org/10.2172/6548367

[7] Davidson, L. (2023). Fluid mechanics, turbulent flow and turbulence modeling. Division of Fluid Dynamics, Department of Mechanics and Maritime Sciences, Chalmers University of Technology.

[8] Menter, F. R. (1993). Zonal two equation $k-\omega$ turbulence models for aerodynamic flows. AIAA 23rd Fluid Dynamics, Plasmadynamics, and Lasers Conference, 1993. https://doi.org/10.2514/6.1993-2906

[9] Menter, F. R. (1992). Influence of freestream values on $k-\omega$ turbulence model predictions. AIAA Journal, 30(6):1657–1659.

[10] Menter, F. R. (1994). Two-equation eddy-viscosity turbulence models for engineering applications. AIAA Journal, 32:1598–1605.

[11] Frojd, K. SIEMENS. (2022-10-25). Simcenter STAR-CCM+ 2210 released! What's new?. Siemens. https://blogs.sw.siemens.com/simcenter/simcenter-star-ccm-2210-released-whats-new/

[12] Li, Dongqin., Zhang, Yili., Li, Peng., Dai, Jingjing., Li, Guohuan. (2019). AERODYNAMIC PERFORMANCE OF A NEW DOUBLE-FLAP WING SAIL (POLISH MARITIME RESEARCH, No 4/2019, vol 26). POLISH MARITIME RESEARCH.

[13] Li, Chen., Wang, Hongming., Sun, Peiting. (2020). Numerical Investigation of a Two-Element Wingsail for Ship Auxiliary Propulsion (Journal of Maritime Science and Engineering, Vol 8, issue 5). Journal of Maritime Science and Engineering. doi:10.3390/jmse8050333

[14] Viola, IM, Biancolini, ME, Sacher, M Ubaldo, C 2015, 'A CFD-based wing sail optimisation method coupled to a VPP', Paper presented at 5th High Performance Yacht Design Conference, Auckland, New Zealand, 9/03/15 - 11/03/15.
[15] White, F. M. (2011). Fluid Mechanics (Seventh edition) (pp. 488-489). McGraw-Hill.

DEPARTMENT OF SOME SUBJECT OR TECHNOLOGY
CHALMERS UNIVERSITY OF TECHNOLOGY
Gothenburg, Sweden
www.chalmers.se

CHALMERS
UNIVERSITY OF TECHNOLOGY